# DYNAMIC MODELING, SIMULATION AND DATA LOGGING OF A HYBRID POWER SYSTEM FOR A REMOTE HOUSE IN QINGHAI PROVINCE IN CHINA

By Bojian Jiang, A thesis submitted to the School in the partial fulfillment of the requirements for the degree of

**Master of Electrical Engineering/Faculty of Engineering and Applied Science/**

**Memorial University of Newfoundland**

**May 2019**

St. John's Newfoundland and Labrador

# Abstract

Hybrid power systems include both renewable and traditional energy. In China, some rural areas not connected to the grid are more suitable for isolated hybrid power systems than grid extension, because of lack of roads and infrastructures. Government's policies have largely boosted the development of renewable energy, making the hybrid power system more affordable for those areas.

In this research, the system is firstly sized for optimum net present cost using HOMER according to given weather data and generated hourly load data. Then, the transient stability of the designed system is checked through the dynamic modeling and simulation in Simulink based on each component's dynamic equations and control system. Designed control systems, which keep the stable operation of the designed system, include a supervisory controller, MPPT (Maximum Power Point Tracker), inverter controller and so on. Due to nonlinear and time variant load, the controller of the DC voltage regulator is designed based on a robust control method. A data logger with web transfer is then designed to monitor an isolated PV system. Sensor data are collected by Arduino boards and transferred to Thingspeak web server by the python program on PC. The collected data is downloaded and analyzed on MATLAB to analyze the system operation. Therefore, this thesis presents system sizing, dynamic modeling and its simulation results, a data logging system with data visualization on a web server and lab test results.

# Acknowledgment

Firstly, I am very grateful for the continuous support of Dr. Tariq Iqbal. His timely instructions and advice always give me inspiration and courage when I am stuck in my research. I have an appreciation for the patients of Dr. Siu O'young, which helps me understand new knowledge during his graduate course. I am very thankful for the support from Mr. Greg O'Leary for his support during the lab. The author also gives special thanks to Dr. Wayne Raman-Nair and Dr. Cynthia Coles for their graduate courses.

I am also thankful for the support and help from my parents and my friends during my graduate studies.

I am very appreciated for the financial support from Gansu Liujiaxia Hydro-Electric Joint Ind. Co., which enables me to finish the graduate study.

# Table of Contents

# List of Figures and Tables

# List of Abbreviations

| | |
|---|---|
| DC | Direct Current |
| AC | Alternative Current |
| MPPT | Maximum Power Point Tracker |
| ESR | Equivalent Series Resistance |
| DCR | Direct Current Resistance |
| PID | Proportion Integration Derivative |
| PI | Proportion Integration |
| R | Resonance |
| CCF | Capacitor Current Feedback |
| PV | Photovoltaic |
| P&O | Perturbation and Observation |
| CP&O | Current Perturbation and Observation |
| PLC | Programmable Logic Controller |
| VAT | Value Added Tax |
| USD | United State Dollars |
| CAD | Canadian Dollars |
| SOC | State of Charge |
| IGBT | Insulated-Gate Bipolar Transistor |
| LC | Inductor and Capacitor (Resonant Circuit) |
| TDC | Time Delayed Control |
| PC | Personal Computer |
| URL | Uniform Resource Locator |
| USB | Universal Serial Bus |
| RMS | Root Mean Square |

# Chapter 1

# Introduction and Literature Review

## 1.1 Development of an Isolated Hybrid Power System in China

According to Manwell et al. [1], hybrid power systems include traditional generation and at least one renewable generation. There are grid-connected and isolated hybrid power systems, which are connected and disconnected to power grids respectively. Since feed-in tariff is not allowed for individual residences in China, the grid-connected systems cannot supply excessive power to the grid and get profits [4]. Thus, only the literature for isolated hybrid power systems in China is presented.

In remote areas, diesel generators are the primary or only power source, which requires continuous diesel supply all the time [1]. The difficult transportation in these areas also increases the cost of grid extension. The diesel consumption results in the air pollution and substantial financial burdens to purchase, transport and store of the diesel in these areas. Therefore, hybrid power systems including only renewable energies or both diesel and renewable energy are designed for these areas to minimize diesel consumption or substitute for grid extension [1]. Compared to renewable hybrid power systems, the hybrid power systems based on diesel energy can supply the remote communities more reliably because of diesel energy for backup.

Currently, only isolated renewable hybrid power systems for the houses in urban areas are studied in China, like the wind/solar/battery hybrid power system for a house in Urumqi [2]. The designed system can adequately supply the load throughout the simulation, but it does not consider the negative environmental effects (turbulences and shades) that can decrease renewable generations in urban areas [3]. Because there is no diesel generator for backup, this system could fail to supply the load when the battery storage is used up during long-time undesired weather conditions. Fangqiu Xu et al. designed an off-grid wind power farm with battery storage for a remote community in

Heibei Province in China [5]. The authors optimized the system with the goals to maximize annual profit and minimize wind power curtailment. This research shows a profitable and reliable isolated renewable hybrid power system for a rural community in China. Currently, some Chinese companies are producing isolated renewable hybrid power systems (figure 1.1) and export them to foreign countries. However, most systems are not diesel based and thus could fail during long-time undesired climate.

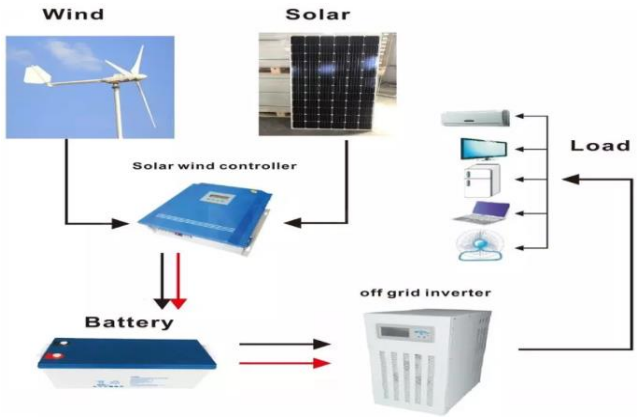


Figure 1.1 Isolated Hybrid Power System Produced in China [6]

## 1.2 Development of Traditional Energy in China

Traditional energy, such as crude oil, natural gas, and coal, is still the main power source in China, in which coal takes 62% energy consumption in 2016 [7]. Because China takes 23.2% global energy consumption, the intensive coal consumption can result in severe air pollution both in China and the whole earth [7]. Thus, Chinese government formatted laws and policies to ensure the efficiency of traditional energy and limit their greenhouse gas emission, such as Law on Electric Power, Law on the Coal industry and so on [7]. This can increase the investment of coal production and environmental management, which combined with the decreasing storage of coal can further increase the price of coal and make renewable energy more attractive in China in the future [3].

## 1.3 Development of Renewable Energy in China

Although Chinese renewable energy resources are not the most abundant, the development of renewable energy in China is the fastest in the world [4]. This is because

of the supportive government policies, such as reductions in sales, energy and VAT taxes and so on [4]. These policies increase the demand and production of renewable generation devices and decrease the cost of renewable energy devices. The costs of renewable energy, therefore, keep decreasing in recent years. In 2016, the maximum levelized costs of on-shore-wind and solar energies were 0.155 USD/kWh and 0.07 USD/kWh respectively in China [4]. This helps renewable energy becoming more affordable for people living in rural areas in China.

## 1.4 System Sizing for Hybrid Power System

System sizing aims to design a reliable and economically reliable system based on local weather data and hourly load data. The optimum design aims to minimize the Present Net Cost and Levelized Cost of energy [9]. By now there are many software programs for this purpose, such as SAM, HOMER, RAP-SIM and so on, in which the optimum sizing results come out instantly after designing system and entering data [9]. According to Lose´ and Rodolfo [9], SAM is specifically designed for economic analysis and cannot design hybrid power systems, RAP-SIM has more design functions (even dynamic simulation) but needs to be paid, HOMER is free and functional and more widely used. HOMER determines the economically optimum design and checks the pre-feasibility of the system according to users' requirements and entered data [9]. This is completed in the user interface shown in figure 1.2, in which sensitivity analysis can also be included, to make the system design more practical [10].

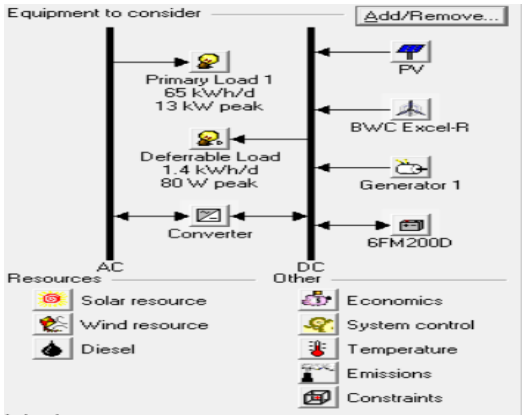


Figure 1.2 User Interface in HOMER

## 1.5 Dynamic Modeling and Simulation of Hybrid Power System

Dynamic modeling and simulation check the transient dynamics of the designed system under possible inputs and disturbance in reality. The dynamic model of a hybrid system consists of the dynamic model based on each component's mathematic equations and the control systems that are designed to stabilize the whole system [1]. The detailed literature review for these two parts is shown in section 1.5.1 and 1.5.2 below.

### 1.5.1 Dynamic Model of Hybrid Power System

#### 1.5.1.1 Dynamic Model of Wind Turbine

A wind turbine transforms the kinetic power of the wind into mechanical power by its rotor and blades, this mechanical power is then sent to its generator by its drive train, and the generator transforms the mechanical power into electrical power [11]. The model in [1] considers all three processes above. In comparison, the model developed by Khan et al. [12] simplifies the first two process by digitalizing its wind power curve from the manufacturer into the Simulink model, which largely saves simulation time. Such a model is suitable to describe the dynamics of small wind turbines without pitch control [1]. For large turbines with pitch control, the model from [13] is more suitable, which includes a detailed aerodynamic model of large wind turbines. This enables the pitch control of the wind turbines. The pitch control turns the pitch angle of a blade by a pitch actuator, which can be described by the 1$^{st}$ order system in [14]. The generators in small turbines and large turbines are permanent magnet generators and induction generators respectively, which are represented by a 2$^{nd}$ order transfer function in [12] and eleven algebraic & differential equations in [13]. Thus, the wind turbine needs to be carefully checked before modeling, to prevent large simulation error.

#### 1.5.1.2 Dynamic Model of PV Panel

One PV panel consists of many solar cells connected in series. Each cell is a photons sensitive semiconductor. When the photons in lights land on a solar cell, the energy of

these photons dislodges electrons of the semiconductor to the external circuit, which then forms the electrical current through the load [3]. The equivalent circuit of a solar cell is shown in figure 1.3.

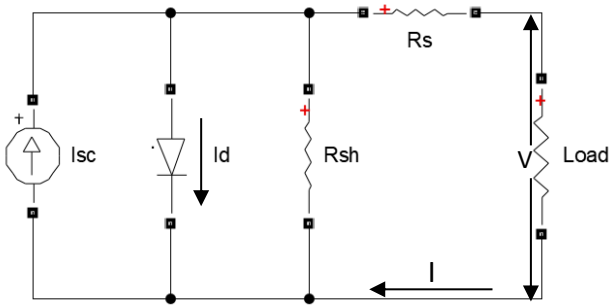


Figure 1.3 Equivalent Circuit of Solar Cell

Figure 1.3 shows that the load current (I) is solved by subtracting the photovoltaic current ($I_{SC}$) with the dark current ($I_d$) and current on the shunt resistor ($R_{sh}$). The load voltage (V) is decided by the resistance value of the load. This dynamic can be described by the simplified equations in [15]. However, this model neglects the temperature effect on its output voltage, which can lead to large simulation error. In the solar cell model from [13], this effect is described by the voltage-temperature coefficient, which can increase the simulation accuracy. More detailed and accurate dynamic models of a solar cell developed in [16, 17] are specifically designed to research its specific physic dynamics and calculate its shunt and series resistance respectively.

#### 1.5.1.3 Dynamic Model of Lead Acid Battery

Lead acid batteries are widely used as backup energy in current power systems because of their low price and stable performance. The voltage of a lead acid battery is proportional to its capacity during charging or discharging [1]. To accurately describe the dynamics of lead acid batteries, both the dynamics of battery capacity and battery voltage needs to be modeled [1]. The dynamic of the battery capacity is described by using available charge and the charge released at speed proportional to the rate constant, and the dynamic of the battery voltage is described by the relation between the internal

voltage and battery capacity [1]. However, the parameter-ratio of available charge capacity to total capacity must be derived from manufacture or lab test, which increases the modeling time of the battery [18]. In comparison, the model from [13] describes all dynamics above by only two equations without deriving any parameter by designers, which largely simplifies the modeling process.

#### 1.5.1.4 Dynamic Model of Diesel Generator

To research the dynamics of the wind-diesel hybrid power system, Theubou et al. [19] build a 3rd order state space model of the diesel generator by integrating the state space models of the prime mover, autonomous voltage regulator, and synchronous generator. The model is then tested under various eigenvalues in the situation of load rejection and shows excellent performances to keep stable operation. The model proposed by Hasan Asif [20], describes the dynamic of a diesel generator by a 1st order model with a 1st order frequency regulator. This model largely simplifies the global model of a hybrid power system and thus can be used to predict future performance. These two models are designed for AC diesel generator in AC coupled hybrid power systems. For a DC alternator in a DC coupled hybrid power system, the dynamic model in [13] can accurately describe its dynamics by only two 1st order equations with a few parameters. Its control system is a PID torque controller without considering voltage variation.

#### 1.5.1.5 Dynamic Model of DC Voltage Regulator

DC/DC boost converters are widely used to stabilize the DC voltage in hybrid power systems [21]. It both boosts up and stabilizes the DC bus voltage by its switching operation. Rick [22] derives the dynamic model of a boost converter by using partial derivatives on its state space model. This model can accurately describe its dynamics when a load of a boost converter is linear [22]. The values of the inductor and capacitor in the boost converter should be carefully chosen according to the procedure in [22], to avoid unsteady operation near maximum load supply. Ya-Xiong Wang et al. [23] describes the off-on operation of the switching device by using 1s and 0s in his boost

converter model. Compared to [22], this model is closer to the real operation of a boost converter and can be applied in its nonlinear controller design such as the slide-mode controller design in [23].

#### 1.5.1.6 Dynamic Model of Single-Phase Inverter

Currently, the widely used single-phase inverter is the full-bridge inverter, due to its high efficiency in high power applications [24]. El-Sharkh et al. [40] build a simple model for the full-bridge inverter, which only includes one algebraic equation for output voltage and another for output power. This model cannot describe the switching operation of the inverter, which is the main reason for the deformation of its output voltage. Xiao Liu et al. [25] and Yanbo Che et al. [26] develop inverter models by using the generalized average method, which represents the instantaneous variables in the state space model with their quasi-Fourier representation. These two models can therefore accurately represent the switching operation of the inverter. Compared to the model in [26], the one developed by Xiao Liu et al. [25] can more accurately represent the ripple-magnitude variation by using sideband components.

### 1.5.2 Control System for Hybrid Power System

#### 1.5.2.1 Supervisory Controller

The control systems in [11, 27] both include a supervisory controller, which manage the balance among the power generation, energy storage and load. Once the generated power is lower than the load power, the backup generator will be switched on to charge the energy storage and supply the load; otherwise, the backup generator will be switched off. The system can thus stably supply the load and prevent the energy storage from overdischarging and overcharging. In comparison, the supervisory controller in [11] is on-off control. This is easier to be implemented than the one in [27], which has a complicated process to calculate reference values to control its energy storage, backup generator, dump load and so on.

1.5.2.2 Controllers for Wind Turbine and PV Array

According to [11], there are two different PID controllers (shown in figure 1.4). One is a torque controller that controls the output power of the generator, and another is a pitch controller that maximizes the output power through pitch control.

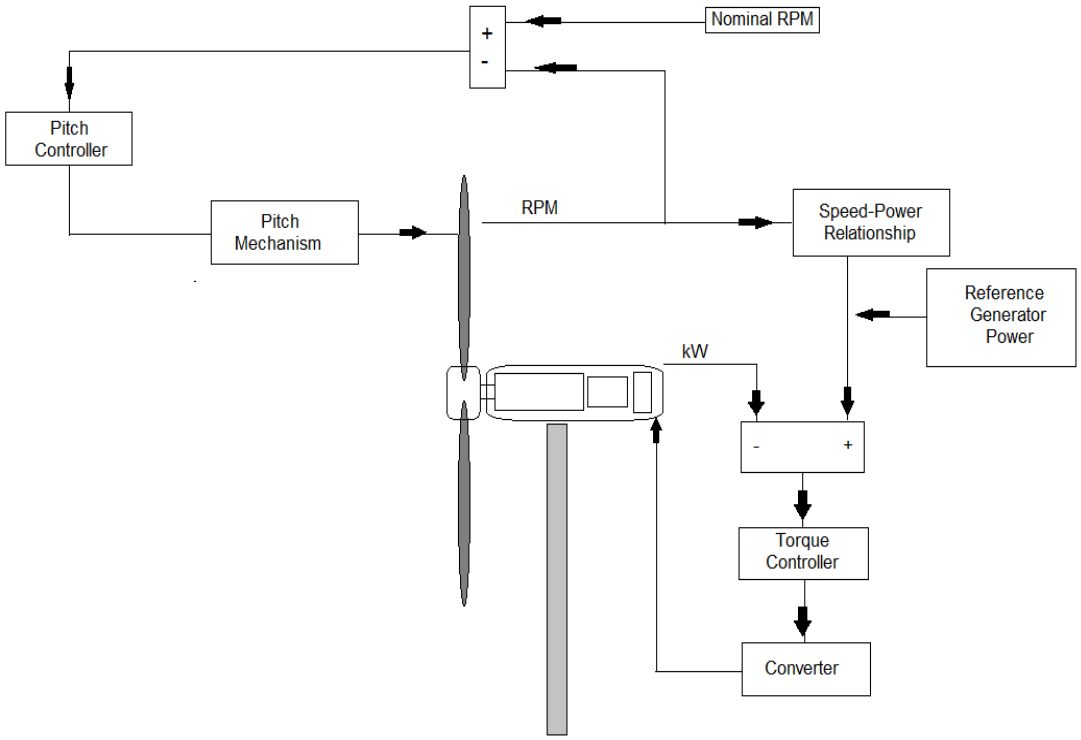


Figure 1.4 Control System of Wind Turbine

In order to maximize the power output of a PV array, Milana et al. designed a CP&O (current perturbation and observation method) controlled MPPT to reach the maximum output power of a PV array, which is realized by periodically adjusting the output current of the PV array [11]. Voltage P&O method, however, is more widely applied in reality [28]. It adjusts the output voltage of a PV array by periodically increasing (decreasing) the output current of a PV array, based on the change of its output power in each step (figure 1.5) [28].

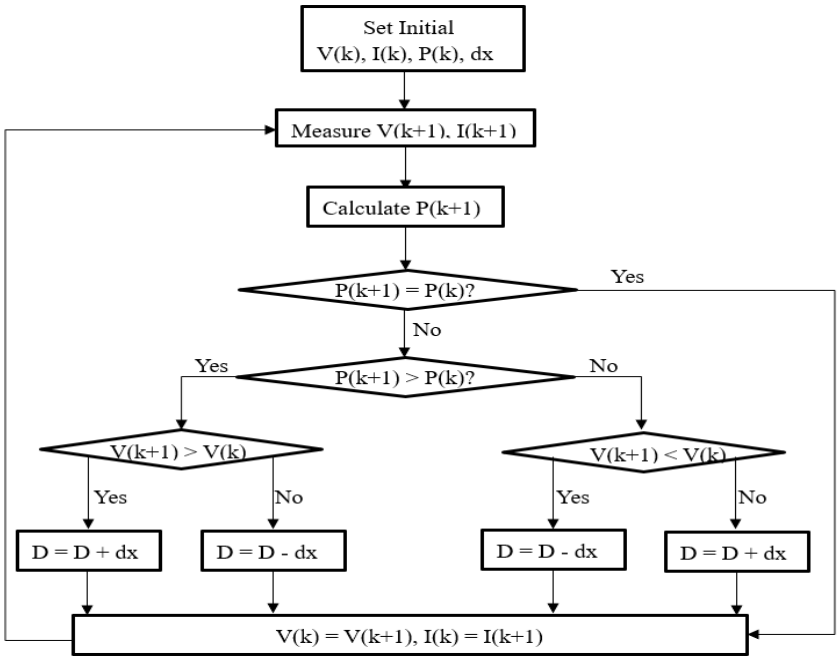


Figure 1.5 Flow Chart of Voltage P&O Method

However, the constant step size of the duty ratio leads to the power oscillation around maximum power in P&O controlled MPPT [28]. This can be overcome by the incremental conductance method that uses the induction of output power to decide the step size the duty ratio, which is shown in the red circle in figure 1.6 below [29].

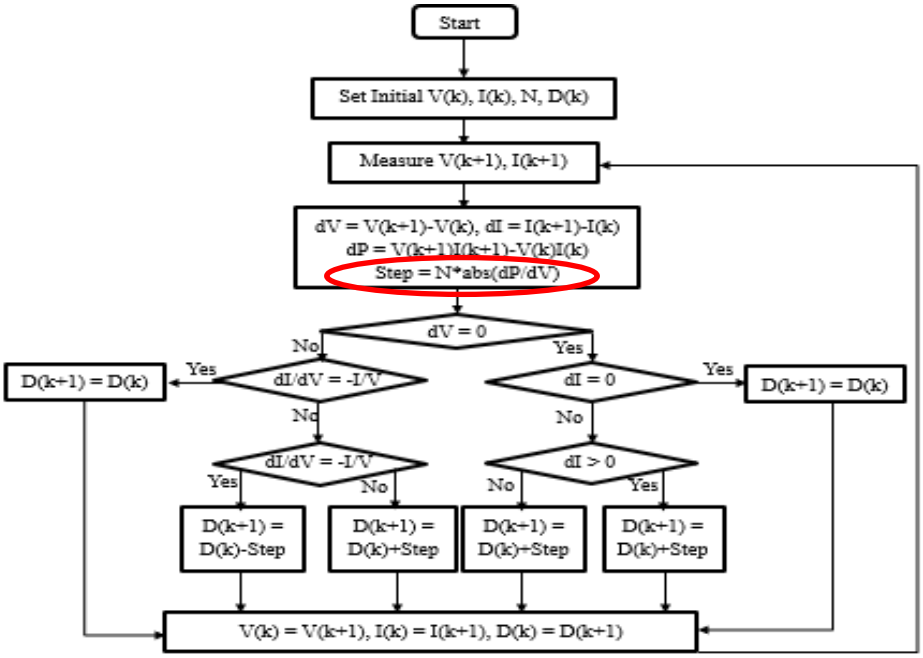


Figure 1.6 Flow Chart of Incremental Conductance Method

As it is shown in figure 1.6, the duty ratio is increased when the inductance is positive, the duty ratio is decreased when the inductance is negative, and the absolute value of the inductance decides the duty ratio's step size [29]. The step size is close to zero when the power is near to the maximum power, and larger than zero when the power is much less [29].

#### 1.5.2.3 Controller for Single Phase Inverter

For users who need low power quality, a Proportion Integration (PI) voltage controller is enough to control the inverter output voltage. This method compares the inverter output voltage with the standard reference sinewave and sends the error signal to the PI controller, which then outputs the control signal to modulate the inverter [24]. As the power-quality requirement of electrical appliances keeps increasing, this controller is no longer enough. According to Zhaoan Wang et al. [24], control methods, such as hysterical comparison method, timing comparison method and triangular-wave comparison method are developed to control an inverter. Only hysterical comparison method can realize closed-loop voltage tracking and decrease waveform deformation at the same time [24]. This method decreases the switching frequency when the output voltage is larger than $V_{ref} + \Delta V$, and increases the frequency when the voltage is less than $V_{ref} - \Delta V$ [24]. This increases the high frequency harmonics of the output voltage, and requires an additional lowpass filter after the inverter [24]. The above control methods have poor transient performance at transient load transitions [30]. According to Dong Dong et al. [30], an addition inner current loop and voltage resonance controller are required in the control system to stabilize the inverter output voltage under transient load transition.

#### 1.5.2.4 Controller for DC Voltage Regulator

Typically, the load of the DC voltage regulator is a linear load with small variation. The dynamics of the regulator can then be accurately described by the control-voltage transfer function in [31], and build a well performed PID voltage controller based on

that model. However, in hybrid power systems the load is nonlinear and time variant, which leads to poor performances of the PID voltage controller. Time-delayed control, one of the robust control methods, is a good option to deal with nonlinear time variant dynamics [32]. According to Ya-Xiong Wang et al. [23], the time-delayed control shows simple design processes and better performances to control a DC/DC boost converter than the PID voltage control, slide-mode control, and model predictive control. The fuzzy logic control of a boost converter designed by Nik Ismail et al. [32] shows an even simpler design process, which only needs the general knowledge of the converter without building the detailed mathematic model.

## 1.6 System Monitoring for Isolated Hybrid Power System

For an isolated hybrid power system, it is necessary to monitor the operation of the system when its users are away from the location. Hegazy et al. [33] and Francisco et al. [34] use a data-acquisition device and PLC (Programmable Logic Controller) respectively as the data loggers. The sensors in a hybrid power system such as temperature sensors, current sensors, and voltage sensors, are far away from each other. If they are connected by cables, the system could easily become disordered increasing the difficulty of its maintenance [35].

Farid Touati et al. [35] solve the problem by using XBee, which is a wireless network protocol. Although the power consumption of XBee is pretty low [36], the transmission range of XBee is less than 100m, which is much smaller than Lora and radio frequency transmission. According to Terashimila et al. [37], Lora or radio frequency is a good option, which can achieve reliable communication within 5km and 1km respectively.

## 1.7 Thesis Objectives

This literature review failed to find any design of hybrid power systems for a remote home in China. Detailed system design and system information are missing in the literature. The detailed information of the data logging system, robust web transfer and data visualization for an isolated hybrid power system are also not found in the literature. Thus, this thesis designs and presents an isolated hybrid power system, which includes system sizing, dynamic modeling and simulation and the design of the data logging system, for a remote house in China. The objectives of the research are listed as follows:

a) Design a reliable hybrid power system for a remote location in China based on the weather data, load data and building architecture of that location. Size the designed system for the final optimum design with high renewable penetration and minimum system cost.

b) Build a dynamic model of the final sized system in Simulink, and develop a control system, which includes both individual controllers and the global supervisory controller, to keep the system model operating as it is designed.

c) Simulate the designed dynamic model under the extreme conditions that would happen in real-time operation, and analyze the transient dynamics of the system based on the simulation results.

d) Design a low-cost data logging system for an isolated power system with wireless communication among sensors. Develop a robust data transfer that sends sensor data from data loggers to a web server that can visualize and monitor the system operation when the users are away from the location. Analyze the collected data to check the system operation during the test.

## 1.8 Thesis Organization

Chapter 1 is the introduction of a hybrid power system, the development of renewable energy in China, project background, and literature review of previous studies. Chapter 2 presents the process of system sizing, including weather data collection, load data generation in BEopt and system optimization in HOMER. Chapter 3 describes the dynamic modeling of the hybrid power system based on the sizing result in chapter 2. Time-delayed controller for the DC voltage regulator to stabilize the inverter input voltage is also presented. Chapter 4 talks about the hardware and program of the data logging system of a PV system. The data analysis of the collected sensor data in MATLAB is also presented at the end of this chapter. The reference section contains all sources of information including the literature review. Codes and other related material are directly shown in the pictures and tables from chapter 2 to chapter 4.

# Chapter 2

# System Sizing

## 2.1 Introduction

In some rural areas in the northwest of China, people are suffering from large voltage drop due to the distance from the grid. Recently, the price of solar and wind energy has declined drastically in China due to the government policy of renewable energy. The price of solar panels is also declining very fast. Shortly isolated hybrid power systems could be very affordable by the users who live in those areas (where net metering is not allowed). Before it becomes a reality, it is necessary to size a system based on local load data and weather condition. The processes of system sizing include weather data collection, load simulation, and system sizing. This chapter will first introduce the current development of renewable energy in China, then go through those processes in detail.

## 2.2 Pre-Feasibility Study of Hybrid Power System

In some rural areas in Qinghai province, which is located in northwestern China, people suffer from the voltage drop over 5% of the rated voltage due to long-distance power transmission. Therefore, their power quality and stability are not maintained as a high degree as urban areas. Furthermore, the maintenance of the power supply system is both costly and time-consuming for power companies because of the poor transportation in these rural areas. Independent renewable power generation is a good alternative when there are abundant renewable energy resources and affordable devices in these areas. Because of the high altitude, there are abundant renewable energy resources in this province, which is shown in figure 2.1 and 2.2 below.

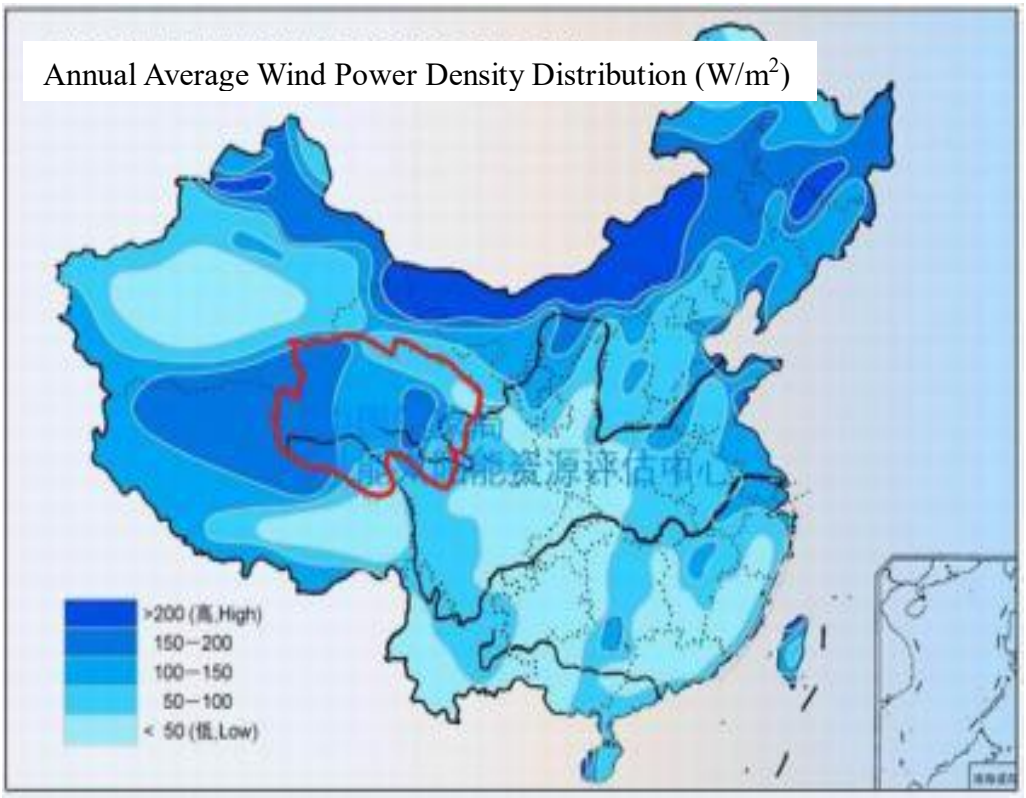


Figure 2.1 Annual Average Wind Power Density Distribution in China (W/m$^2$) [38]

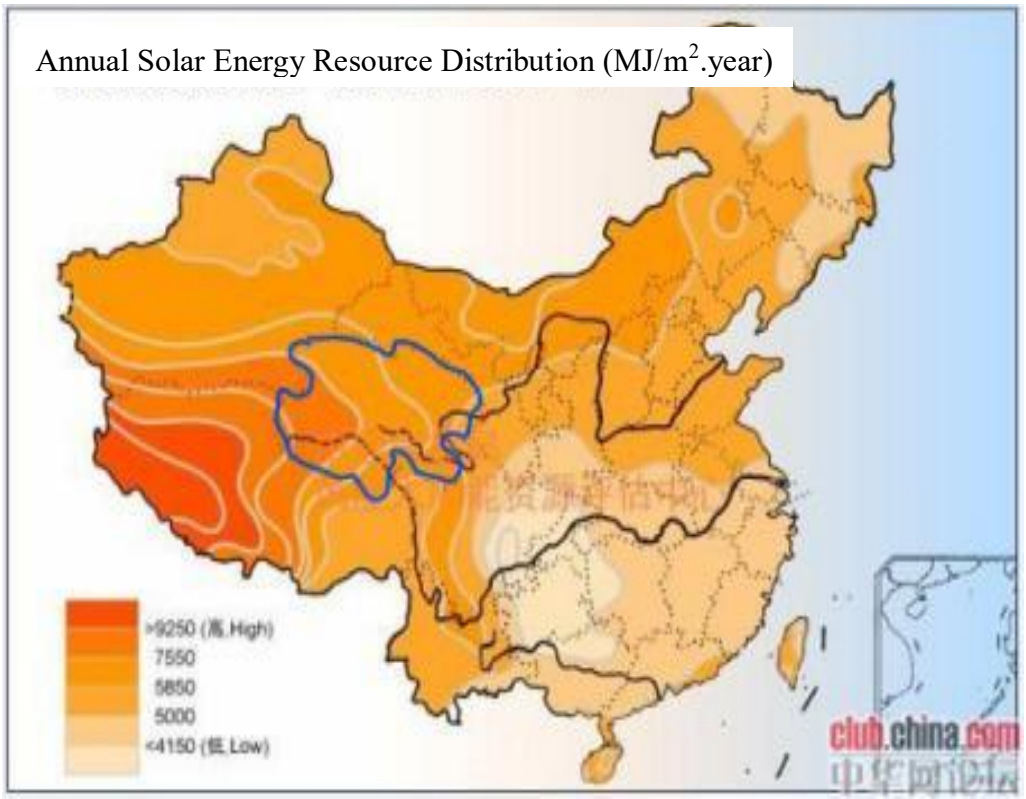


Figure 2.2 Annual Solar Energy Resource Distribution in China (MJ/m$^2$.year) [39]

Figure 2.1 and figure 2.2 show that the annual average wind power density and annual solar resource of Qinghai province (enclosed by red lines) are about 100-200 W/m$^2$ and 5000 MJ/m$^2$.year respectively. This means a great potential for renewable generation in Qinghai Province. Besides that, government policies, like Reductions in Sales and Energy and VAT Taxes, also play an important role in developing renewable energy [4]. In 2016 the installed renewable energy in China took the largest part of the world, which can be seen from figure 2.3 below. This decreases the price of renewable energy. The levelized cost of solar and onshore-wind power are 0.075-0.155 USD/kWh and 0.05-0.07 USD/kWh respectively in China [4]. If the government policies kept in place, the price of solar and wind power will continue to decrease, which could make the isolated renewable energy system affordable for this area.

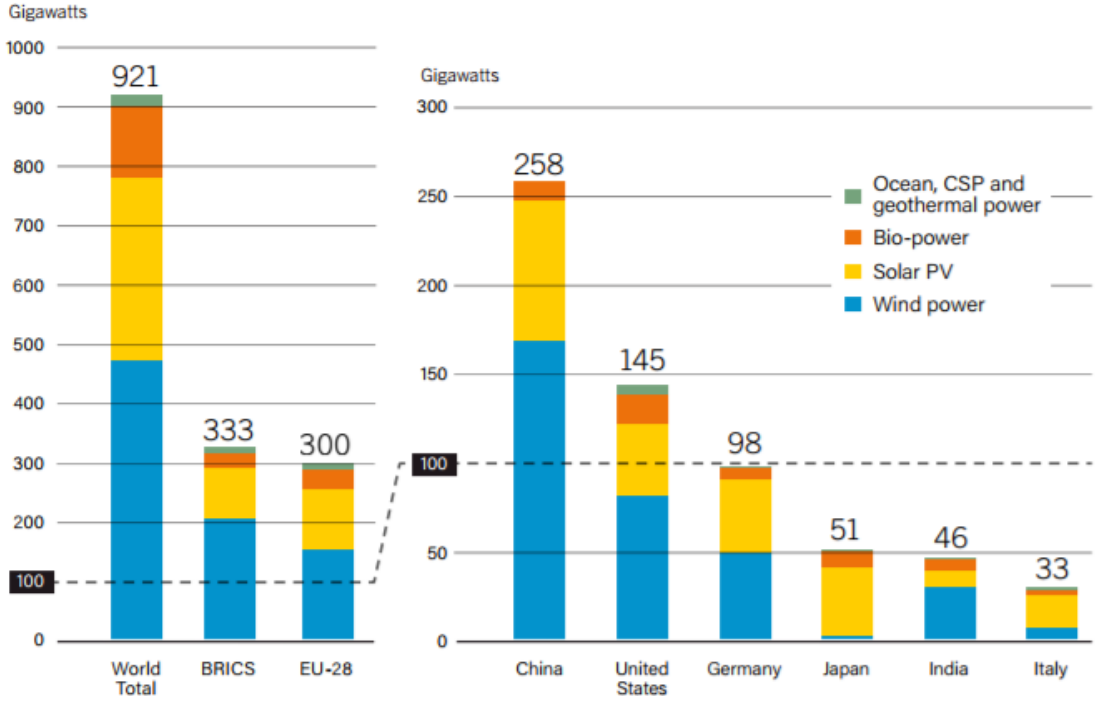


Figure 2.3 Renewable Power Capacity Comparison [4]

However, the economy of the system must be based on its reliability to supply the load. Before checking the reliability of the system, it is necessary to collect the weather data and generate load data based on the location of the system and the building architecture of the location.

## 2.3 Site Location, Renewable Energy Resource, and Load Data Generation

### 2.3.1 Site Location

The site is located at a remote area in Qinghai province, and its coordination is 37º50'N, 101º58'E. The building (enclosed in the red rectangular) and peripheral topography of the location are shown in figure 2.4 below.

Figure 2.4 Building Architecture and Topography around Site

It can be seen from figure 2.4 that there is no obstacle around the site, which means that there are little turbulence and shade for wind turbines and PV arrays. More power could be therefore harvested from wind and solar energy resources.

### 2.3.2 Climate Data of Selected Location

The renewable resources are the power sources of renewable power generation. Wind speed and solar radiations are the power sources of wind turbines and PV arrays. Monthly average values of wind speed and daily solar energy are provided in figure 2.5 and 2.7 respectively. Since the ambient temperature is disproportional to the power output of the PV array, the monthly average ambient temperature is provided in figure 2.8. Except for the temperature data collected from [40], these weather data are automatically collected in HOMER software by inputting the coordination of the selected location.

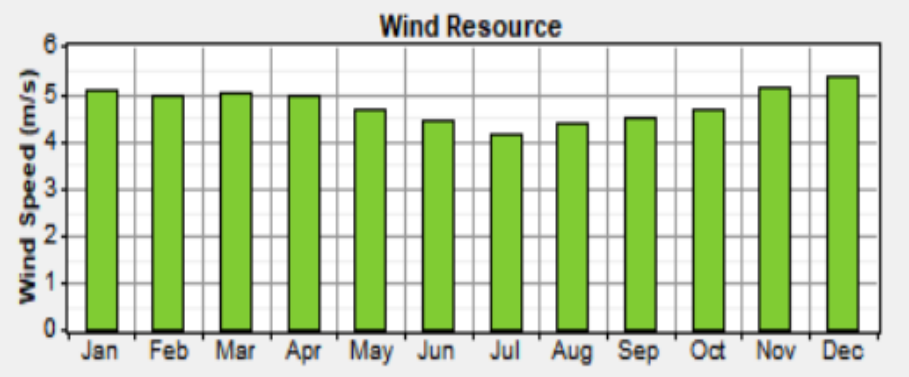


Figure 2.5 Monthly Average Wind Speed

Figure 2.5 shows that the distribution of the wind speed is stable over the year, which means the stable power output of wind turbines in this location. According to the duration curve of the wind speed in figure 2.6, the hours when the wind speed exceeds 3m/s are more than 6000 hours. This means that the annual effective wind power density of the location is larger than 200W/m$^2$, so this location is suitable for wind power generation [41].

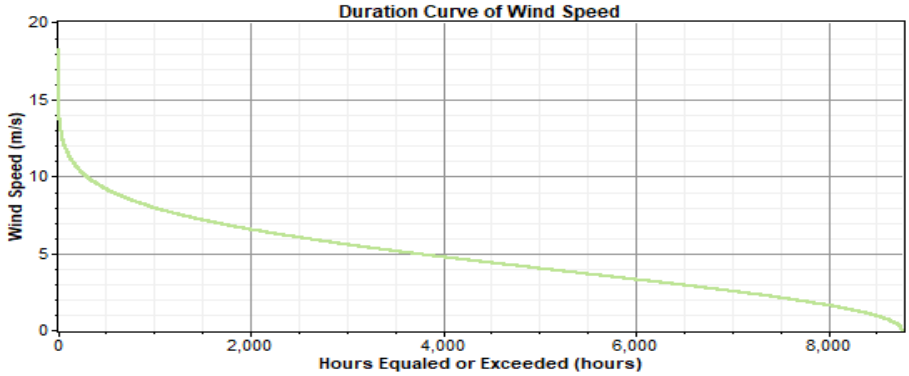


Figure 2.6 Duration Curve of Wind Speed

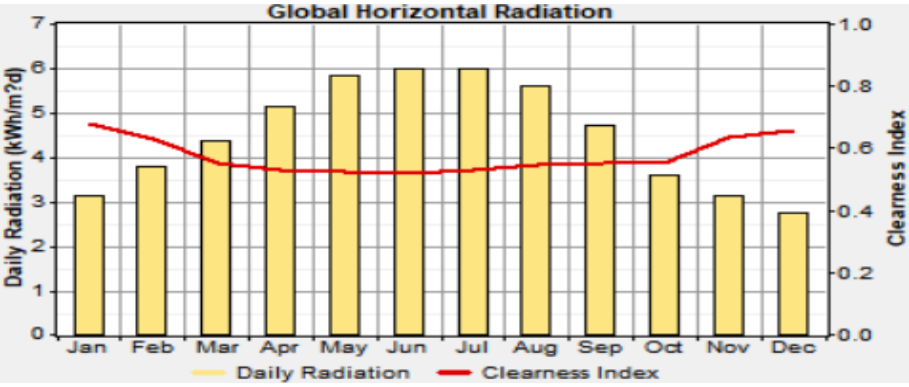


Figure 2.7 Monthly Average Daily Solar Radiation

Figure 2.7 shows that the solar radiation in summer, late spring and early autumn is higher. This is because the angle between solar radiation and the horizontal surface is closer to 90° when it is around summer. The solar radiation travels a shorter distance to reach the earth surface, and less radiation gets diffused. The average daily solar irradiance is 4.51kWh/m$^2$.day, which means a large amount of solar energy resource in this location.

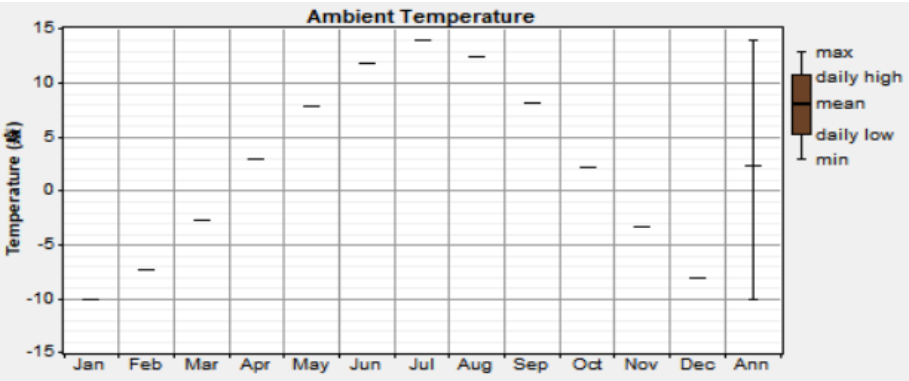


Figure 2.8 Monthly Average Ambient Temperature

Figure 2.8 shows that the temperature of the location changes along with solar radiation. The monthly average temperature reaches its maximum value (14℃) in the middle of the summer. The annual average temperature is 2.33℃. This low temperature helps increase the output power of the PV array, because of the disproportion relationship between the temperature and PV output power.

### 2.3.3 Prime Load Data Generation

Since hourly load data cannot be provided by Chinese power companies, the specific software is used to generate the hourly load, such as Energy3D and BEopt. Thermal loads (cooling and heating) take the largest part of the total load. BEopt is more suitable for the precise load generation of the house since it has the weather data of the location and the options for insulation materials. The parameters of the house model in BEopt are shown in table 2.1 below.

| Options | Value |
|---|---|
| R Value of Walls | 0.43 h-ft$^2$-R/Btu |
| R Value of Ceiling & Roof | 4.4 h-ft$^2$-R/Btu |
| R Value of Windows | 2.63 h-ft$^2$-R/Btu |
| Window Areas | 207 ft$^2$ |
| R Value of Door | 2.08 h-ft$^2$-R/Btu |
| Door Areas | 20 ft$^2$ |
| Foundation & Floors | 2.08 h-ft$^2$-R/Btu |
| Exterior Wall Mass | 0.42 Btu/F-ft$^2$ |
| Partition Wall Mass | 0.42 Btu/F-ft$^2$ |
| Ceiling Mass | 0.42 Btu/F-ft$^2$ |
| Internal Shading | 0.7 |
| Ventilation | Natural Ventilation 7 days/Week |
| Room Air Conditioner | 8.5 Btu/W-h |
| Electricity Baseboard Efficiency | 100% |
| Cooling Setpoint | 77F |
| Heating Setpoint | 63F |
| Water Heating Setpoint | 125F |
| Hot Water Distribution | Copper, Uninsulated |
| Lighting | 100% LED |
| Refrigerator Energy Consumption | 718 kWh/year |
| Cooking Energy Consumption | 500 kWh/year |
| Dishwasher Energy Consumption | 111 kWh/year |
| Clothes Washer Energy Consumption | 42.9 kWh/year |
| Dryer Energy Factor | 3.1 lb/kWh |
| Plug Loads | 2152 kWh/year |

Table 2.1 Parameters of House Model in BEopt

The house model in BEopt based on the architecture in figure 2.4 is the typical architecture in the selected area, which is shown in figure 2.9 below. The resulted annual hourly load data is shown in figure 2.10.

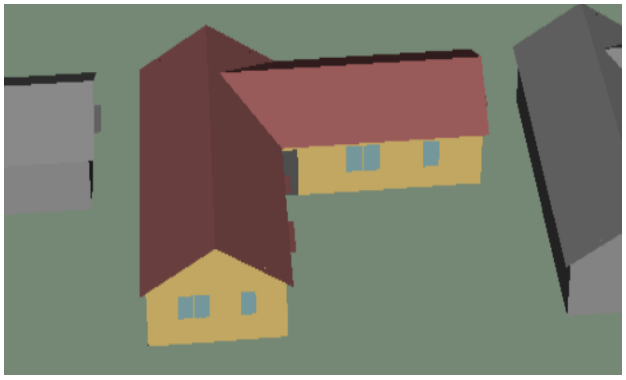

Figure 2.9 Building Model in BEopt

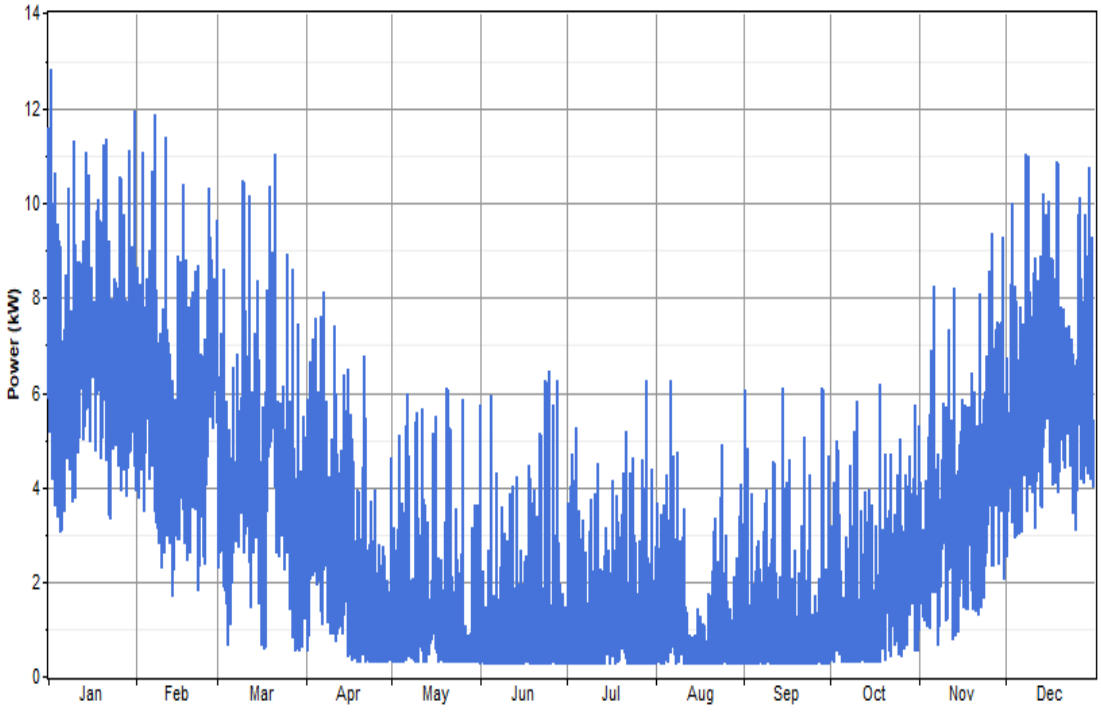


Figure 2.10 Annual Hourly Load Data in BEopt

According to figure 2.10, the load is the lower in summer and higher in winter. During summer, although the monthly average temperature is the highest among the year, its value is below 14℃. The cooling demand of the site is thus lower in summer. In comparison, the temperature in winter is around -10℃. The heating demand of the location, therefore, is very high and results in a higher hourly load in winter. The maximum load power is 12.8kW, and the annual average hourly load power is 2.73kW.

### 2.3.4 Deferrable Load Data

The input data include not only the weather and load data discussed above but deferrable load data. This deferrable load data represents the water-pumping load since it can be substituted by human-power lifting. The power needed for water pumping is calculated based on the equations below [42]:

$$H_{dynamic} = Vertical\ Lift + Friction\ Loss + Tank\ Pressure \quad (2.1)$$

$$Required\ Solar\ Power = \frac{\rho m g H_{dynamic}}{0.7\eta_{PV}\eta_{mppt}\eta_{BB}\eta_{PM}} \quad (2.2)$$

Where $H_{dynamic}$ is the dynamic head of the water pump, $\rho$ is the density of the water, $m$ is the weight of the water, $\eta_{PV}$ is the efficiency of the PV array, $\eta_{mppt}$ is the efficiency of the MPPT, $\eta_{BB}$ is the efficiency of the battery storage, $\eta_{PM}$ is the efficiency of the pump motor.

The resulted monthly data of the deferrable load is shown in figure 2.11 below.

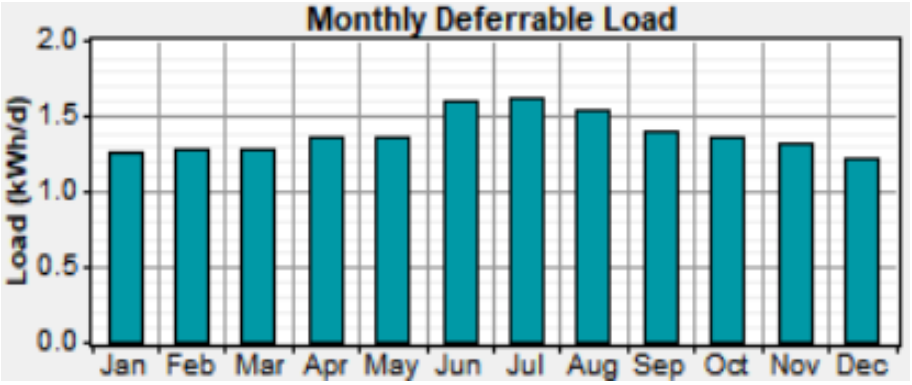


Figure 2.11 Monthly Deferrable Load

## 2.4 System Sizing

The system sizing is done through HOMER 2.68. This software is used for power system design, system sizing, and system economy check. The whole process is discussed in the sections below.

### 2.4.1 System Configuration

The initial system design in HOMER is a DC coupled system, which is easier to control and more robust than AC coupled systems. The initial system includes wind turbines, PV panels, a diesel generator, inverter, battery storage, and AC load. The wind turbine and PV array transfer the wind and solar energy resource into electrical power. The electrical power is then supplied to the battery storage and load.

The diesel generator generates power when the power generated by the PV array and wind turbine cannot supply the load. The loads include the AC primary load and deferrable load, representing the energy for normal daily use and water pumping. The system configuration is shown in figure 2.12 below.

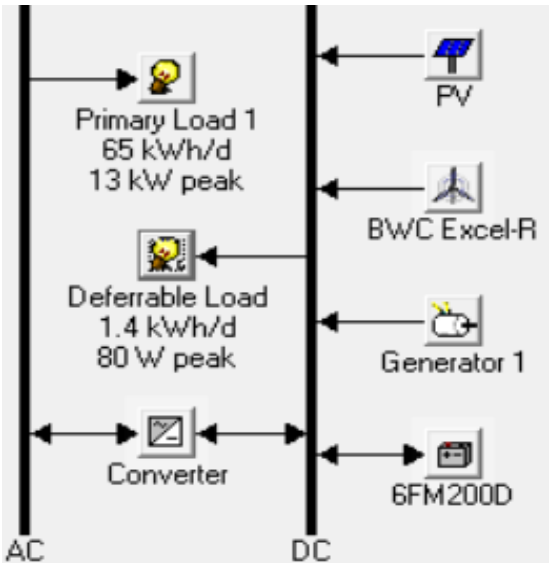


Figure 2.12 Initial Hybrid Power System Design

### 2.4.2 System Sizing

System Sizing is automatically done by HOMER after giving all required data and initial system design. HOMER checks the system whether it can supply the load in each hour of the year. HOMER then compares the economics of all capable hybrid power systems and lists them in the order of economics. The final system sizing result is shown in figure 2.13 below.

Sensitivity Results | Optimization Results

Double click on a system below for

Categoriz | Overall

| PV (kW) | XLR | Label (kW) | 6FM20... | Conv. (kW) | Disp. Strgy | Initial Capital | Operating Cost ($/yr) | Total NPC | COE ($/kW... | Ren. Frac. | Diesel (L) | Label (hrs) |
|---|---|---|---|---|---|---|---|---|---|---|---|---|
| 13.... | | 8 | 20 | 15 | CC | $ 28,595 | 10,187 | $ 158,824 | 0.509 | 0.62 | 4,666 | 1,867 |
| 13.... | | 8 | 20 | 15 | CC | $ 27,935 | 10,250 | $ 158,968 | 0.509 | 0.60 | 4,726 | 1,893 |
| 13.... | | 8 | 24 | 15 | CC | $ 30,195 | 10,074 | $ 158,977 | 0.510 | 0.62 | 4,537 | 1,811 |
| 13.... | | 8 | 24 | 15 | CC | $ 29,535 | 10,140 | $ 159,162 | 0.510 | 0.61 | 4,600 | 1,831 |
| 13.... | | 8 | 16 | 15 | CC | $ 26,995 | 10,354 | $ 159,357 | 0.511 | 0.61 | 4,881 | 1,969 |
| 13.... | | 8 | 16 | 15 | CC | $ 26,335 | 10,421 | $ 159,545 | 0.511 | 0.59 | 4,934 | 1,989 |
| 13.... | | 8 | 28 | 15 | CC | $ 31,795 | 10,003 | $ 159,665 | 0.512 | 0.63 | 4,466 | 1,779 |
| 10.... | 1 | 7 | 20 | 15 | CC | $ 50,995 | 8,513 | $ 159,818 | 0.512 | 0.73 | 3,439 | 1,510 |
| 11.... | 1 | 7 | 16 | 15 | CC | $ 50,055 | 8,591 | $ 159,876 | 0.512 | 0.73 | 3,555 | 1,573 |
| 11.... | 1 | 7 | 20 | 15 | CC | $ 51,655 | 8,467 | $ 159,890 | 0.513 | 0.74 | 3,382 | 1,482 |
| 13.... | | 7 | 48 | 15 | CC | $ 39,495 | 9,422 | $ 159,944 | 0.513 | 0.65 | 3,989 | 1,736 |
| 10.... | 1 | 7 | 16 | 15 | CC | $ 49,395 | 8,648 | $ 159,950 | 0.513 | 0.72 | 3,617 | 1,604 |
| 13.... | | 8 | 28 | 15 | CC | $ 31,135 | 10,084 | $ 160,038 | 0.513 | 0.61 | 4,541 | 1,806 |
| 9.92 | 1 | 7 | 20 | 15 | CC | $ 50,335 | 8,593 | $ 160,188 | 0.513 | 0.72 | 3,515 | 1,545 |
| 9.92 | 1 | 7 | 16 | 15 | CC | $ 48,735 | 8,719 | $ 160,188 | 0.513 | 0.71 | 3,680 | 1,630 |
| 9.30 | 1 | 7 | 16 | 15 | CC | $ 48,075 | 8,788 | $ 160,414 | 0.514 | 0.70 | 3,750 | 1,663 |
| 13.... | | 8 | 32 | 15 | CC | $ 33,395 | 9,941 | $ 160,480 | 0.514 | 0.63 | 4,394 | 1,748 |
| 9.30 | 1 | 7 | 20 | 15 | CC | $ 49,675 | 8,668 | $ 160,485 | 0.514 | 0.70 | 3,611 | 1,595 |
| 9.92 | 1 | 7 | 12 | 15 | CC | $ 47,135 | 8,867 | $ 160,485 | 0.514 | 0.70 | 3,907 | 1,759 |
| 10.... | 1 | 7 | 24 | 15 | CC | $ 52,595 | 8,441 | $ 160,494 | 0.514 | 0.74 | 3,334 | 1,461 |
| 11.... | 1 | 7 | 24 | 15 | CC | $ 53,255 | 8,396 | $ 160,582 | 0.515 | 0.75 | 3,275 | 1,434 |

Figure 2.13 System Sizing Result

The result shows that the 1st and 8th systems are the two most economical systems, and the 1st one is more economical. Figure 2.10 shows that the load is much higher than in winter, early spring and late autumn. Figure 2.5 shows the wind speed in winter, late autumn, and early spring. In comparison figure 2.7 shows the solar irradiance is lower during the same period. According to figure 2.12, the diesel consumption of the 8th system is 1227L less than that of the 1st system, and the renewable fraction of the 8th system is 11% more than the 1st system. However, the excessive electricity of 8th system is 2546kWh more than the 1st system. This excessive energy should be fully decreased, due to its thermal damage to the devices. Besides, the additional wind turbine increases system initial capital and maintenance fees. Therefore, the 1st system is chosen because of better economics and less excess electricity than the 8th system. According to figure 2.14, the payback time of the system is 25 years, and its annual operation cost is 10187 CAD. This system, therefore, could be affordable for the users in this area in the future.

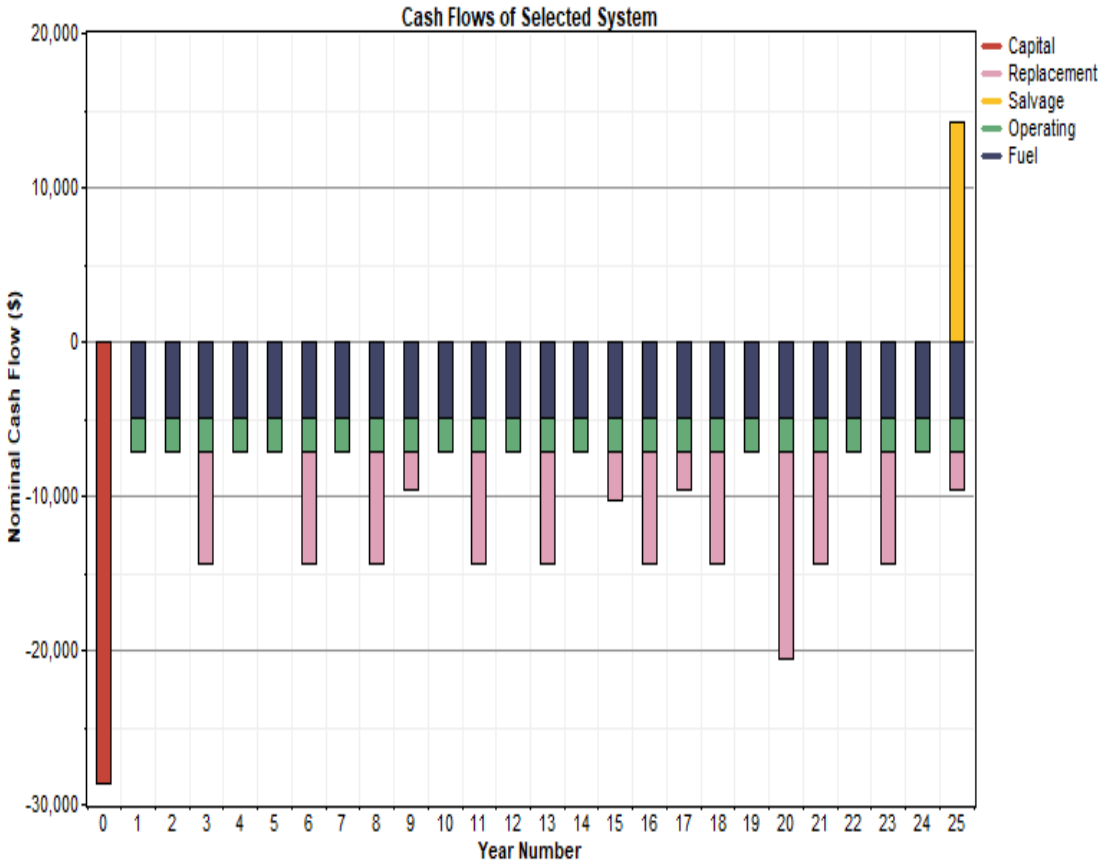


Figure 2.14 Cash Flow of Selected System Design

### 2.4.3 Details of Selected System

In the selected system the DC electricity generated by the PV array and DC generator charges the battery storage and then supplies the AC load through the DC to AC inverter. The detailed description of each component is shown below.

#### 2.4.3.1 PV Array

The PV array consists of 22 strings connected in parallel. Each string consists of 2 PV modules connected in series. The detailed parameters of each PV module are shown in table 2.2 below.

| Parameter | Value |
|---|---|
| Model Number | CHSM6612P 310Wp |
| Rated Output Power at STC | 0.31 kW |
| Short-Circuit Current ($I_{sc}$) | 8.99 A |
| Open-Circuit Voltage ($V_{OC}$) | 45.42 V |
| Output Voltage at Maximum Power | 35.8 V |
| Output Current at Maximum Power | 8.68 A |
| Rated Efficiency at STC | 16 % |
| Temperature Coefficient of $I_{SC}$ | -0.311 %/℃ |
| Temperature Coefficient of $V_{OC}$ | 0.050%/℃ |
| Number of Modules | 44 |
| Azimuth | 0° |
| Price | 306 CAD |

Table 2.2 Detailed Parameters of Single PV Module

The rated output voltage of the PV array is 72V, which effectively charges the 48V battery storage. The rated output power of the PV array is 13.64kW. The slope angle of the PV array is 37.833° (latitude of the location) for maximum solar radiation.

2.4.3.2 DC Diesel Generator

The detailed parameters of DC diesel generator are listed in table 2.3 below.

| Parameter | Value |
|---|---|
| Model Number | PDC-8080VP-20 |
| Rated Output Power | 8 kW |
| Output Voltage | 24~144 V |
| Engine RPM | 2900 rpm @ 8kW |
| Efficiency | 94% |
| Price | 2400 CAD |

Table 2.3 Detailed Parameters of Diesel Generator

Similar to the PV array, the rated output voltage of the diesel generator is 1.5 times the nominal voltage of battery storage (shown in table 2.3) to charge the battery storage effectively.

#### 2.4.3.3 Battery Storage

The nominal voltage and capacity of the battery storage are 48V and 1000Ah respectively. The battery storage consists of five strings of batteries. Each string consists of four batteries connected in series. The detailed data of a single battery is shown in table 2.4 below.

| Parameter | Value |
|---|---|
| Nominal Capacity | 200 Ah |
| Nominal Voltage | 12 V |
| Round Trip Efficiency | 80 % |
| Minimum State of Charge | 40 % |
| Maximum Charge Current | 60 A |
| Price | 400 CAD |

Table 2.4 Parameters of Single Battery

#### 2.4.3.4 Inverter

Because the peak load is 12.88kW, the rated capacity of the converter should be no less than 1.2 times of the peak load for enough redundancy. The detailed parameters of the inverter are shown in table 2.5 below.

| Parameter | Value |
|---|---|
| Model Number | GW Plus 10K |
| Input DC Voltage | 40~60 VDC |
| Output AC Voltage | 220 VAC |
| Output Frequency | 50/60 Hz |
| Rated Output Power | 15 kW |
| Rated Output Current | 68 A |
| Out Type | Single Phase |
| Wave | Pure Sine Wave |
| Efficiency | ≥ 93% |
| Waveform Distortion (Linear Load) | ≤ 3% |
| Power Factor | 0.8 |
| Price | 1068 CAD |

Table 2.5 Parameters of DC/AC inverter

2.4.3.5 Accessories

The details of other accessories in the hybrid power system are shown in table 2.6 below.

| Component | Model Name | Price |
|---|---|---|
| Battery Chest Box | Sunwize Enclosure 2*8D Batteries | 1174.5 CAD × 1 |
| AC Lightning Arrestor | Delta LA301 | 40.732 CAD × 1 |
| DC Lighting Arrestor | Delta LA302DC | 54.4 CAD × 1 |
| Grounding and Wiring Accessories | GENSR-2HOLES-LN | 4.66 CAD/piece × 50 |
| Battery Connect Cables | 2/0 13"BC-BLK | 22.08 CAD/inch × 300 |
| DC Circuit Breaker | NMCB07 | 74.8 CAD/piece × 1 |

Table 2.6 Details of Accessories

## 2.5 Conclusion

Because of the fast development of renewable energy in China and abundant renewable resource in the selected area, the hybrid power system including renewable and traditional power is a viable alternative. Because net metering is not allowed, only the isolated hybrid power system is considered. To achieve an available and economic system design, the system sizing is done in HOMER. Before that, the weather, components specification and annual hourly load data are required. Compared to the weather and components specification data, annual hourly load data is generated in BEopt by inputting collected weather data and building architecture. Finally, an affordable isolated hybrid power system including both solar and diesel power is designed. This means that the isolated hybrid power system is both economical and reliable for the residence in this area.

# Chapter 3

# Dynamic Modeling and Simulation of Hybrid Power System

## 3.1 Introduction

In chapter 2 HOMER is used to design system sketch, check hourly energy balance and size system component based on the provided data of the load, weather, and component. The transient system stability under the short-time disturbances in weather and load is checked by dynamic simulation in Simulink. For system simplification, the hybrid power system is switched to a DC coupled system, in which the diesel generator is a DC diesel generator. For system stability, the designed controllers include the Maximum Power Point Tracking (MPPT) for the PV array, the soft starter for the diesel generator, the charge controller for the battery storage and the PI controller for the single-phase inverter. To increase the quality of the input and output voltage of the single-phase inverter, a boost converter controlled by PID voltage controller is added between the battery and inverter. The inverter's controller is upgraded to PID + R + CCF controller. To further improve the performance of inverter, a time-delayed controller for the boost converter is designed for comparison. The detailed description of this chapter is shown below.

## 3.2 Dynamic Model of Hybrid Power System

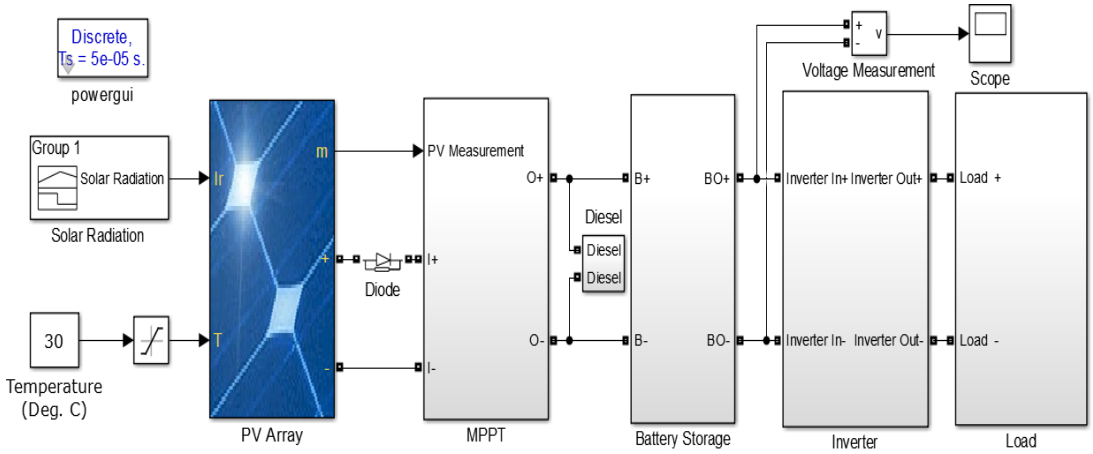


Figure 3.1. Simulink Model of Hybrid Power System

In the hybrid power system shown in figure 3.1, the PV array generates power according to the received solar radiation. The blocking diode at the output of the PV array prevents the PV array being charged during zero solar radiation. The MPPT adjusts the output voltage of the PV array to achieve its maximum power output. The DC diesel generator is a backup power supply when the power generated by the PV array is less than the load power. All the generated power charges the battery storage and supplies the load through the single-phase inverter, which transforms the DC to AC. The system is simulated in discrete mode. Each component is discussed below.

### 3.2.1 PV Array

For efficient simulation, the model of the PV array (shown in figure 3.1) is from [13]. The detailed mathematic equations of the model are listed below [13]:

$$I_d = I_o\left[\exp\left(\frac{V_{diode}}{V_T}\right) - 1\right] \quad (3.1)$$

$$V_T = \frac{kT}{q} \times nI \times Ncell \quad (3.2)$$

$$V_{OCT} = V_{OC}\left(1 + \beta_{Voc}(T - 25)\right) \quad (3.3)$$

$$I_{SCT} = I_{SC}\left(1 + \alpha_{Isc}(T - 25)\right) \quad (3.4)$$

$$V_{diode} = V_{PV} + R_{s\_array} I_{PV} \quad (3.5)$$

$$I_{PV} = I_L - I_d - \frac{V_{diode}}{R_{sh_{array}}} \quad (3.6)$$

Where $I_d$ is the diode current of a solar cell, $I_o$ is the diode saturation current of a solar cell, $V_{OCT}$ is the open-circuit voltage of a solar cell, $V_{OC}$ is the open-circuit voltage of a solar cell, $V_{diode}$ is the diode voltage of the PV array, $V_{PV}$ is the real output voltage of the PV array, $V_T$ is the temperature factor of $I_d$, $I_{PV}$ is the output current of the PV array, $R_{sh_{array}}$ is the shunt resistance of the PV array, $R_{s\_array}$ is the series resistance of the PV array, $I_{SC}$ is the short-circuit current of a solar cell, $I_{SCT}$ is the short-circuit current of a solar cell at temperature $T$ which is the operating temperature of a solar cell, $I$ is diode ideality factor, $\beta_{Voc}$ is the temperature coefficient of $V_{OC}$, $\alpha_{Isc}$ is the temperature coefficient of $I_{SC}$, $N$ is the number of the solar cell per PV module, and $n$ is the number of PV module per string.

The PV array composes of 22 strings of PV modules connected in parallel. Each PV module consists of 72 solar cells in series. Each string consists of two modules in series. Other detailed parameters of a single PV module are shown in table 2.2.

### 3.2.2 Maximum Power Point Tracker (MPPT)

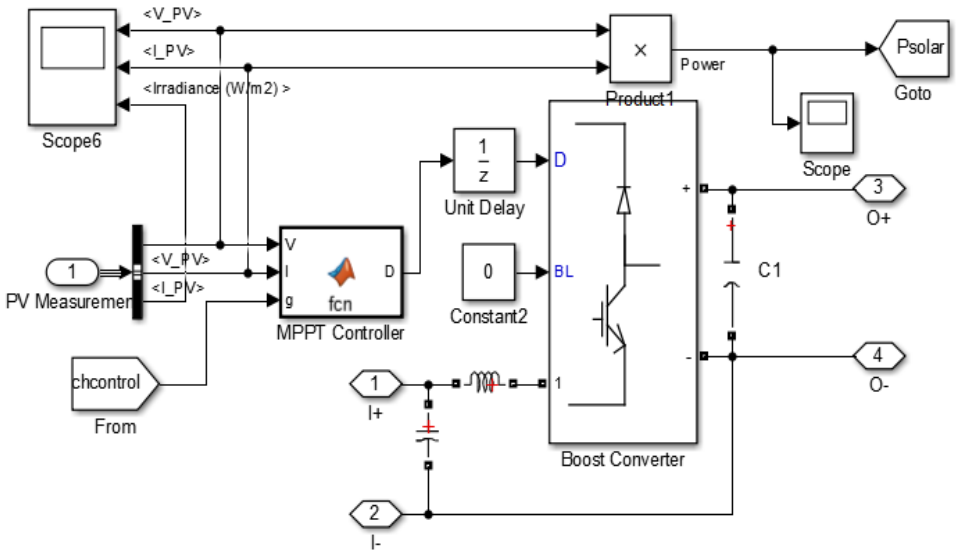


Figure 3.2 MPPT Model

It can be seen from figure 3.2 that the MPPT is a boost converter controlled by an MPPT controller. According to the MPPT controller's output signal, the boost converter changes the PV array's output voltage by changing its duty ratio to achieve its maximum power output. The capacitors at the input and output of the boost converter are used to filter the ripples of the input and output voltage of the boost converter. The inductor at the input of the boost converter stores the energy when the boost converter is switched on and also partially decreases the ripple of the input voltage. The capacitors and inductors above are calculated below [43]:

$$L = \frac{V_{in}(V_{out}-V_{in})}{\Delta I_l f_s V_{out}} \tag{3.7}$$

$$\Delta I_l = \frac{(0.2\sim0.4) f_s V_{out}}{V_{in}} \tag{3.8}$$

$$\Delta V_{PVmppt} = 0.05 V_{mppt} \tag{3.9}$$

$$\Delta V_{PVmppt} = \frac{P_{mppt}}{2 f_g C_{dc} V_{mppt}} \tag{3.10}$$

Where $V_{in}$ is the typical input voltage, $V_{out}$ is the typical output voltage, $f_s$ is the minimum switching frequency of the converter, $\Delta I_l$ is the estimated inductor ripple current, $f_g$ is the carrier frequency of the inverter, $C_{dc}$ is the capacitor at the output of the converter, $P_{mppt}$ is the maximum power of the converter, $V_{mppt}$ is the output voltage of the boost converter during its maximum power output. Please notice that the calculated values of the capacitors and inductor are not final values, since they need to be adjusted for better performance during the simulation.

The measured PV output power is used to monitor the PV array and decide whether to start or shutdown the diesel generator. The MPPT controller is not only to extract the maximum output power of the PV array but also prevent the battery from over discharging and overcharging. The input signals of the MPPT include the output voltage and current of the PV array and control signal from the battery charge controller. The flow chart of the MPPT algorithm is shown in figure 3.3 below.

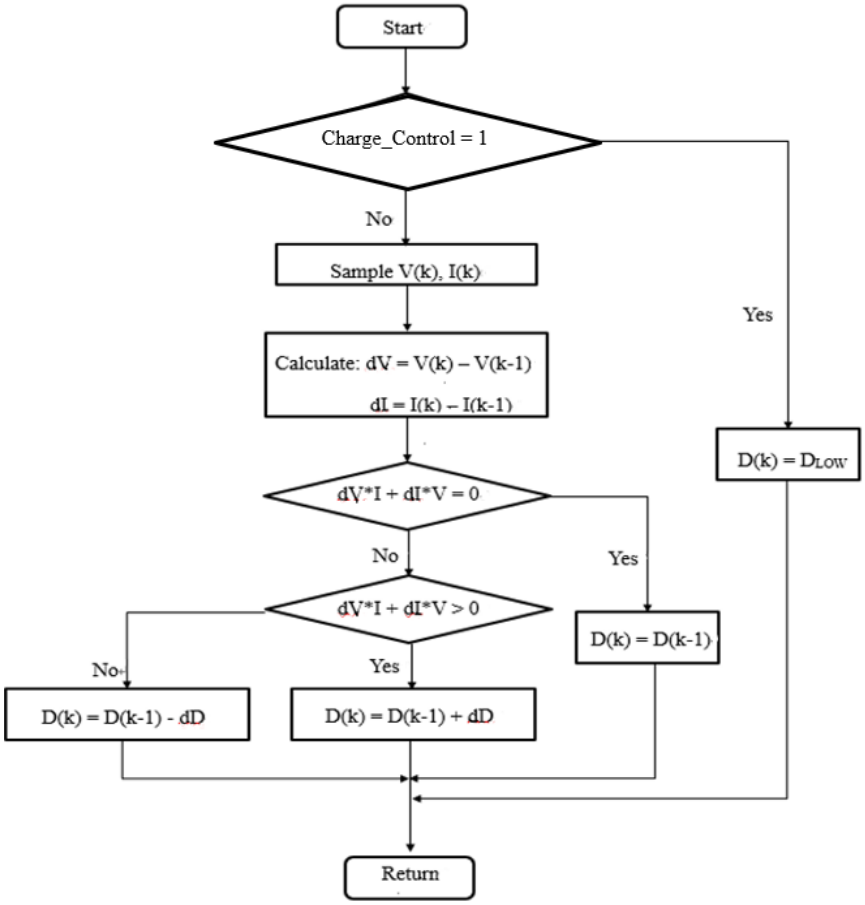


Figure 3.3. Flow Chart of Simplified Incremental Conductance Method

The MPPT algorithm in figure 3.3 is simplified incremental conductance method integrated with battery charge control. When the charge control signal is off, the duty cycle depends on the value of $VdI + IdV$. If the value is positive, the duty cycle will be increased. If the value is negative, the duty cycle will be decreased. If the value is zero, the duty cycle remains unchanged. When the charge control signal is effective, the duty cycle will be switched to a value corresponding to minimum PV output.

### 3.2.3 Diesel Generator

When the output power of the PV array is less than the load, the diesel-generator controller switches on the diesel generator to supply the battery storage and load, to prevent the battery storage from over discharging. The soft starter of the diesel generator is designed to decrease the accumulated damage to the Insulated-gate bipolar transistor (IGBT). The detailed subsystem model of the diesel generator is shown in figure 3.4 below.

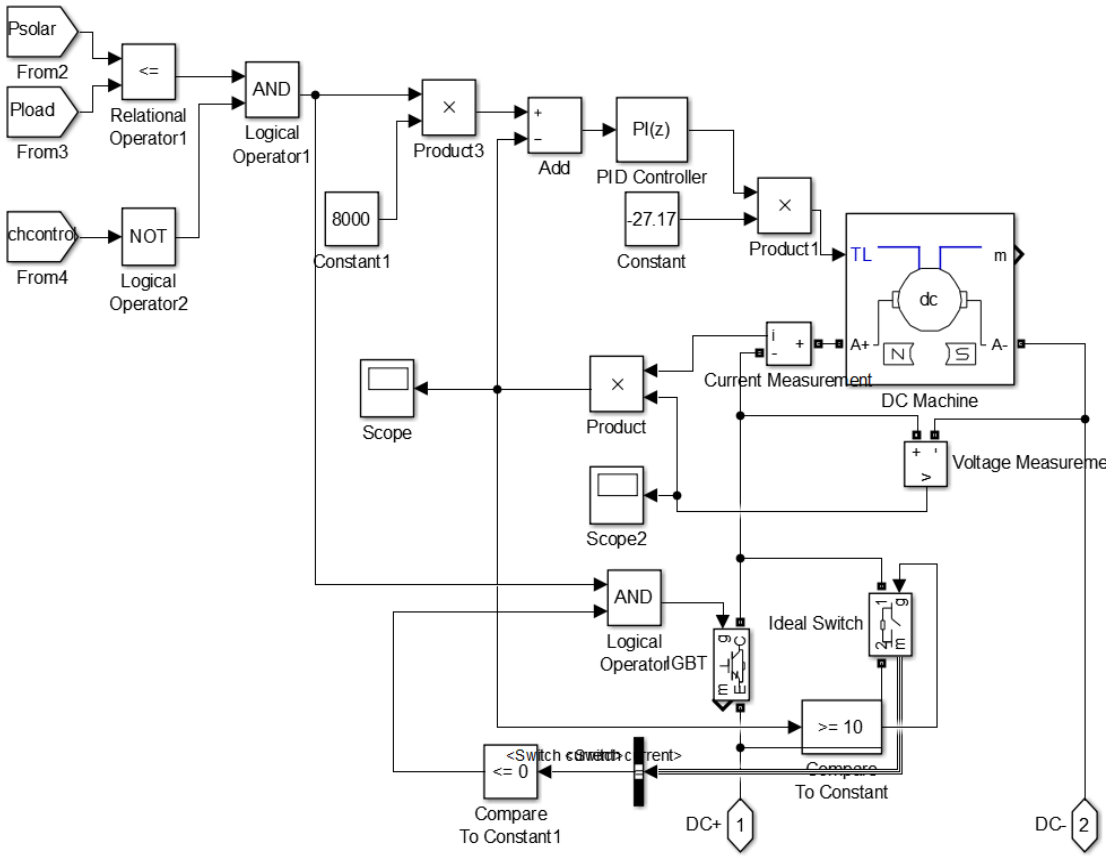


Figure 3.4 Diesel Generator Model

The commonly used diesel generator is an AC generator with a rectifier at the output. For less oscillation in the DC voltage of the system, a permanent magnet DC generator model from [13] is adopted in the simulation. Its mathematic equations are described below [13]:

$$\frac{di_a}{dt} = -\frac{r_a i_a}{L_{AA}} - \frac{k_v \omega_r}{L_{AA}} + \frac{v_a}{L_{AA}} \tag{3.11}$$

$$\frac{d\omega_r}{dt} = \frac{k_v i_a}{J} - \frac{B_m \omega_r}{J} - \frac{T_L}{J} \tag{3.12}$$

Where $i_a$ is the armature current (A), $r_a$ is the armature resistance (Ω), $\omega_r$ is the rotor angular speed (rad/s), $v_a$ is the armature voltage (V), $L_{AA}$ is the armature inductance, $J$ is the total inertia (kg.m^2), $T_L$ is the load torque, $B_m$ is the viscous friction coefficient (N.m.s), $k_v$ is the open-circuit voltage per rotational speed coefficient (V/rpm).

As it is shown in figure 3.4, the PI controller is activated, when the load power is larger than the PV output power, and the control signal of the charge controller is off. The control signal of the PI controller, which is proportional to the difference between the reference and measured power, multiplied with torque-power coefficient (N.m/kW) controls the torque of the diesel generator. The generator then reaches to its rated operation condition according to the torque control signal. Once the torque-control signal is active (the switch of the soft starter is still open), the IGBT keeps closed until the current increased to a certain positive value (0.2A). When the load power is below PV power or the charge-control signal is on, the torque control signal decreases the output power and stops the generator. During the process the IGBT keeps open, and the switch is turned off until the generator is completely stopped.

3.2.4 Battery Storage

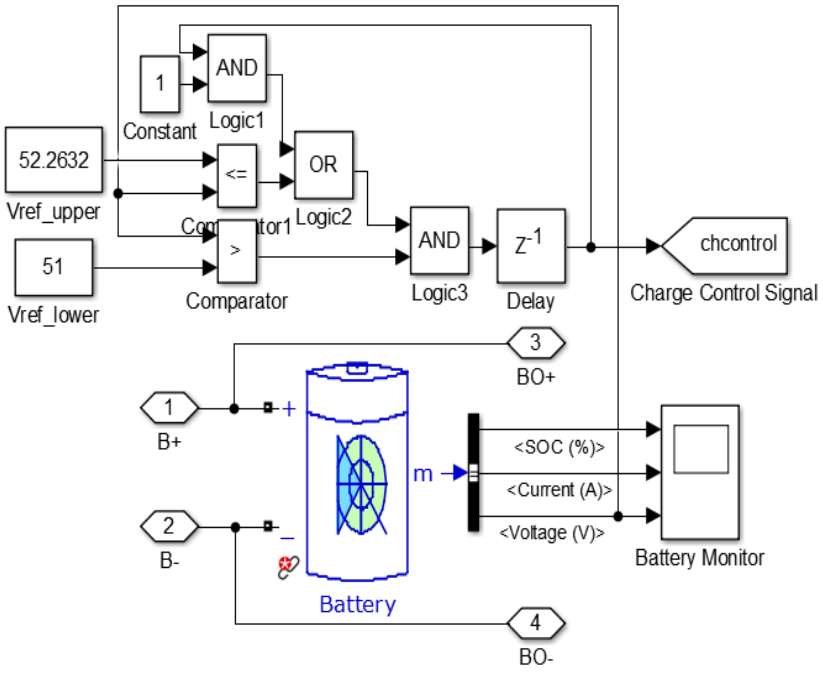


Figure 3.5 Battery Storage Model

The battery storage in figure 3.5 is lead-acid battery storage (48V nominal voltage and 1000Ah rated capacity). The diesel generator operates when the battery storage starts to discharge, and the battery model has the self-switch-off function when the SOC (state of charge) is below 50%. Therefore, in the charge controller, there is no function to prevent battery storage from over-discharging. The controller in figure 3.5 shows that once the battery voltage reaches the high reference value 52.2632V, the charge controller shuts down the diesel generator and switches the PV panel to its low power operation until the battery storage voltage reaches the lower reference value 51V. The mathematic equation of the battery storage model is listed below [13]:

$$E_{discharge} = E_0 - \frac{\mathrm{KQ}i^*}{\mathrm{Q}-i_t} - \frac{KQi_t}{Q-i_t} + Laplace^{-1}\left(\frac{A}{\frac{s}{Bi_t}+1} \cdot 0\right) \quad (3.13)$$

$$E_{charge} = E_0 - \frac{KQi^*}{i_t+0.1Q} - \frac{KQi_t}{Q-i_t} + Laplace^{-1}\left(\frac{A}{\frac{s}{Bi_t}+1} \cdot \frac{1}{s}\right) \quad (3.14)$$

Where $E_0$ is constant voltage (V), $Q$ is maximum battery capacity (Ah), K is polarization constant, $i_t$ is extracted capacity (Ah), $A$ is exponential voltage (V), $B$ is exponential capacity $(\mathrm{Ah})^{-1}$, $i^*$ is low frequency current dynamics (A).

3.2.5 Single Phase Inverter

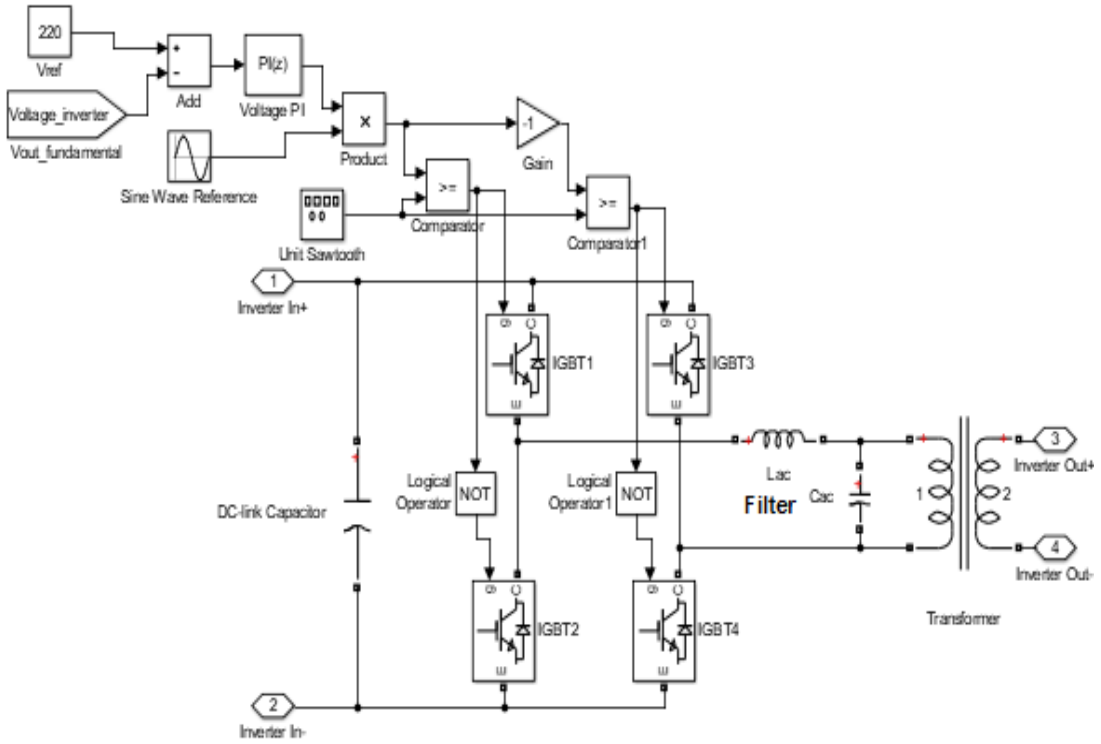


Figure 3.6 Single-Phase Inverter Model

Figure 3.6 shows that the inverter model consists of an input capacitor, four IGBTs, one LC filter, and one transformer. These IGBTs are controlled by unipolar modulation technique, which cancels the output harmonics with the carrier frequency [24]. To achieve steady inverter output, a closed-loop PI voltage control is used. The difference between the reference (220V) and measured fundamental voltage is sent to the PI. The multiplication and its negation of the PI output and reference sinewave (220V(RMS), 50Hz) compared with the same sawtooth carrier (15000Hz) become the modulated signals for the left and right arm of the inverter.

The LC filter filters other harmonics of the inverter output voltage. Its output voltage (34V (RMS)) is then boosted up to the application level (220V(RMS)) by the transformer. The inductance and capacitance of the filter are calculated below [44]:

$$L_{ac} = \frac{V_{dc}}{8\Delta I_{ripple.max} f_{sw}} \tag{3.15}$$

$$C_{ac} = \frac{\alpha P_{rated}}{2\pi f_{line} {V_{rate}}^2} \tag{3.16}$$

Where $\Delta I_{ripple.max}$ is 20% of the rated current, $f_{sw}$ is twice the carrier's frequency, $\alpha$ is the reactive power factor, which is less than 5%.

### 3.2.6 Load Model

The maximum load power is 12.88kW, corresponding to a 3.76Ω load resistance, and the average load power (2810W) corresponds to a 7.56Ω load resistance. The phase-locked loop model from [13] measures the fundamental current and voltage of the load. Their production (load power) is the input of the charge controller and diesel controller. The detailed model is shown below.

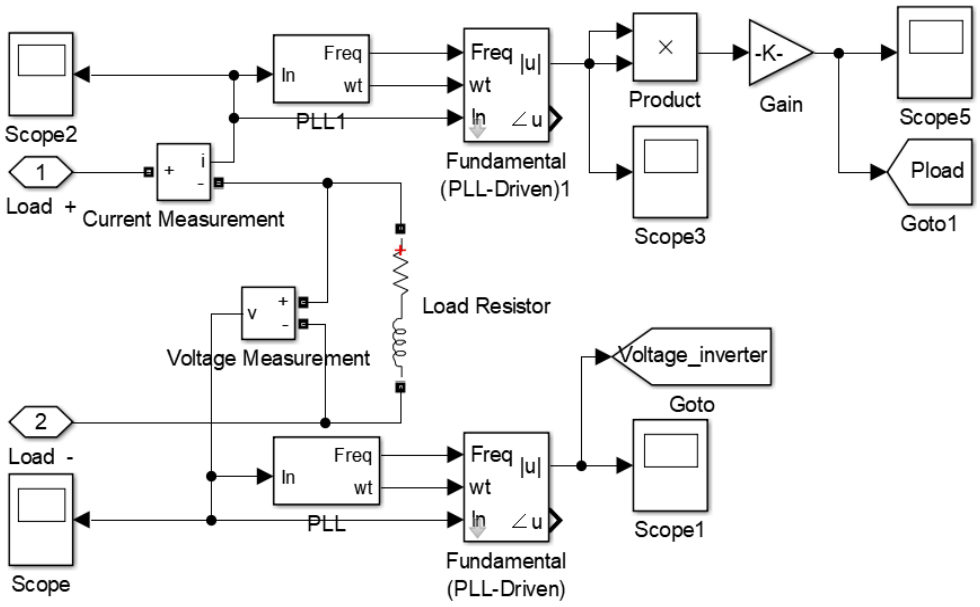


Figure 3.7 Load Model

## 3.3 Simulation Results

The dynamic system model is simulated in the following three situations to check the transient stability and functions of the system under different system operations.

### 3.3.1 Maximum Load, Dip in Solar Radiation and 50% Battery SOC

This case is to check whether the system can steadily supply the maximum load (12.88kW) when the cloud shadow passes by the PV array. The solar radiation in figure 3.8 drops from 1000W/m$^2$ to 500W/m$^2$ and rises back to 1000W/m$^2$ (25s ~ 40s).

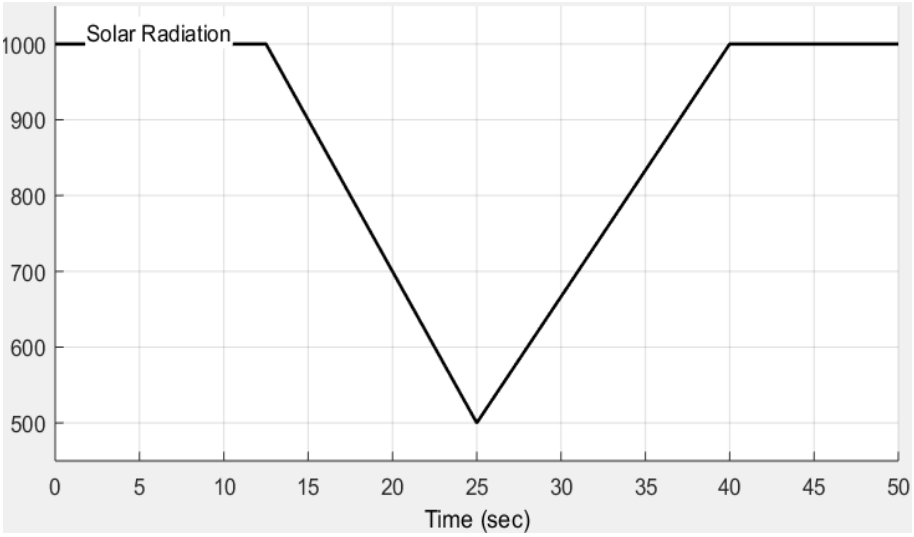


Figure 3.8 Solar Radiation - 1st Case

The power output from the PV array changes in the same manner as the solar irradiance, which is shown in figure 3.9 below.

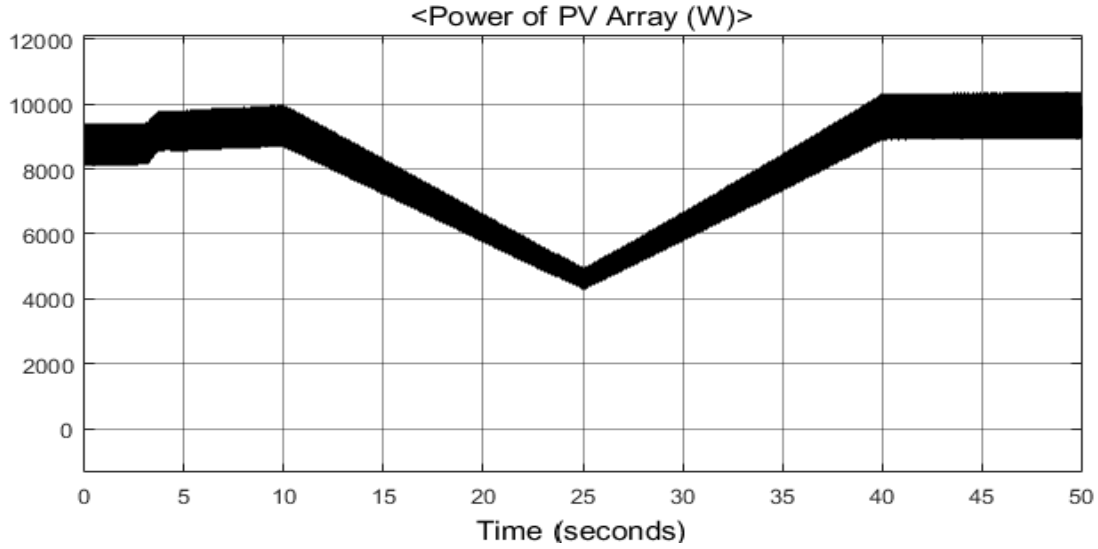


Figure 3.9 Output Power of PV Array – 1st Case

Figure 3.9 shows that the maximum output power of the PV array is 9500W, which is 69% of the rated power output of the PV array. This is because the output voltage of the PV array is firmly controlled by battery storage (1000Ah capacity). Because the PV output power is lower than the maximum load power, the diesel generator keeps operating during the simulation. The inertia of the diesel generator leads to 3s' delay for its initiation and 2s' delay for its steady-state operation (figure 3.10).

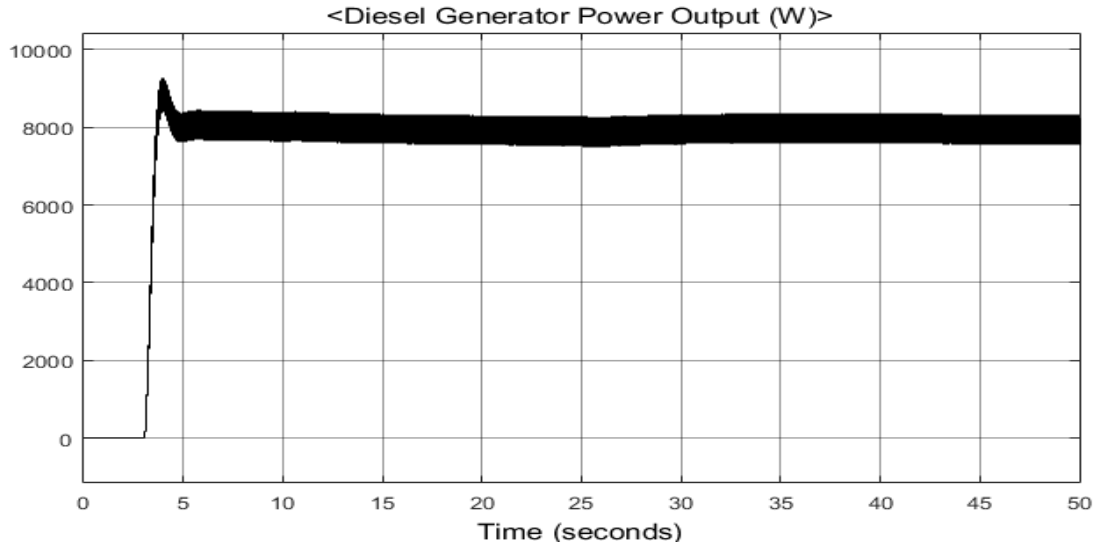


Figure 3.10 Output Power of Diesel Generator – 1st Case

Figure 3.11 shows that during the first 3s when the diesel generator is not fully started, the power from the PV array is not enough to supply the load. The battery voltage therefore decreases. After 3s when the diesel generator is fully started, the total input power is larger than the load. This results in continuous battery charging, and the battery voltage keeps increasing until the end of the simulation.

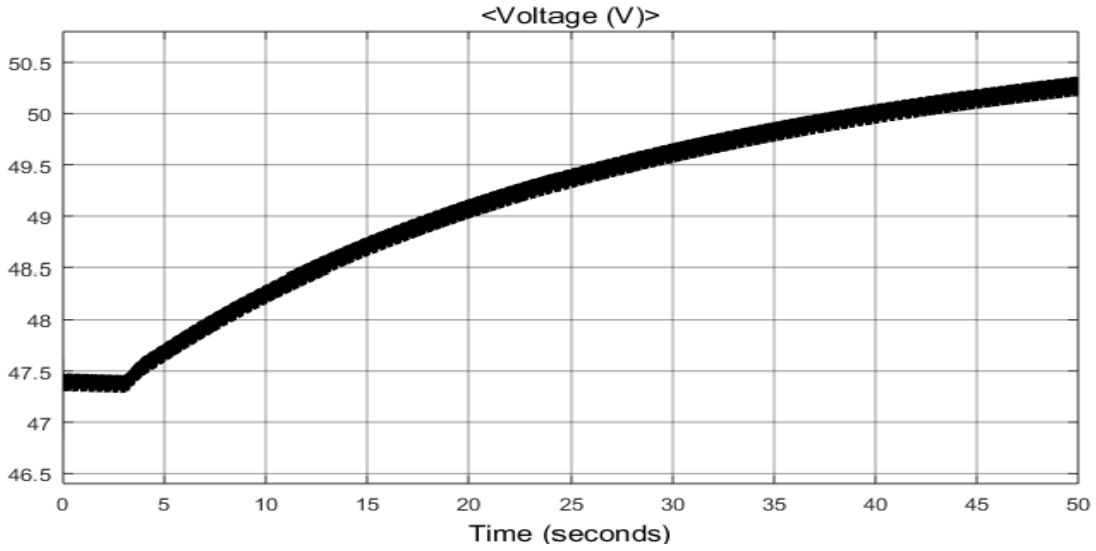


Figure 3.11 Voltage of Battery Storage – 1st Case

The magnitude of the inverter output voltage also changes along with the battery voltage (figure 3.12), because of no voltage stabilization for the inverter's input voltage. If the stabilization exists, the value should be around +/- 311V.

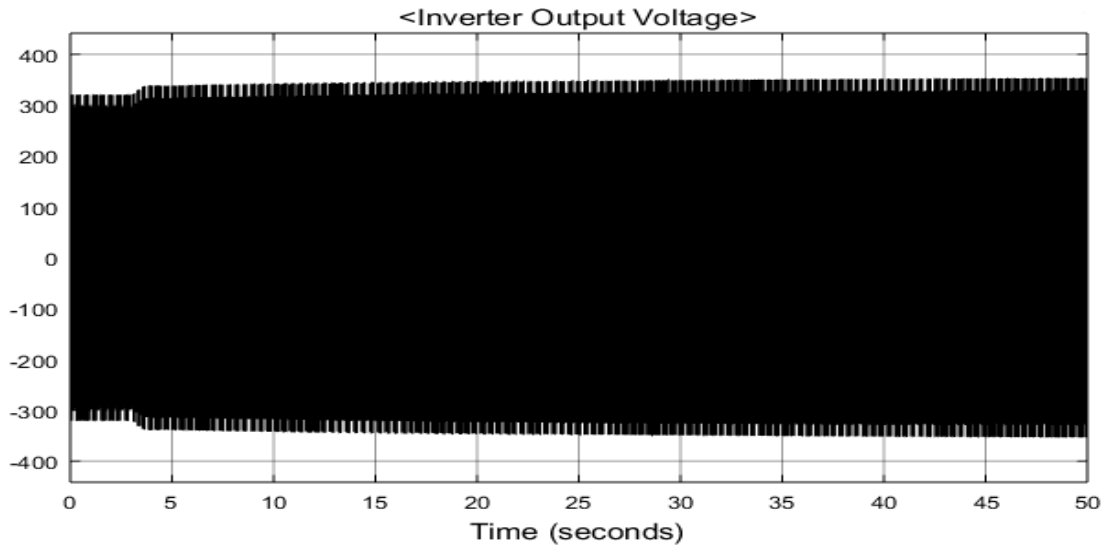


Figure 3.12 Output Voltage of Inverter – 1st Case

### 3.3.2 Average Load, Increasing Solar Radiation and 50% Battery SOC

This case is to check whether the diesel generator can be switched on and off when the power generated by the PV array is below and above the load power respectively. The simulation results are listed below.

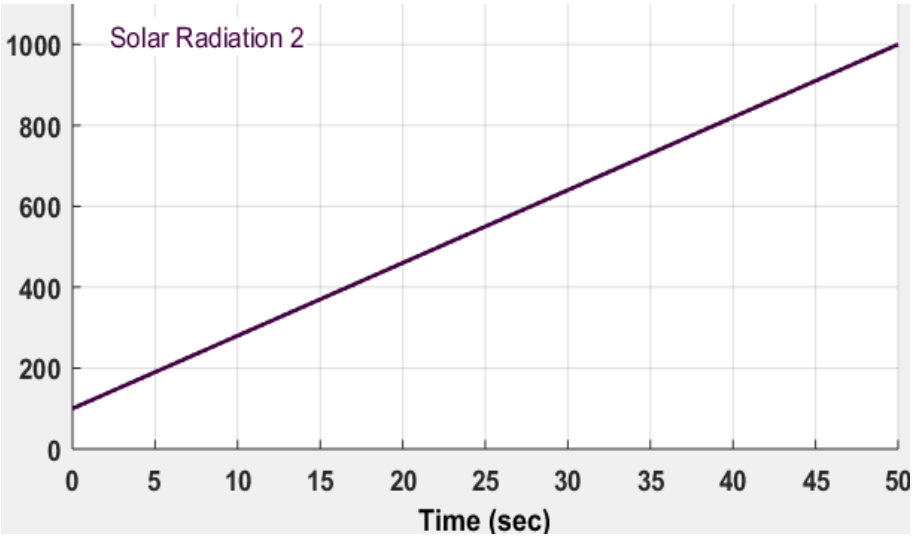


Figure 3.13 Solar Radiation – 2nd Case

As it is shown in figure 3.13, in this case, the solar radiation increases from 100W/$m^2$ to 1000W/$m^2$ at the end. Accordingly, the output power of the PV array changes in the same manner (shown in figure 3.14).

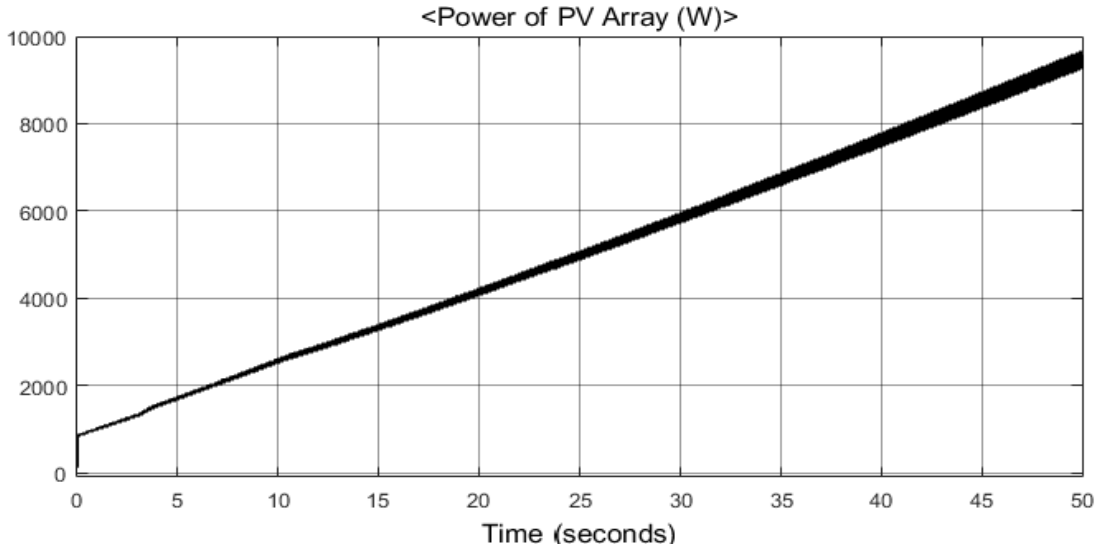

Figure 3.14 Output Power of PV Array – 2nd Case

Figure 3.14 shows that the output power of the PV array is below the load power before 10s. Thus, the diesel generator is switched on and off before and after that time. It takes about 19 seconds to shut down the generator because of its inertia, which also results in the 3s' delay for the initiation of the diesel generator (figure 3.15).

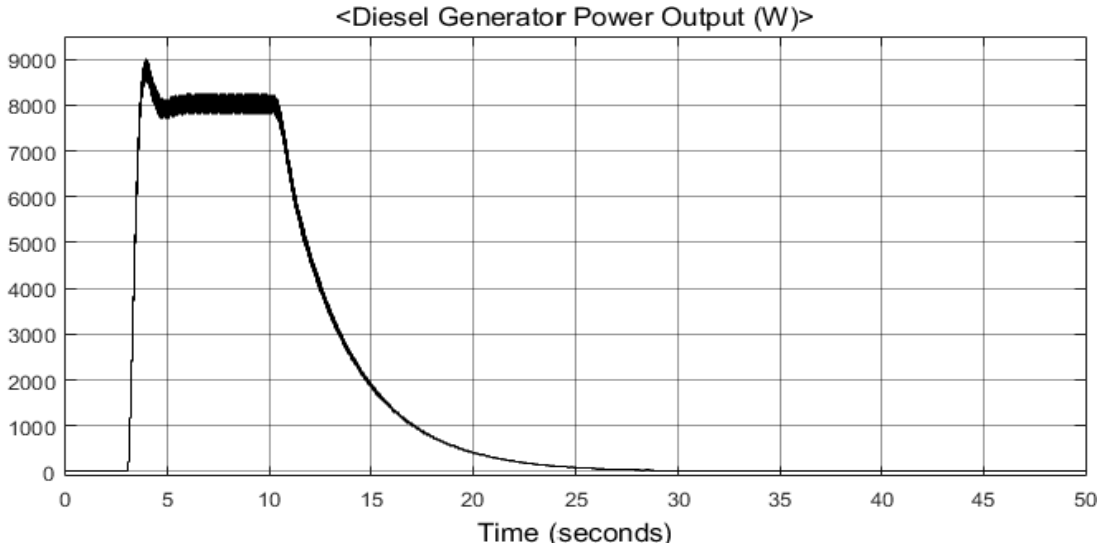

Figure 3.15 Output Power of Diesel Generator – 2nd Case

Figure 3.16 below shows that in the first 3s the battery voltage stays almost constant because of the much lower load power. After 3s when the diesel generator is fully started, due to the much larger input power (power from both PV array and diesel generator), the battery voltage increases very fast. After 10th second when the output power of the diesel generator starts to decrease, the increasing speed of the battery

voltage slows down. When the diesel generator is switched off at the 30s, the power generated by the PV array (about 5900W) becomes higher than the load (2810W), so the battery voltage keeps increasing until the end of the simulation.

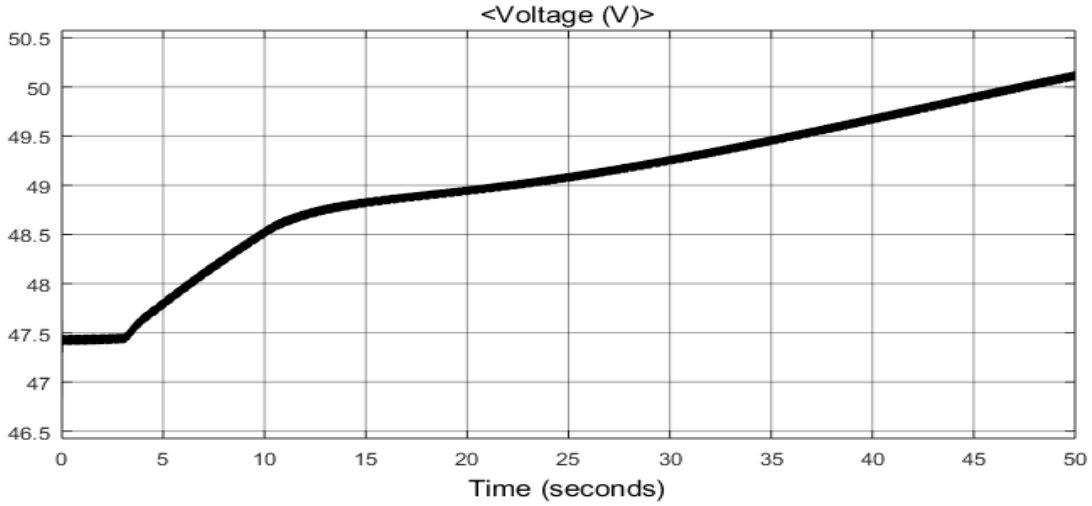


Figure 3.16 Voltage of Battery Storage – 2nd Case

The increasing DC voltage also affects the waveform of the output AC voltage of the inverter (shown in 3.17), in which the peak value of the inverter's output voltage changes in the same manner as the battery-storage voltage in figure 3.16.

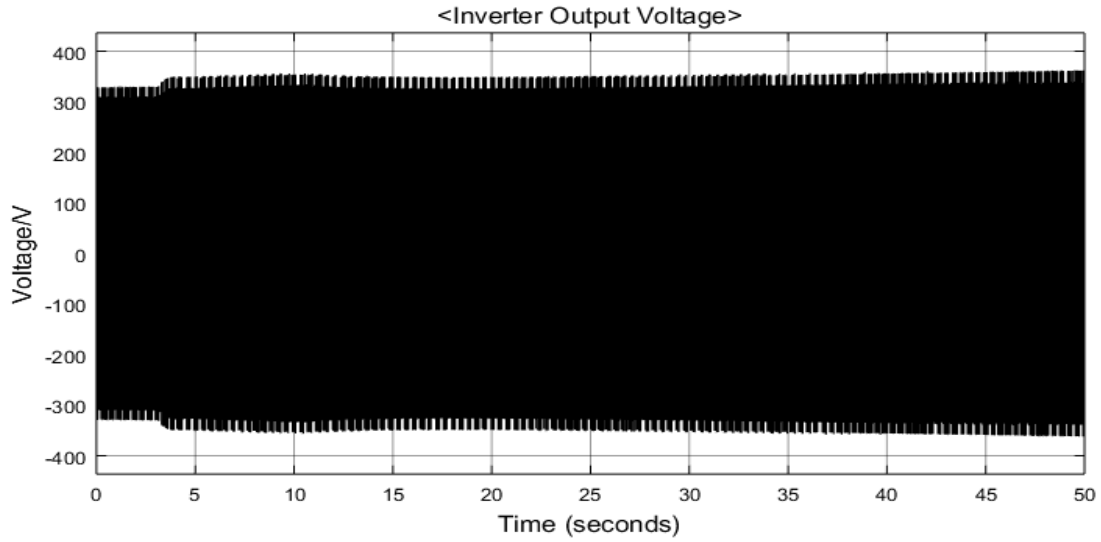


Figure 3.17 Output Voltage of Inverter – 2nd Case

### 3.3.3 Maximum Solar Radiation, Average Load and 99.3% Battery SOC

This case is to check the charge controller of the battery storage whether it can work properly when the battery is fully charged. In this case, the solar radiation keeps its maximum value (1000W) during the whole simulation, which results in maximum

power output of the PV array (figure 3.18).

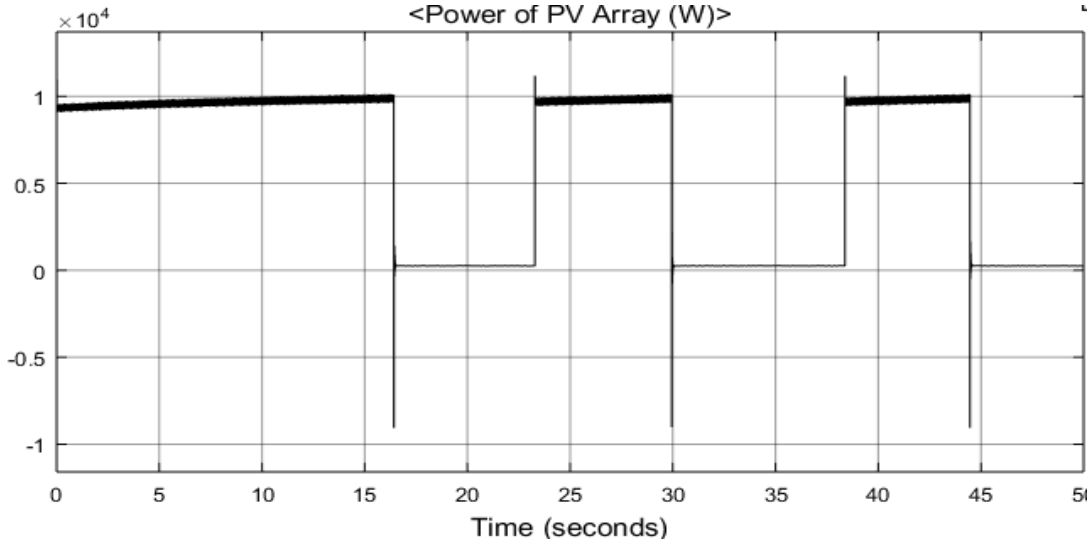


Figure 3.18 Output Power of PV Array – 3rd Case

Figure 3.18 shows that the PV array transits from its maximum power operation (9100W) to lowest power operation (250W) at 16.45s, 29.31s and 42.96s respectively when the battery storage gets fully charged. At the same time, the battery charge controller sends the charge-control signals to switch off the diesel generator (figure 3.19) and switch the PV array to its lowest operation (figure 3.20). Due to the decreased input power, the battery-storage voltage is discharged to its lower setting (51V) at 22.87s and 37.08s. The charge-control signal is then off, and the PV array returns to its maximum operation. During the maximum operation of the PV array, its maximum output power (> load power, 2810W) keeps shutting down the diesel generator (figure 3.19).

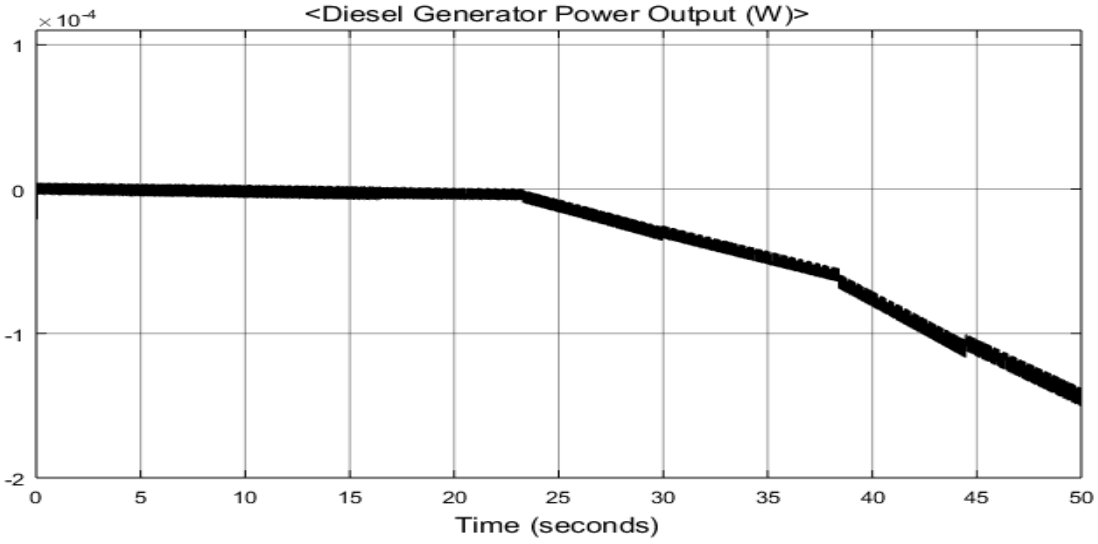


Figure 3.19 Output Power of Diesel Generator – 3rd Case

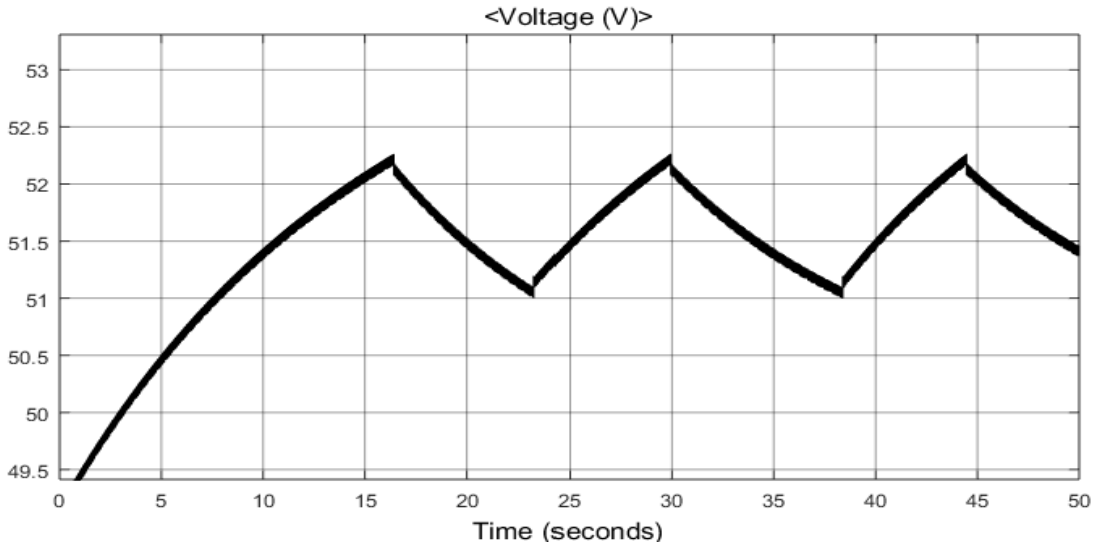


Figure 3.20 Voltage of Battery Storage – 3rd Case

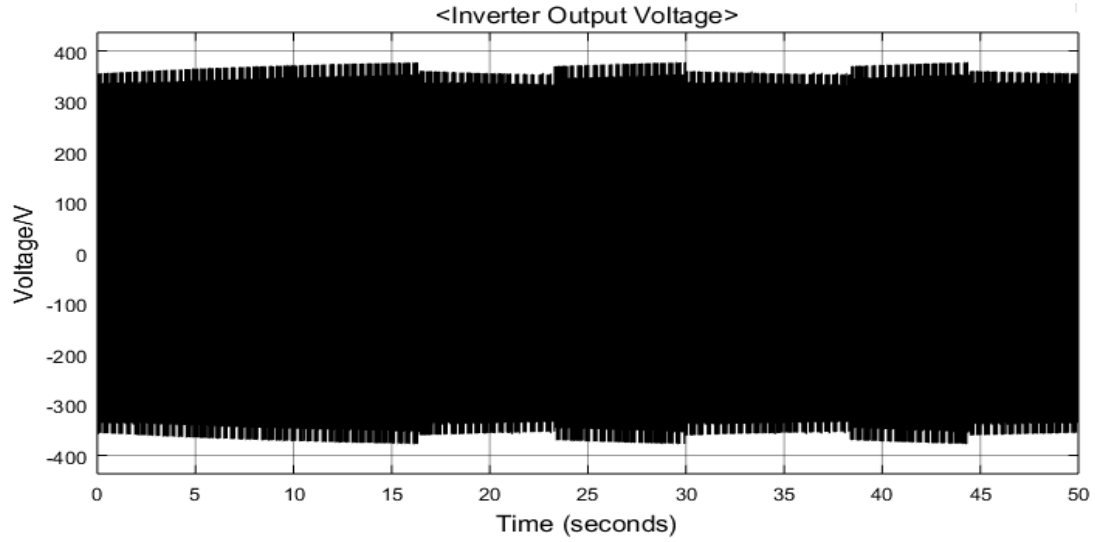


Figure 3.21 Output Voltage of Inverter – 3rd Case

Figure 3.21 shows that the increment and decrement of the battery-storage voltage change of the peak value of the inverter output voltage varying in the same manner as the battery-storage voltage.

It can be seen that different system operations change the battery-storage voltage and inverter output voltage, which results in an unstable power supply to the load. The inverter controller is designed to keep a constant RMS value of the fundamental output voltage of the inverter. The waveform of the inverter output voltage (shown in figure 3.22) is also severely distorted. Therefore, a DC input voltage regulator and a more advanced controller for the inverter are required, which is shown in section 3.4.

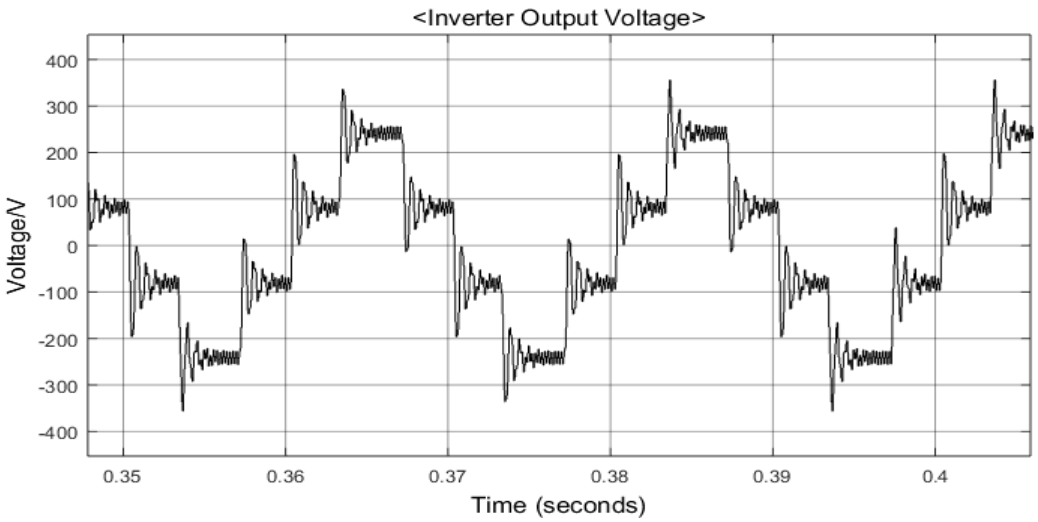


Figure 3.22 Distorted Waveform of Inverter Output Voltage

## 3.4 DC Voltage Regulator of Single-Phase Inverter

### 3.4.1 General System

According to the general structure of the system in figure 3.23, the input voltage stabilization is realized by a boost converter controlled by a time-delayed controller. The boost converter boosts up and stabilizes the DC input voltage of the inverter. The inverter, which is controlled by PID + R + CCF controller, then transforms the DC voltage to AC voltage for electrical applications.

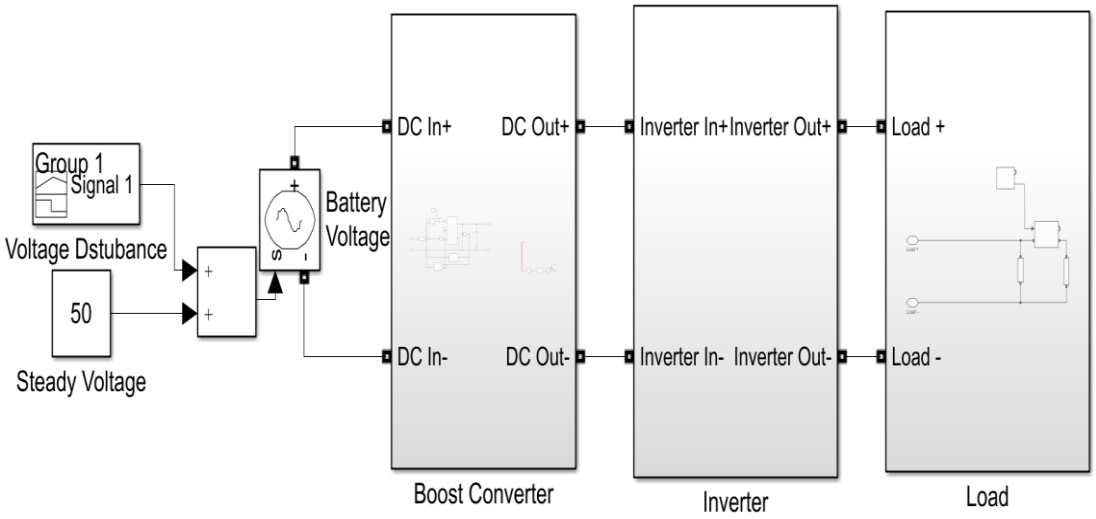


Figure 3.23 General System of DC Voltage Regulator

3.4.2 Controller Design of Single-Phase Inverter

As it is shown in figure 3.24, $V_{dc}$ is the DC input voltage of the inverter, $I_{dc}$ is the input current, $V_{AB}$ is the input voltage of the low pass filter, $I_{AB}$ is the input current of the lowpass filter, $R_{ac}$ is the load resistance, $Z_{ac}$ is the load resistance observed from the primary side of the transformer, $S_{AB}$ is the control signal of the inverter, $V_{ac}$ is the output voltage of the lowpass filter, $I_{ac}$ is the capacitor current.

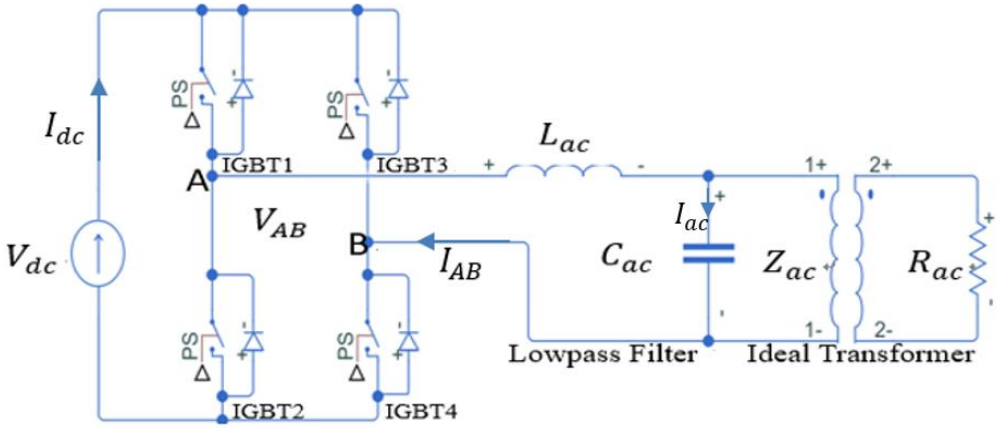


Figure 3.24 Schematic of Single-Phase Inverter

According to the mathematic model of the inverter shown in figure 3.25, the controller of the inverter consists of the series connection of the outer voltage controller (PID voltage controller (H_v) and resonance controller (R)) and the inner PID current controller (H_i). The resulted control signal is sent to the signal delay model (H_delay). The delayed control signal is then sent to the control to capacitor current plant (Gic). Its output signal is then both fed back to the inner current control loop through the lowpass filter (H_filter) and sent to the capacitor current to output voltage plant (Gvic). These transfer functions are listed below.

The control signal ($S_{AB}$) to capacitor current ($I_{ac}$) transfer function is shown in equation 3.17 below [45]:

$$G_{iC} = \frac{sC_{ac}Z_{ac}V_{dc}}{s^2L_{ac}C_{ac}+sL_{ac}+Z_{ac}} \quad (3.17)$$

The LC filter output voltage ($V_{ac}$) to its input current ($I_{ac}$) transfer function is shown in equation 3.18:

$$G_{viC} = \frac{1}{sC_{ac}} \tag{3.18}$$

The control signal delay model is shown in equation 3.19 below [45]:

$$H_{delay} = \frac{1-0.5T_{delay}s+(\frac{T_{delay}}{12})^2s^2}{1+0.5T_{delay}s+(\frac{T_{delay}}{12})^2s^2} \tag{3.19}$$

Where $T_{delay}$ is the time delay of the control signal, which is 1/72000s in this model. The transfer function of the filter is shown in equation 3.20 [13]:

$$H_{filter} = \frac{{\omega_0}^2}{1+2\zeta\omega_0+{\omega_0}^2} \tag{3.20}$$

Where $\omega_0$ is the natural frequency of the output voltage, which is $100\pi$, $\zeta$ is the damping ratio which is 1 in this model.

Since the electrical load for residential use is resistive, PID + R + CCF controller is enough [46]. The PID voltage controller (H_v) paralleled with the resonance controller (R) is to decrease the steady-state error of the inverter output voltage [46]. The reference signal for the outer voltage control is standard 50Hz sinewave, and its feedback is the measured inverter output voltage. The harmonics of the inverter output voltage can be therefore reflected to and attenuated by the outer voltage controller (H_v + R) and inner current controller (H_i). The complete mathematic model of the inverter, including its control system, is shown in figure 3.25 below.

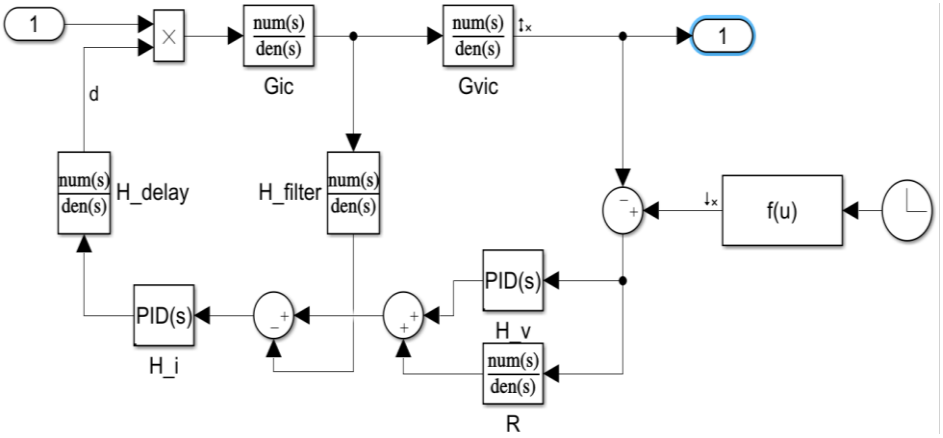


Figure 3.25 Mathematic Model of Single-Phase Inverter

The tuning and design of the control system are finished in controller design application in MATLAB, which largely saves the time for controller design. However, because of

the inaccurate mathematic model of the IGBT devices, there are some errors between the mathematic model and real-time model of the inverter. Thus, different performance appears in the mathematic and real-time simulation of the inverter by applying the same parameters in the controller. The controller thus needs to be tuned again in the real-time simulation.

### 3.4.3 Dynamic Model of Boost Converter

#### 3.4.3.1 Parameters of Boost Converter

To minimize the voltage ripple of the boost converter and increase the stability of the converter, the parameters of the boost converter are calculated below [47]:

$$V_{o\_ripple\_ESR} = I_{in} \cdot R_{ESR} \tag{3.21}$$

$$C_{min\_ripple} = \frac{I_{in}}{V_{o\_ripple\_C} \cdot f_{sw}} \left(1 - \frac{V_{in}}{V_o}\right) \tag{3.22}$$

$$R_{DCR\_max} = \frac{0.3 P_{total\_loss}}{{I_{in}}^2} \tag{3.23}$$

$$P_{total\_loss} = P_{total} \left(\frac{1}{\eta} - 1\right) \tag{3.24}$$

$$L_{\max} = C \cdot \left[R_{max} \cdot V_{in\_max}/(10 \cdot V_o)\right]^2 \tag{3.25}$$

Where $R_{ESR}$ is the equivalent series resistance of the capacitor, $I_{in}$ is the maximum input current, $V_{in}$ is the steady-state input voltage, $V_o$ is the steady-state output voltage, $V_{o\_ripple\_ESR}$ is the voltage ripple on $R_{ESR}$, $V_{o\_ripple\_C}$ is the predetermined voltage ripple of the capacitor- $C$, $C_{min\_ripple}$ is the minimum capacitor value, $f_{sw}$ is the switching frequency of the boost converter, $R_{DCR\_max}$ is the maximum direct-current resistance of the inductance, $\eta$ is the efficiency of the boost converter, $P_{total}$ is the maximum input power of the boost converter, $R_{max}$ is the maximum load resistance, $L_{\max}$ is the maximum inductance, $V_{in\_max}$ is the input voltage at the maximum load, $P_{total\_loss}$ is the power lost during the maximum load supply.

The resulted parameters are shown in table 3.1 below.

| Parameter | Value |
|---|---|
| Capacitance ($C$) | 3.57 (mF) |
| Inductance ($L$) | 3 (μH) |
| DCR ($R_{DCR}$) | 5.82 (mΩ) |
| ESR ($R_{ESR}$) | 0.776(mΩ) |
| Duty Ratio (Steady State) | 0.5 |
| $f_{sw}$ | 100(kHz) |
| $P_{total}$ | 12880(W) |
| $V_{in}$ (Steady State) | 50(V) |
| $V_o$ (Steady State) | 100(V) |
| $I_{in}$ (Steady State) | 257.6(A) |
| $R_{max}$ | 0.64(Ω) |

Table 3.1 Calculated Parameters of The Boost Converter

3.4.3.2 Mathematic Model of the Boost Converter

According to figure 3.26 below, the boost converter has two operations. One is IGBT-on operation, and the other is IGBT-off operation.

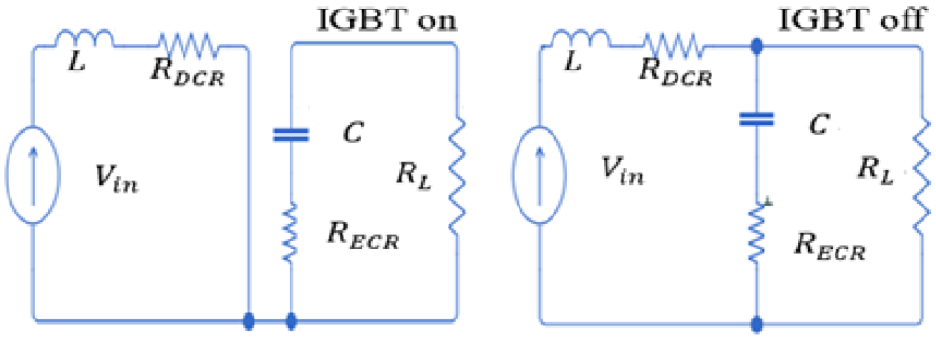


Figure 3.26 Equivalent Circuits of Boost Converter in On-Off Operation

Since the dynamics of these two operations are different, averaging these two dynamics is required [48]. The average model of the boost converter is listed below:

$$\begin{bmatrix}\dot{v}_C\\ \dot{i}_{in}\end{bmatrix}=\begin{bmatrix}\frac{1}{C(R_L+R_{ESR})} & -\frac{R_L}{C(R_L+R_{ESR})}\\ -\frac{R_L}{L(R_L+R_{ESR})} & -\frac{R_{DCR}}{L}-\frac{R_{ESR}R_L}{L(R_L+R_{ESR})}\end{bmatrix}\begin{bmatrix}v_C\\ i_{in}\end{bmatrix}+\begin{bmatrix}0 & \frac{R_L}{C(R_L+R_{ESR})}\\ \frac{R_L}{L(R_L+R_{ESR})} & \frac{R_{ESR}R_L}{L(R_L+R_{ESR})}\end{bmatrix}\begin{bmatrix}v_C\\ i_{in}\end{bmatrix}d+\begin{bmatrix}0\\ \frac{1}{L}\end{bmatrix}v_{in} \quad (3.26)$$

$$\begin{bmatrix} \dot{v_O} \\ \dot{i_{in}} \end{bmatrix} = \begin{bmatrix} \frac{R_L}{R_L+R_{ESR}} & \frac{R_L R_{ESR}(1-d)}{R_L+R_{ESR}} \\ 0 & 1 \end{bmatrix} \begin{bmatrix} v_C \\ i_{in} \end{bmatrix} \quad (3.27)$$

Where $v_C$, $i_{in}$, $v_{in}$, $v_O$, $d$ are the averaged capacitor voltage, input current, input voltage, output voltage and duty ratio respectively.

### 3.4.4 Time Delayed Control of Boost Converter

#### 3.4.4.1 Introduction of Time Delayed Control

Time delay control (TDC for abbreviation) is a robust control for nonlinear systems. Its control law is designed to minimize the error between the nonlinear system model and reference model. The mathematic equations of TDC are listed below [49]:

$$\dot{x}(t) = f(x,t) + d(x,t) + B(x,t)u(t) \quad (3.28)$$

$$\dot{x}_m(t) = A_m x_m(t) + B_m r(t) \quad (3.29)$$

$$e(t) = x(t) - x_m(t) \quad (3.30)$$

$$\dot{e}(t) = (A_m + K)e(t) \quad (3.31)$$

$$\hat{f}(x,t) = f(x,t) + d(x,t) + \left(B(x,t) - \hat{B}(x,t)\right)u(t) \quad (3.32)$$

$$u(t) = \left(\hat{B}^T\hat{B}\right)^{-1}\hat{B}^T(-\dot{x}(t-L) + \hat{B}u(t-L) + A_m x_m(t) + B_m r(t) - Ke(t)) \quad (3.33)$$

Where equation 3.28 is the state-space model of a designed system, equation 3.30 is the reference system model, equation 3.30 describes the error between state variables and references, equation 3.31 is the derivative of the system error (equation 3.30), equation 3.32 is the total effect of system uncertainty, equation 3.33 is the control law of the system, $d(x,t)$ is the system disturbance, $f(x,t)$ is the overall dynamic of the system, $r(t)$ is the command signal, $u(t)$ is the control input, $B(x,t)$ is the control input distribution, $\hat{B}(x,t)$ is the range of the control distribution, $x_m$ is reference state, $A_m$ and $B_m$ are reference matrixes, $L$ is time-delay constant, $K$ is the error feedback constant. The detailed derivation is shown in [49].

In the control law (equation 3.33), the total system uncertainty-$\hat{f}(x,t)$ is estimated by the delayed control input signal-$u(t-L)$ and the derivative of the delayed system state $\dot{x}(t-L)$. The domain of $\hat{B}(x,t)$ should be firstly calculated based on [10] to ensure

stability, and then tuned for an accurate system-uncertainty estimation and ideal system response.

### 3.4.4.2 Time Delayed Controller Design of Boost Converter

Since the voltage of $R_{ESR}$ is very small compared to the voltage of the capacitor, $V_o$ is approximately equal to $V_C$, which eliminates the observer design and simplifies the controller design. The detailed design process is shown below.

Instead of only using $-\dot{x}(t-L)$ and $\hat{B}u(t-L)$ to estimate system uncertainty (as shown in equation 3.33), a linear detectable dynamic $f^+(x,t)$ is included for the same purpose. Thus, the system uncertainty is shown in equation 3.34 below.

$$\hat{f}(x,t) = f(x,t) - f^+(x,t) + d(x,t) + \left(B(x,t) - \hat{B}(x,t)\right)u(t) \tag{3.34}$$

Due to the introduction of $f^+(x,t)$, the system state-space model shown in equation 3.28 becomes:

$$\dot{x}(t) = \hat{f}(x,t) + \hat{B}(x,t)u(t) + f^+(x,t) \tag{3.35}$$

Thus, based on equation 3.28, 3.29, 3.30, 3.31, 3.33, 3.34 and 3.35, the control law is described by equation 3.36 below.

$$u(t) = \left(\hat{B}^T\hat{B}\right)^{-1}\hat{B}^T(-\dot{x}(t-L) + \hat{B}u(t-L) + f^+(x,t-L) - f^+(x,t) + A_m x_m(t) + B_m r(t) - Ke(t)) \tag{3.36}$$

Based on the equations above, the TDC of the converter is shown below. Because of the changing load and current, only the voltage reference is utilized during the controller design. Thus, the average model of the output voltage (1st row of the equation 3.26) is used for the controller design. Accordingly, the reference model is designed to maintain the steady output voltage of the boost converter. The state space model and a reference model of the boost converter for the TDC design are shown in equation 3.37 and 3.38 below:

$$\dot{V}_o(t) = \frac{V_o(t)}{C(R_L+R_{ESR})} - \frac{R_L i_{in}(t)}{C(R_L+R_{ESR})} + \frac{R_L i_{in}(t)}{C(R_L+R_{ESR})}u(t) \tag{3.37}$$

$$\dot{V}_{ref} = -PV_{ref} + PV_o(t) \tag{3.38}$$

Where $u(t)$ is the control input, $\frac{V_o(t)}{C(R_L+R_{ESR})} - \frac{R_L i_{in}(t)}{C(R_L+R_{ESR})}$ is the overall system dynamics-$f(x,t)$, $\frac{R_L i_{in}(t)}{C(R_L+R_{ESR})}$ is the control signal distribution-$B(x,t)$, $V_{ref}$ is the reference of the output voltage, $V_o(t)$ is the state variable in equation 3.37 and order command signal in equation 3.38, $u(t)$ is the system control signal in equation 3.37, $-P$ and $P$ are the reference matrixes in equation 3.38.

Due to the changing load-$R_L$, the overall system dynamics-$f(x,t)$ becomes uncertain. Thus, the linear detectable dynamic-$f^+(x,t)$ is designed for its estimation. Since $R_{ESR}$ is very small, the uncertain dynamics-$\frac{R_L i_{in}(t)}{C(R_L+R_{ESR})}$ can be estimated by $\frac{i_{in}(t)}{C}$, and the uncertain dynamics-$\frac{V_o(t)}{C(R_L+R_{ESR})}$ can be estimated by $\frac{V_o(t)}{CR_{L.ra}}$. Since the dynamic of $R_L$ is unknown, the estimation of $\frac{V_o(t)}{C(R_L+R_{ESR})}$ is adjusted by tuning the parameter $R_{L.ra}$

Thus, the linear detectable dynamic $f^+(x,t)$ is shown in the equation below.

$$f^+(x,t) = -\frac{i_{in}(t)}{C} + \frac{V_o(t)}{CR_{L.ra}} + \frac{I_{the\,the\,ra}(t)}{C}u(t) \tag{3.39}$$

The control distribution range $\hat{B}$ is decided by equation 33 below.

$$\hat{B} = \frac{I_{ra}}{c} \tag{3.40}$$

Where $I_{ra}$ represents the range of the inductor current, which is equivalent to $\hat{B}$. $I_{ra}$ and $R_{L.ra}$ are the most frequently tuned parameters in this simulation. Their tuning process will be discussed in section 3.4.6.

Based on equations 3.34 to 3.40, the system uncertainty and control law is shown in equation 3.40 and 3.41 below.

$$\hat{f}(t) = \frac{V_o(t)}{C(R_L+r_C)} - \frac{V_o(t)}{CR_{L.ra}} + \frac{i_{in}(t)}{C} - \frac{R_L i_{in}(t)}{C(R_L+r_C)} + \frac{R_L i_{in}(t)}{C(R_L+r_C)}u(t) - \frac{I_{ra}}{\mathrm{C}}u(t) \tag{3.41}$$

$$u(t) = \frac{C}{I_{ra}}[\dot{V}_o(t) - \dot{V}_o(t-L) + \frac{V_o(t-L)}{CR_{L.ra}} - \frac{V_o(t)}{CR_{L.ra}} + \frac{i_{in}(t)}{C} - \frac{i_{in}(t-L)}{C} + \frac{I_{ra}}{C}u(t-L) + P(V_O - V_{ref})] \tag{3.42}$$

Based on equation 3.42, the TDC model for the converter in Simulink is designed in figure 3.27 below.

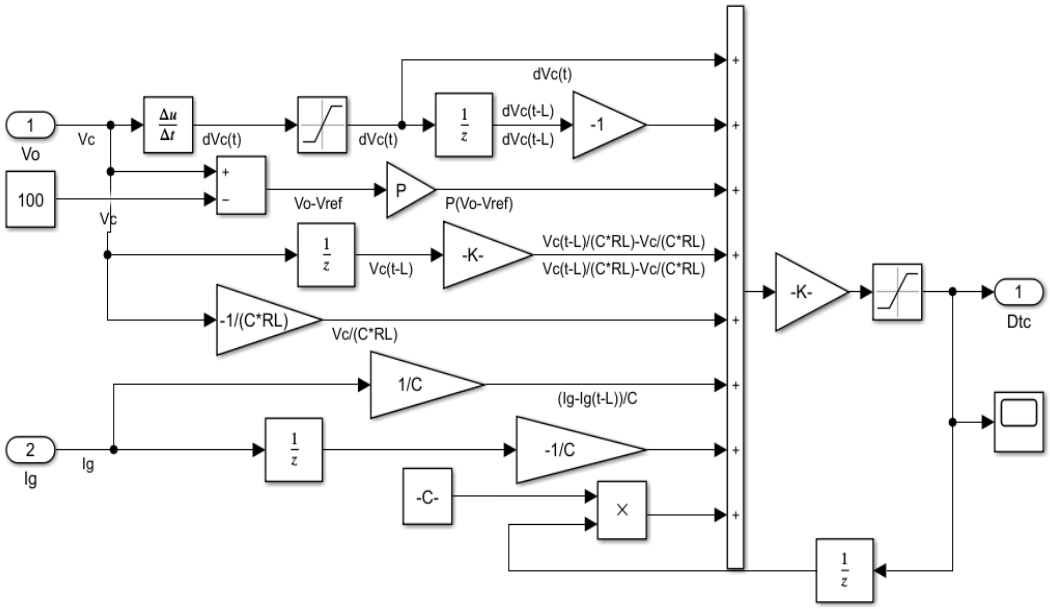


Figure 3.27 TDC Model of Boost Converter in Simulink

### 3.4.5 Simulations Result

To check the performance of the designed system and its controllers, the system is simulated under the five cases below.

#### 3.4.5.1 Maximum Load with Transient Voltage Disturbance

This case checks the performance of the converter-inverter system under the maximum load and the ∓10V input voltage disturbances (at 0.1s and 0.2s respectively). The output voltage of the boost converter under transient disturbance is shown in figure 3.28.

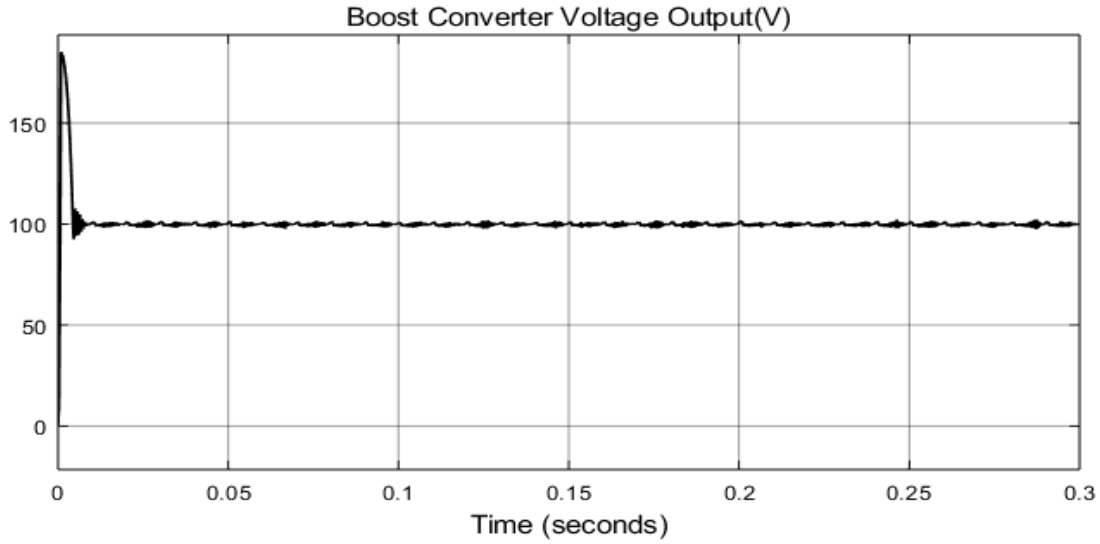


Figure 3.28 Converter Output (TDC) - 1st Case

Figure 3.28 shows that the output voltage of the converter oscillates from 98V to 102V. The effects of the input voltage disturbances at 0.1s and 0.2s are almost negligible. Thus, the waveform of the output voltage has less distortion, as it is shown in figure 3.29.

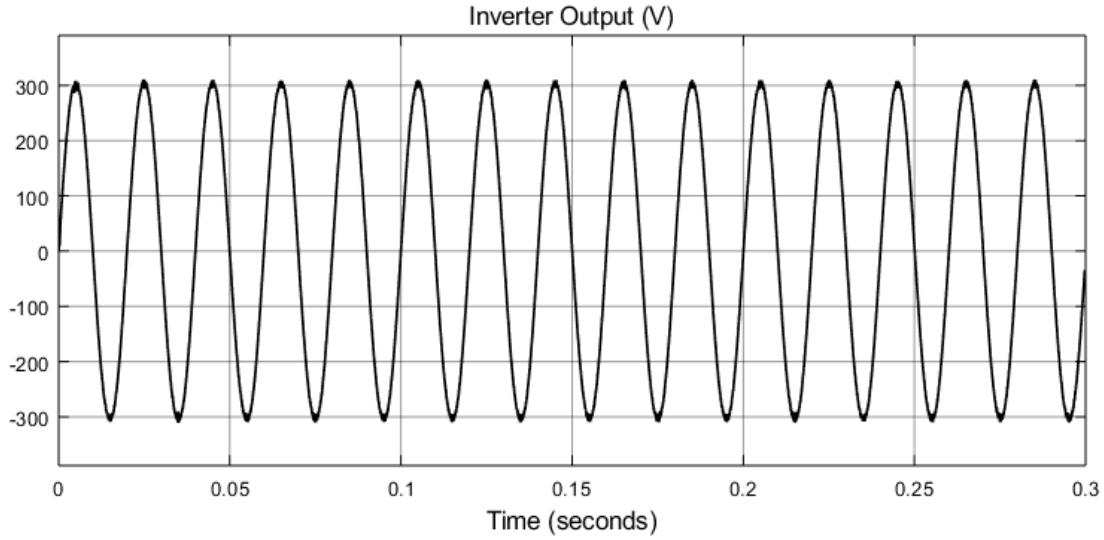


Figure 3.29 Inverter Output (TDC) - 1st Case

3.4.5.2 Maximum Load with Low-to-High Voltage Transition

This case checked the system at the maximum load when the converter input changed from a low voltage (45V, 0s ~ 0.15s) to a high voltage (55V, 0.15s ~ 0.3s). These two values, which are lower and higher than the lower and upper limit of the battery-storage voltage, are designed to check the system performance under extreme conditions. The input and output voltage of the converter is shown in figure 3.30 and 3.30 respectively.

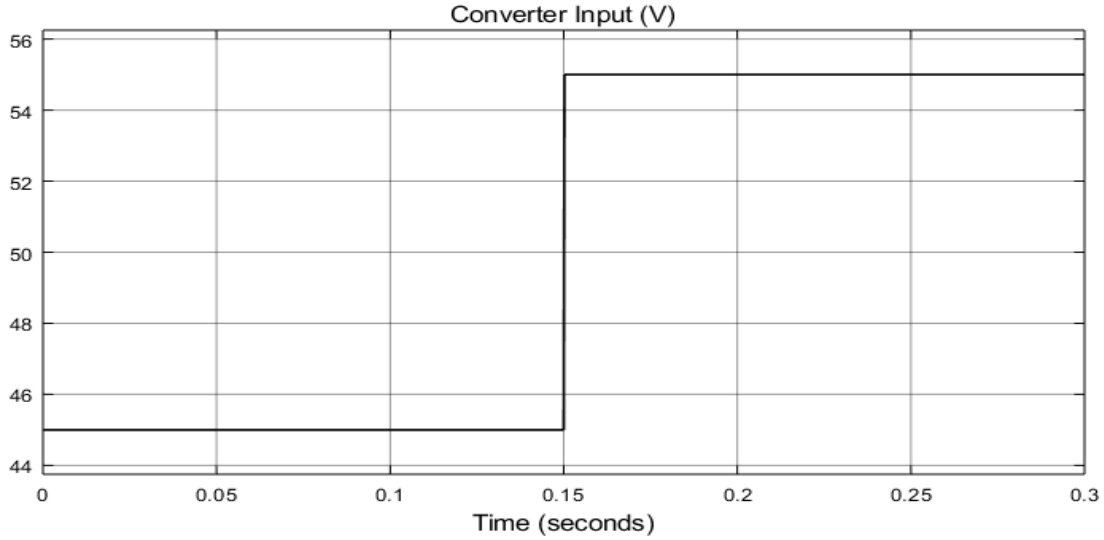


Figure 3.30 Converter Input - 2nd Case

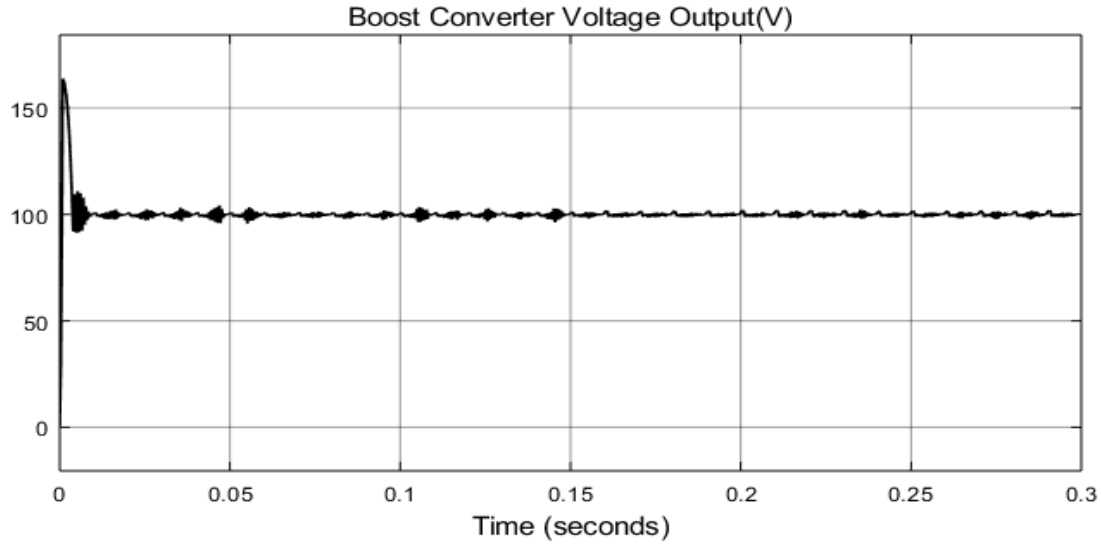


Figure 3.31 Converter Output (TDC) - 2nd Case

According to figure 3.31, during 0s to 0.15s when the input voltage is low, the maximum voltage ripple oscillates from -4V to +4V. This is just a part of the converter output during this time. When the input voltage is high (0.15s to 0.3s), the voltage ripples oscillate from -2V to +2V. The voltage transition at 0.15s results in a negligible effect on the converter output. Therefore, the distortion of the inverter output voltage is very small, which is shown in figure 3.32 below.

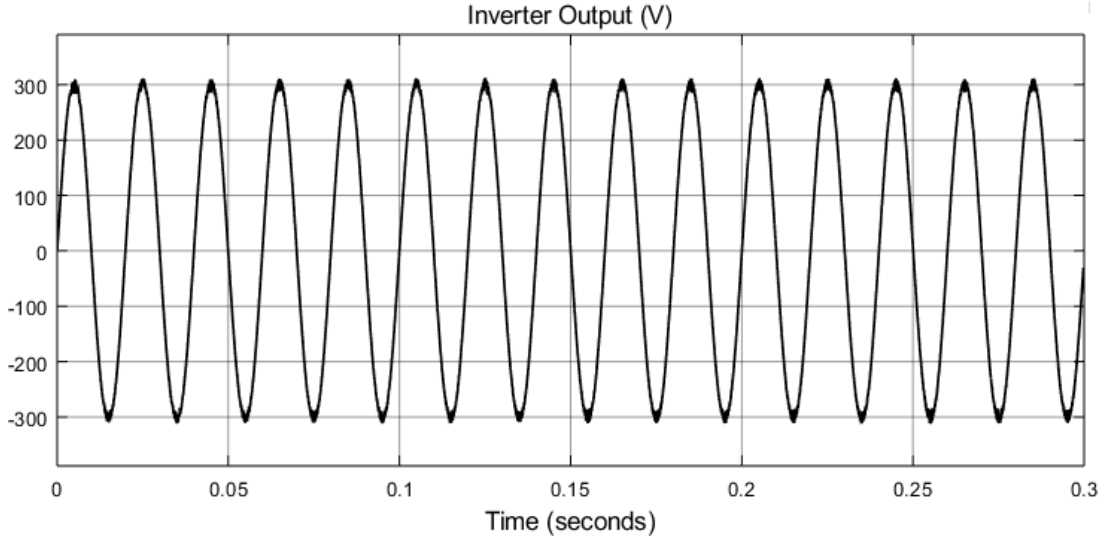


Figure 3.32 Inverter Output (TDC) - 2nd Case

3.4.5.3 Maximum Load with High to Low Voltage Transition

Compared to the 2nd case, this case checks the system performance under the maximum load when the converter input voltage changed from the high voltage (45V, 0s ~ 0.15s) to low voltage (55V, 0.15s ~ 0.3s), which is shown in figure 3.33 below.

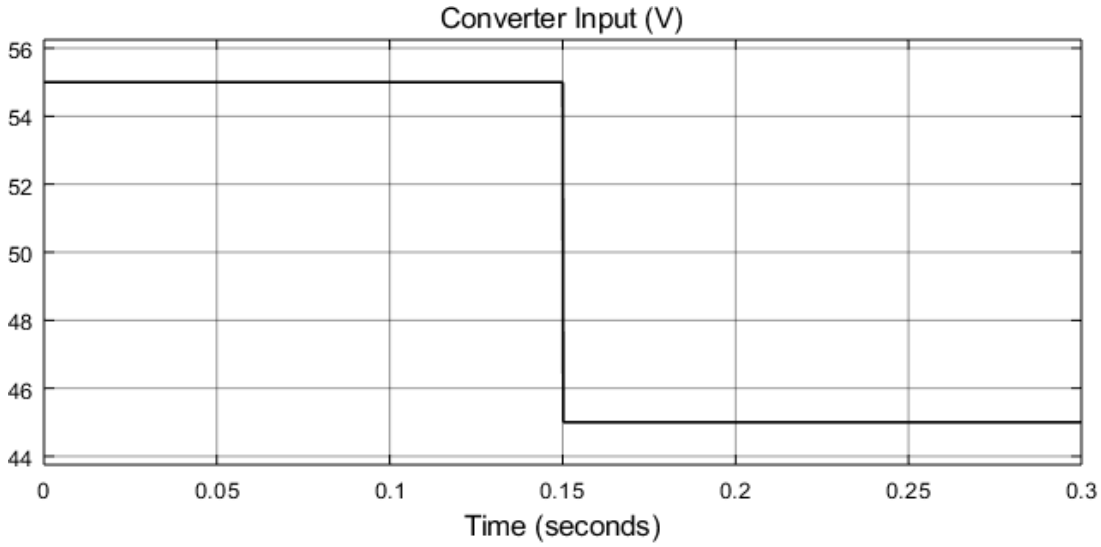


Figure 3.33 Converter Input - 3rd Case

The output voltage of the converter is shown in figure 3.34 below.

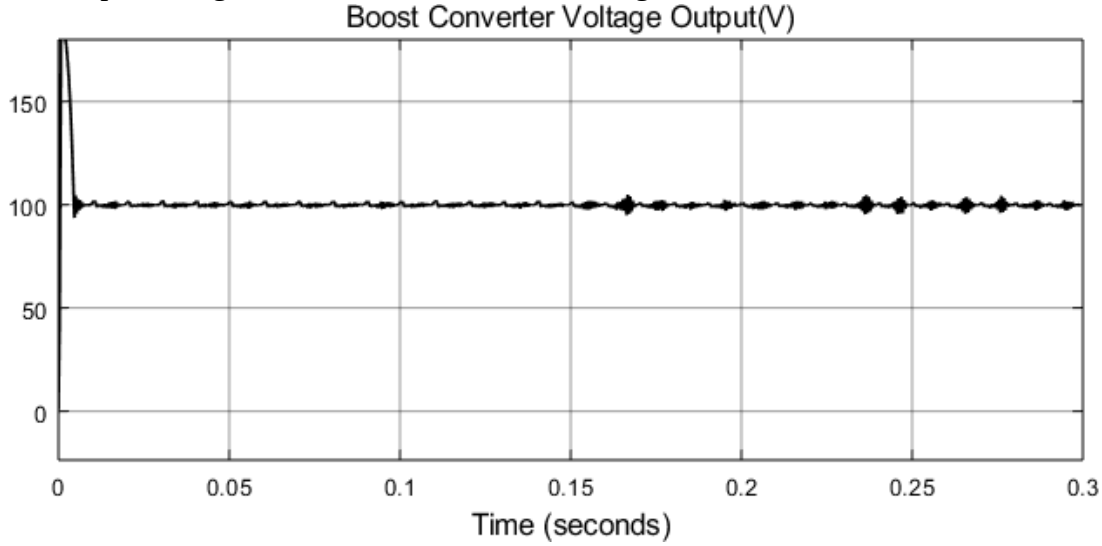


Figure 3.34 Converter Output (TDC) - 3rd Case

It can be seen from figure 3.34 that the output voltage of the converter under high and low input voltage is the same as that in figure 3.31. The voltage transient of the converter output at the voltage transition (from high voltage to low voltage, at 0.15s) is almost negligible in figure 3.34. Because the voltage ripple is very small, the inverter output voltage is only slightly distorted, which is shown in figure 3.35 below.

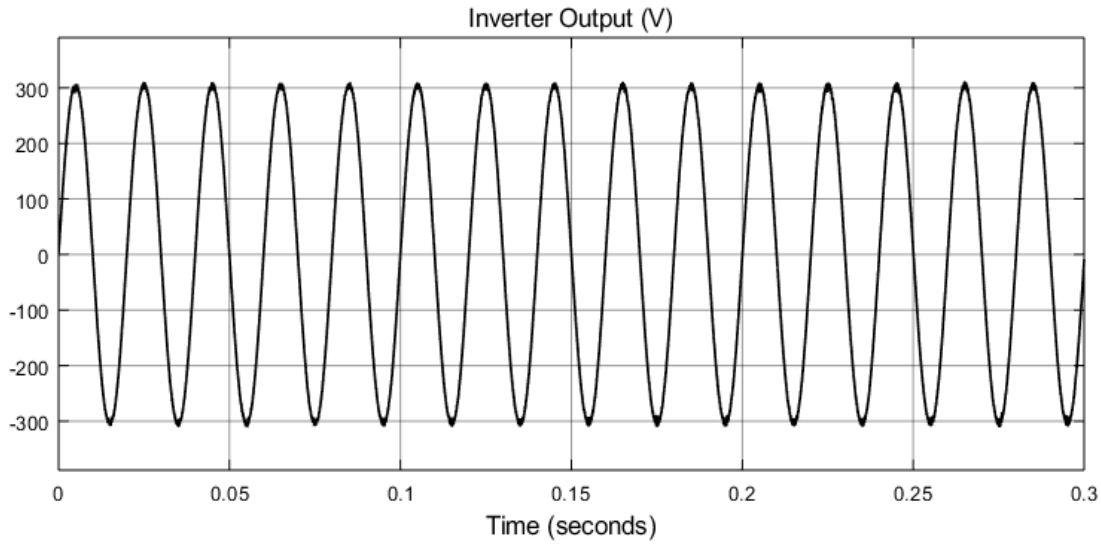


Figure 3.35 Inverter Output - 3rd Case

3.4.5.4 Light-to-Heavy Load Transition

This situation tests the system performance under normal voltage input-50V when the load is transited from $\frac{1}{18}$ to maximum load. The converter output is shown below.

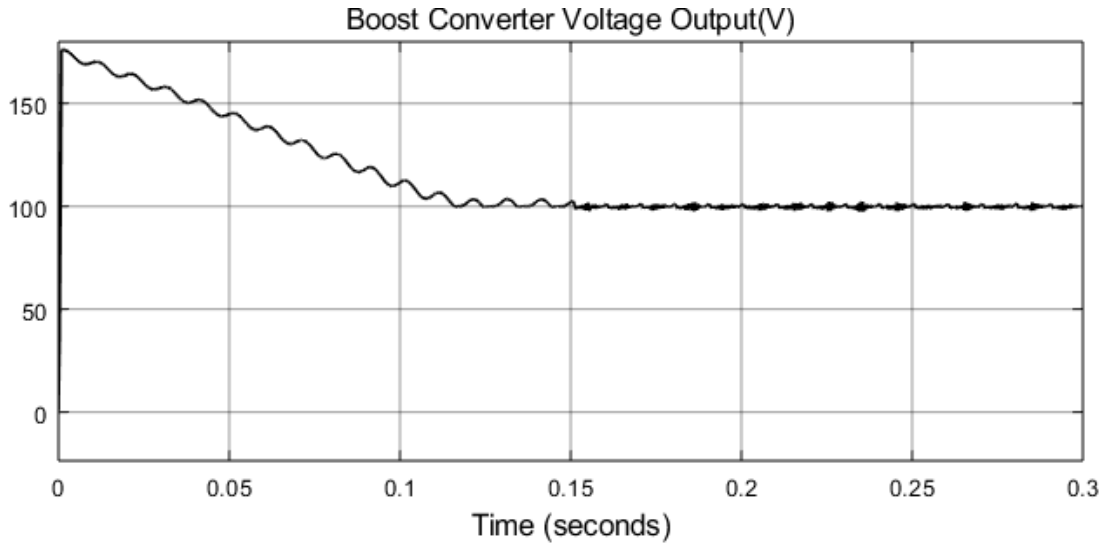


Figure 3.36 Converter Output - 4th Case

Figure 3.36 shows that during the light load (0s ~ 0.15s), the converter reaches its steady operation before the load transition. The voltage ripple during the steady operation oscillates (0V ~ 4V). After the load transition, the converter output voltage is the same as the converter that operates under 50V input voltage and maximum load. Therefore, the inverter output voltage in figure 3.37 is only a little distorted.

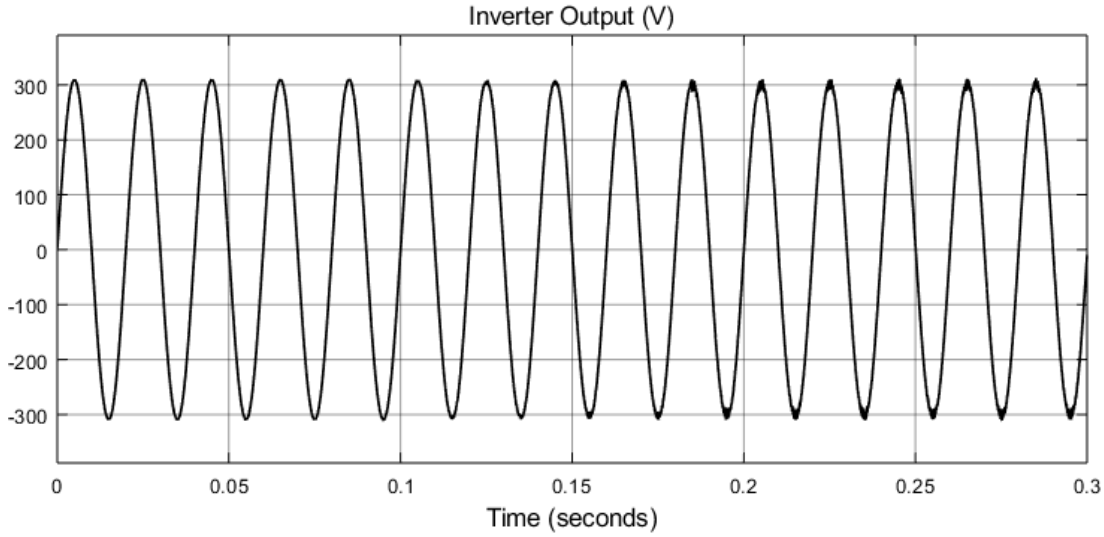


Figure 3.37 Inverter Output (TDC) - 4th Case

As it is shown in figure 3.37, the output voltage of the inverter is less distorted in light load than a heavy load. This is because, under heavy load supply, the right-half zero frequency of the boost converter is close to its resonance frequency. This leads to some resonant oscillation at the converter output voltage (0.15s ~ 0.3s, figure 3.34), and the distortion in the inverter output voltage (0.15s ~ 0.3s, figure 3.35)

Even when the converter does not reach its steady-state operation before load transition (0.05s), the TDC can still reach its steady-state operation immediately, which is shown in figure 3.38 below.

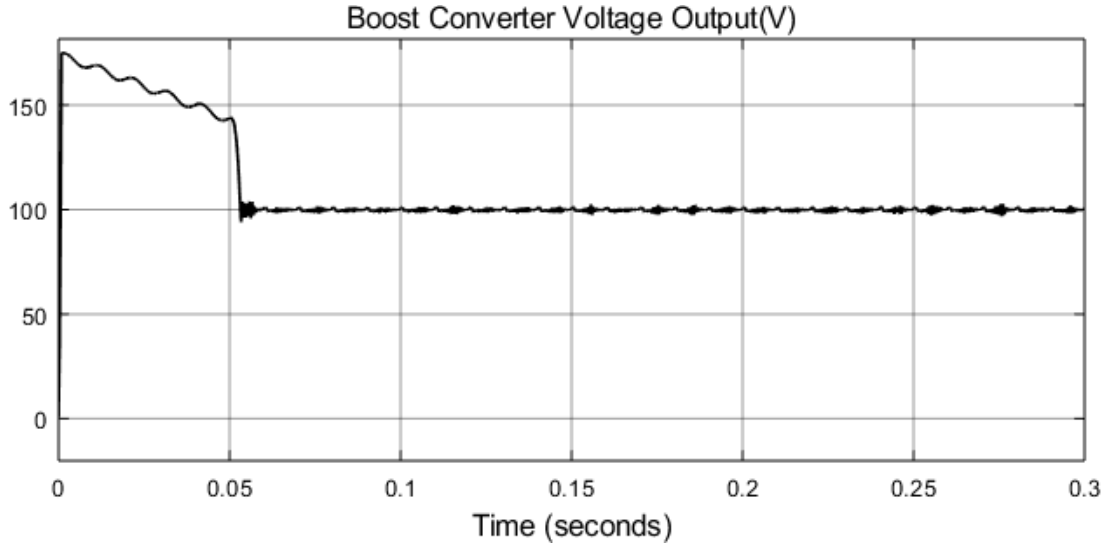


Figure 3.38 Converter Output (TDC) with Load Transition at 0.05s

3.4.5.5 Heavy-to-Light Load Transition

This case checks the system performance under normal voltage input-50V when the load is transited from the maximum load to $\frac{1}{18}$ maximum load. The output voltage of the converter is shown in figure 3.39 below.

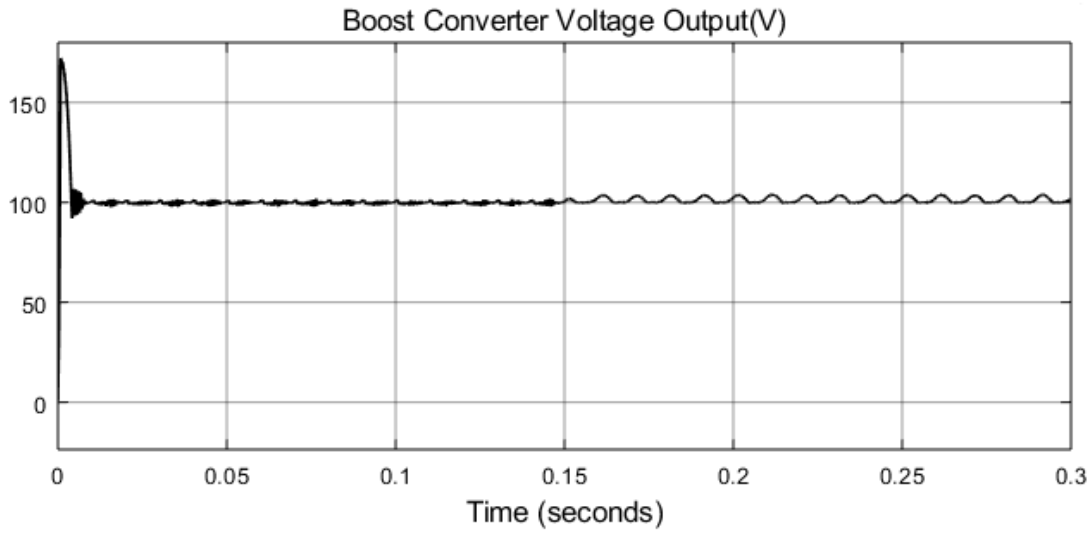


Figure 3.39 Converter Output (TDC) - 5th Case

Figure 3.39 shows that during the heavy load the output voltage ripple of the converter oscillates from -2V to +2V. When the converter reaches its steady operation (< 0.01s), the output voltage oscillates from 100V to 104V. Thus, the inverter output voltage in figure 3.40 gets little distorted.

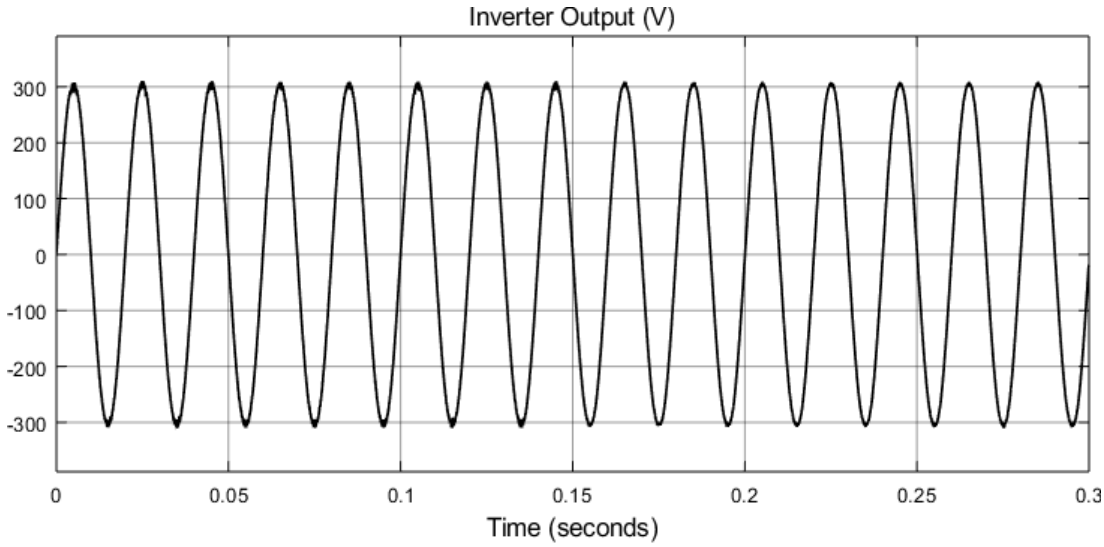


Figure 3.40 Inverter Output (TDC) - 5th Case

### 3.4.6 TDC Tuning of Boost Converter

In [23] and [49], the parameters need to be tuned are time delay constant and the gains in the reference matrixes. In this project, the time delay constant ($L$) is set equal to the system sampling time (0.00005s), and the reference gain-P is set to 15200. As it is mentioned in section 3.4.4.2, the most frequently tuned parameters are $I_{ra}$ and $R_{L.ra}$. Their tuning processes are shown below.

#### 3.4.6.1. Tuning of $I_{ra}$, $R_{L.ra} = 4R_L$

According to [50], the stability domain of $I_{ra}$ is [0, 514]. In this domain different $I_{ra}$ results in different performance. The tuning process of $I_{ra}$ is shown below.

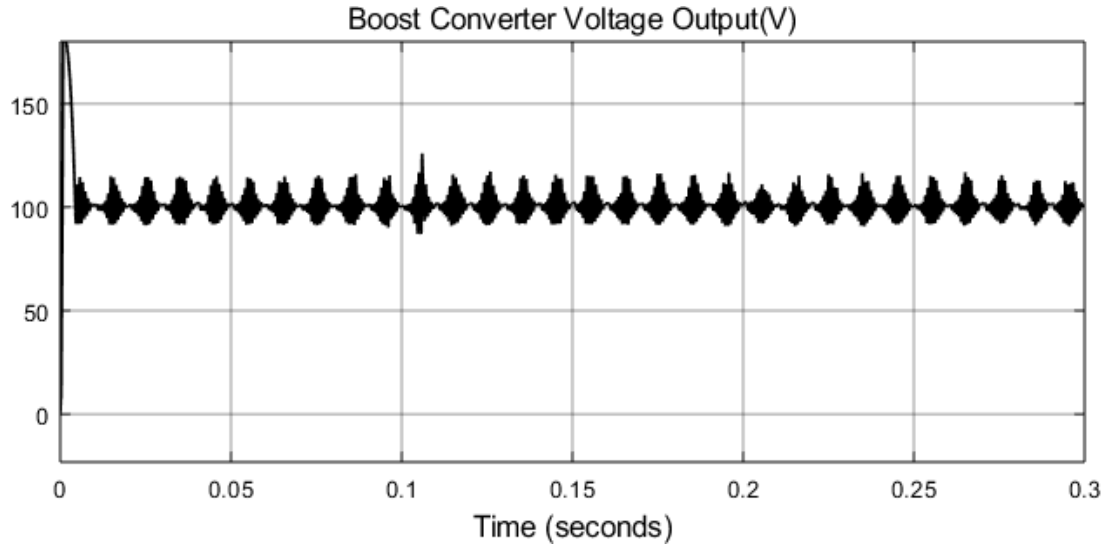


Figure 3.41 Converter Output ($I_{ra} = 200$) TDC

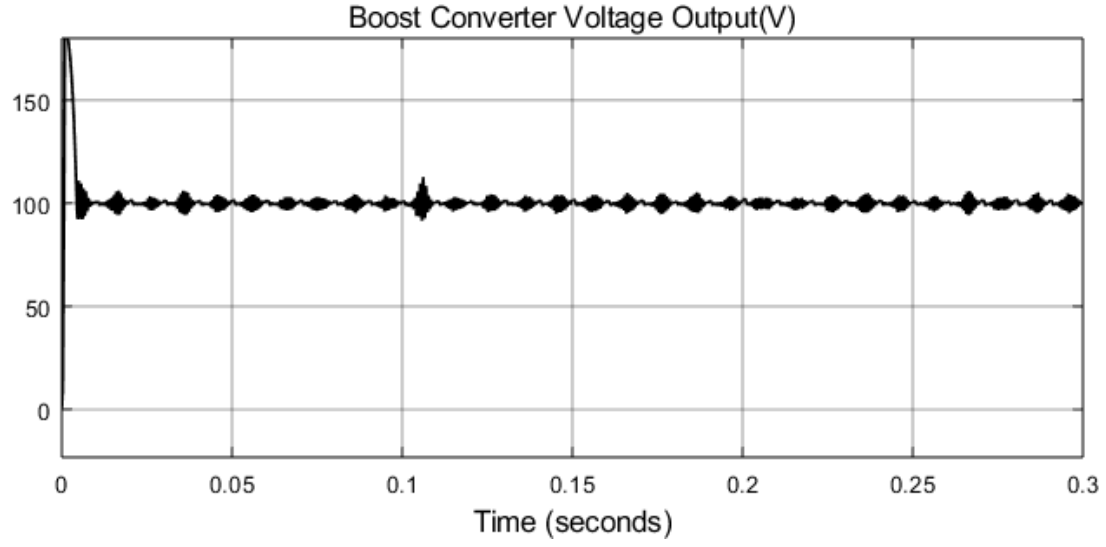


Figure 3.42 Converter Output ($I_{ra} = 100$) TDC

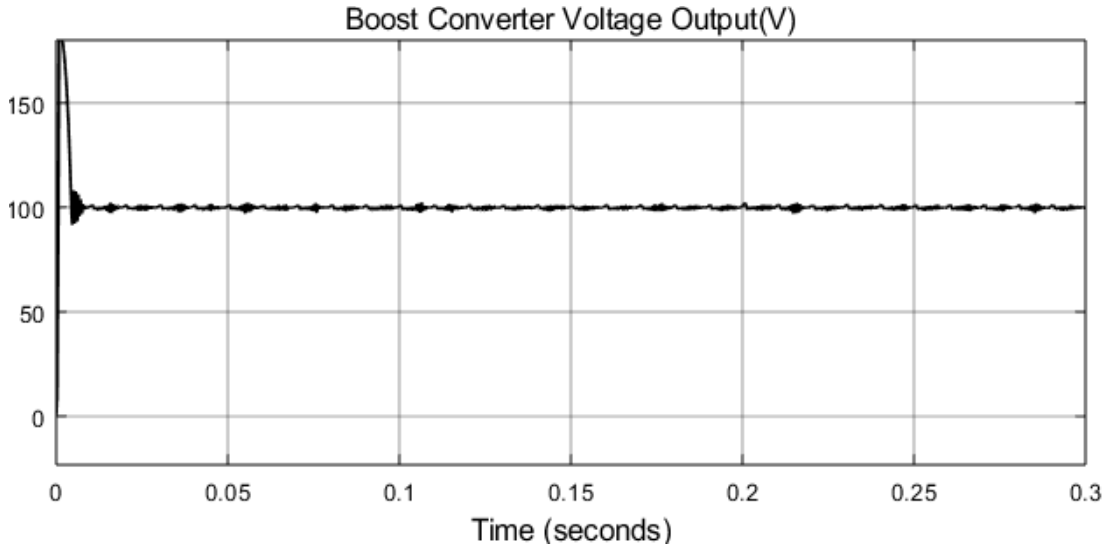


Figure 3.43 Converter Output ($I_{ra} = 42.182$) TDC

It can be seen from figure 3.41 to 3.43 that the voltage ripple of the converter output voltage decreases as $I_{ra}$ declines. As long as $\hat{B} = \frac{I_{ra}}{C}$ is in the stable domain, decreasing $I_{ra}$ can increase the accuracy of the uncertainty estimation $\hat{B}u(t-L) = \frac{I_{ra}}{C}u(t-L)$ in the control law (equation 3.41). This can improve the performance of the converter and thus inverter.

3.4.6.2. Tuning of $R_{L.ra}$, $I_{ra} = 42.182$

As it is mentioned in section 3.4.4.2, $R_{L.ra}$ estimates the uncertain dynamic $\frac{V_o(t)}{C(R_L+r_C)} - \frac{V_o(t)}{CR_{L.ra}}$. Its tuning process is shown below.

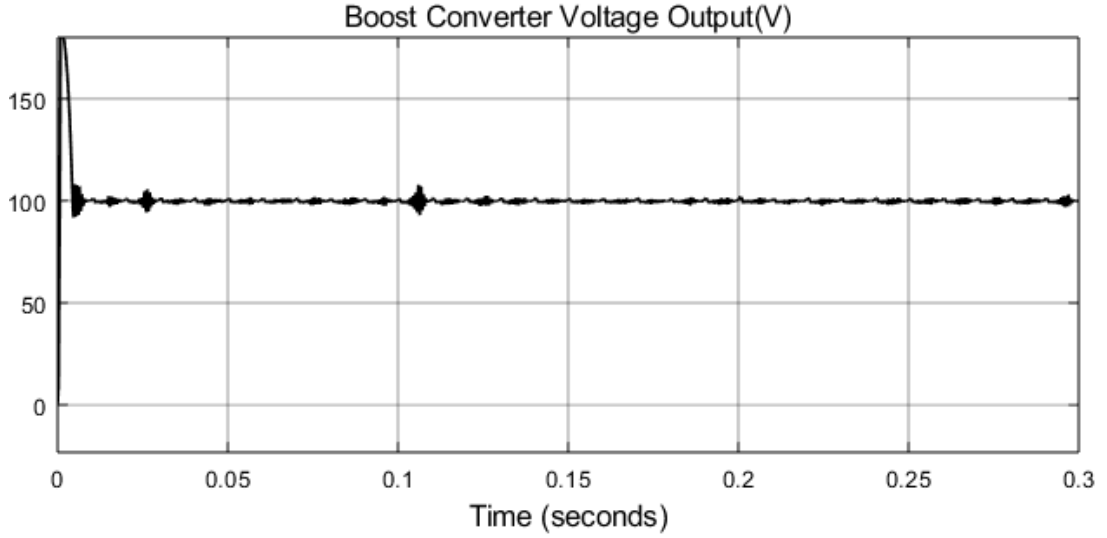


Figure 3.44 Converter Output ($R_{L.ra} = 0.5R_L$) TDC

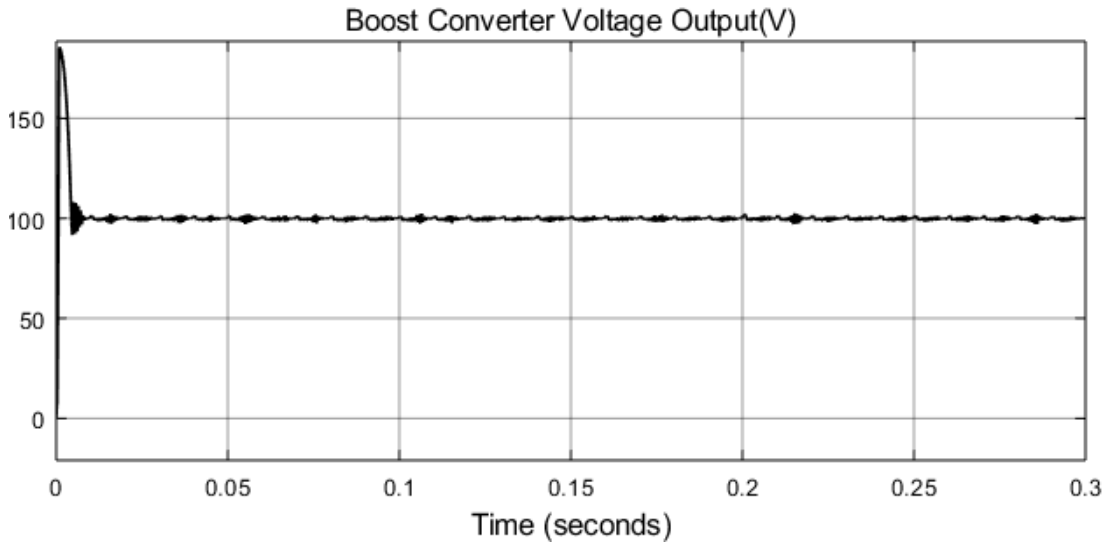


Figure 3.45 Converter Output ($R_{L.ra} = 4R_L$) TDC

Figure 3.44 and 3.45 show that $R_{L.ra}$ corresponds to the performance of the converter output voltage under input voltage disturbance at 0.11s. This is because that as $R_{L.ra}$ increases, the estimation of the uncertainty $\frac{V_o(t)}{C(R_L+r_C)} - \frac{V_o(t)}{CR_{L.ra}}$ becomes increasingly accurate. Thus, the converter output voltage becomes more stable under input disturbance.

## 3.5 Conclusion

This chapter shows the dynamic modeling and simulation of the hybrid power system designed in chapter 2. It shows that the system can keep steady-state operation under the passing cloud, increasing solar radiation and the situation when the battery storage near fully charged. To improve the waveform of the inverter output voltage, a boost converter is added between the battery storage and inverter. The inverter is controlled by a more advanced PID+R+CCF controller. The TDC controller designed for the boost converter exhibits little voltage ripple under various input voltage, input-voltage transition, and load supply. The output voltage of the inverter only gets small distortion because of this TDC controlled converter. At last, the tuning process of the TDC is described to show how to get the best system performance.

# Chapter 4
# Data Logging and Visualization System

## 4.1 Introduction

To monitor the operation of a residential PV system, both data logger and data storage are needed to collect the sensors data. The data includes the PV system's voltage-current data and local weather data. However, the PV system in MUN is 5 meters away from the window through which the weather data is collected. In China PV systems maybe 25-50 meters away from homes, it is more meaningful to realize the communications among sensors by wireless data transfer rather than long metal cables. In reality, this can significantly reduce the cabling work of a large PV system with longer distances among sensors. PC receives all the data and transfer them to a web server. To monitor the system outside the campus, a web server is used instead of a local server, which allows a much more frequent data logging (once per second). During the data transformation from a PC to a web server, the stability and robustness of the program must be guaranteed. The system alarm that reports the data-disconnection failure is also necessary to notify the user to resume the data connection as fast as possible. This chapter will first introduce the general system setup, then present each part of the system in detail, and analyze the collected data and make a conclusion.

## 4.2 Overall System Setup

The overall system includes a PV system, weather data logger, PV system data logger, radio transmission and web transfer system on a PC. Its schematic is shown in figure 4.1 below.

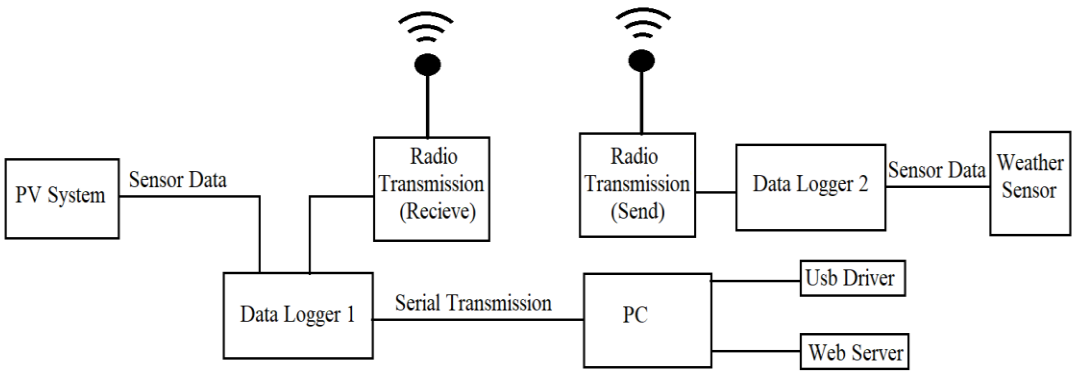


Figure 4.1 Overall System Schematic

As it is shown in figure 4.1, the weather data is first sent to data logger 2 and transmitted to data logger 1 through radio transmission. Then, by serial transmission data logger, 1 sends all sensor data to a PC. The PC transfers the data to a local USB server and web server (Thingspeak server). Since the real overall setup is hard to be included in one picture, the setups for the data logging of the PV system and weather are shown in figure 4.2 and figure 4.3 respectively. The detailed system is shown in figure 4.4.

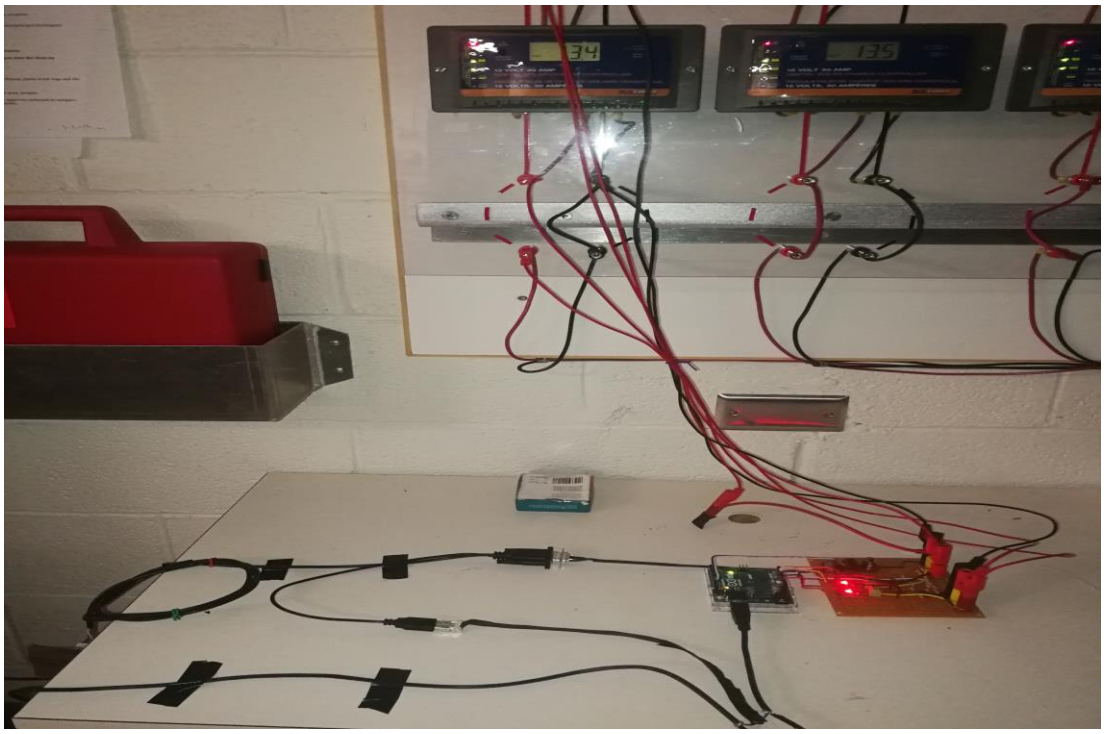

Figure 4.2 Lab Setup of Data Logging System

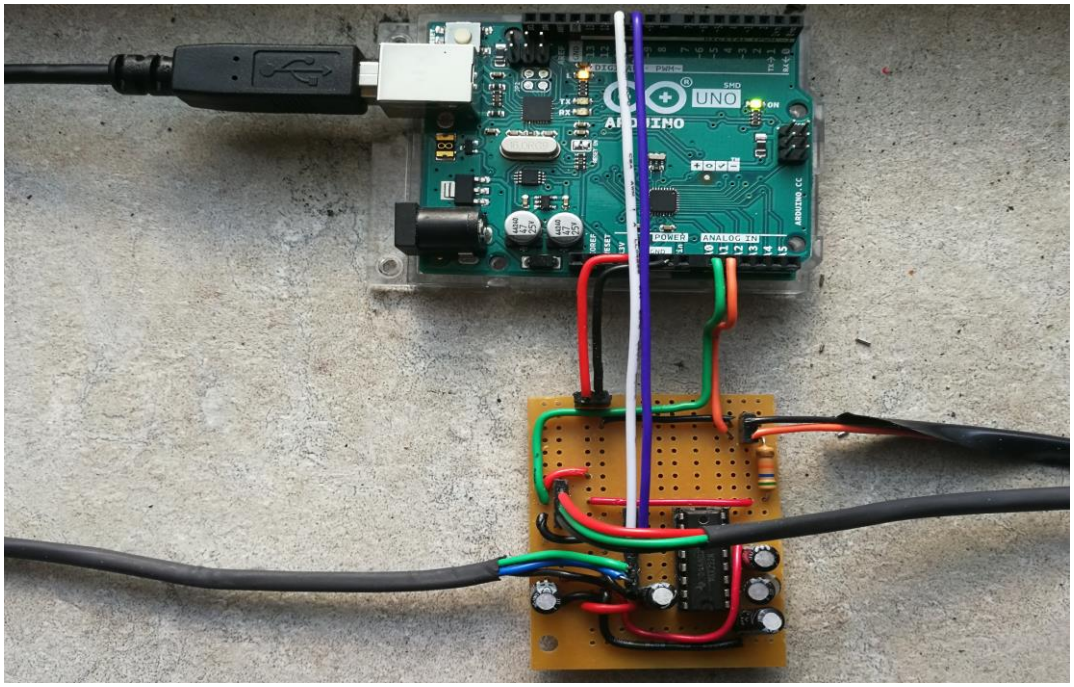

Figure 4.3 Weather Data Logger

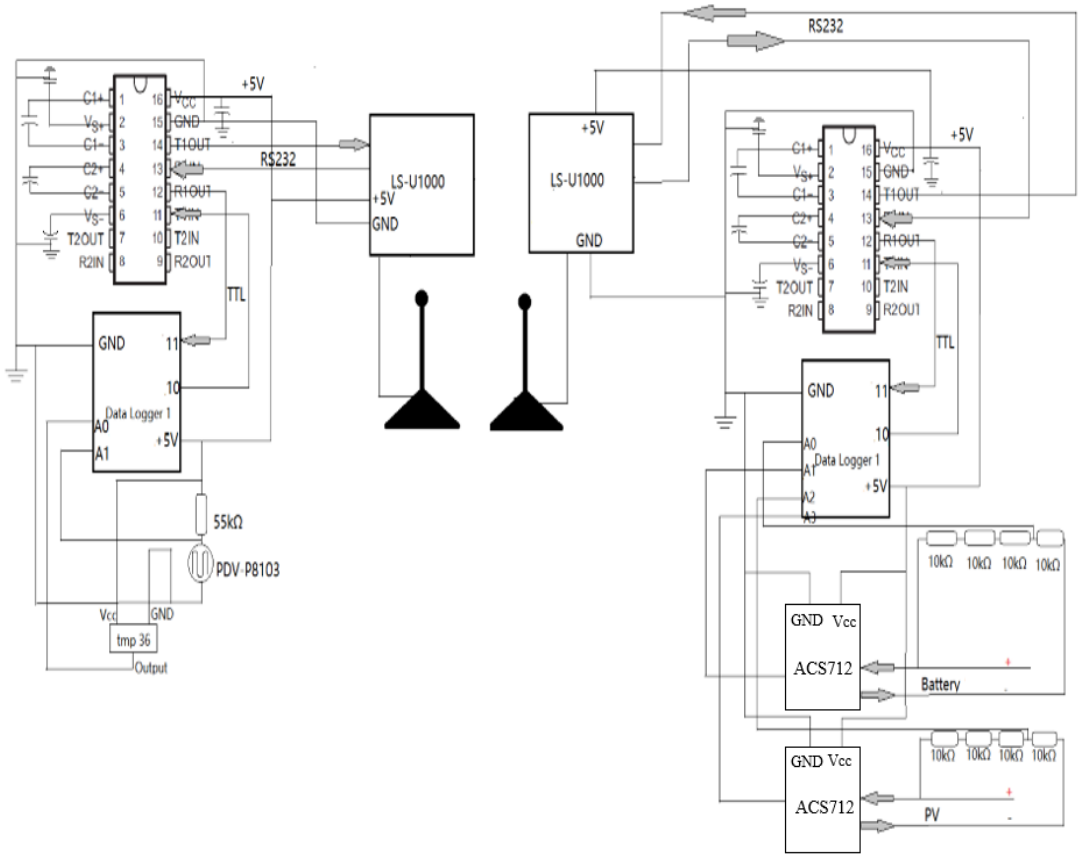


Figure 4.4 Detailed Wiring Diagram of Data Logging System

## 4.3 PV System

The overall PV system consists of a PV array, MPPT (Maximum Power Point Tracker) and battery. The PV array is composed of 2 PV panels connected in parallel (each with the 12V output voltage and 130W output power). The battery has 12V nominal output voltage and 200 Ah nominal capacity. The nominal voltage and current of MPPT are 12V and 30A respectively. Other detailed information of all these components is listed in [51,52,53]. The overall PV system is shown in figure 4.5 below.

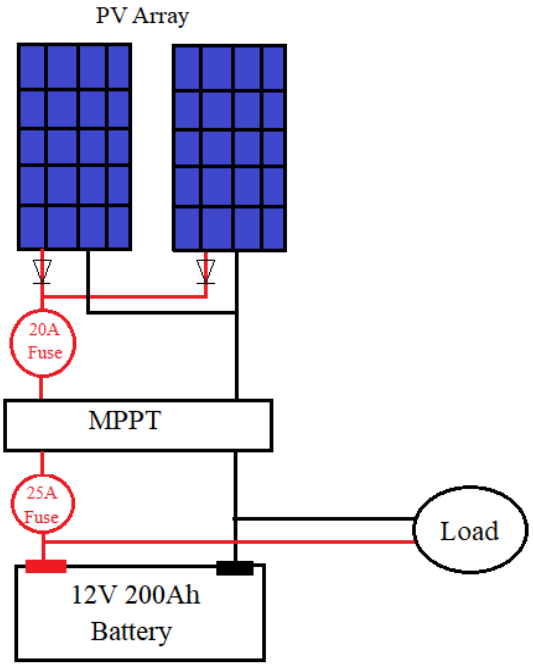


Figure 4.5 Overall PV System

As it is shown in the figure above, during daytime the PV array transforms the solar radiation to electricity through photovoltaic effect, then transmits the electrical power to MPPT. MPPT is a DC-DC converter which is used to reach the maximum power output of the PV array for the given temperature and solar radiation by adjusting the output voltage of the PV array. After the MPPT, the electricity charges the battery and supplies the load. During nights when there is no solar radiation, the output voltage and power of the PV array drops to zero. The blocking diodes at the output of the PV panels prevent battery discharging during these periods. The PV system in the lab (without PV array) is shown in figure 4.6 below.

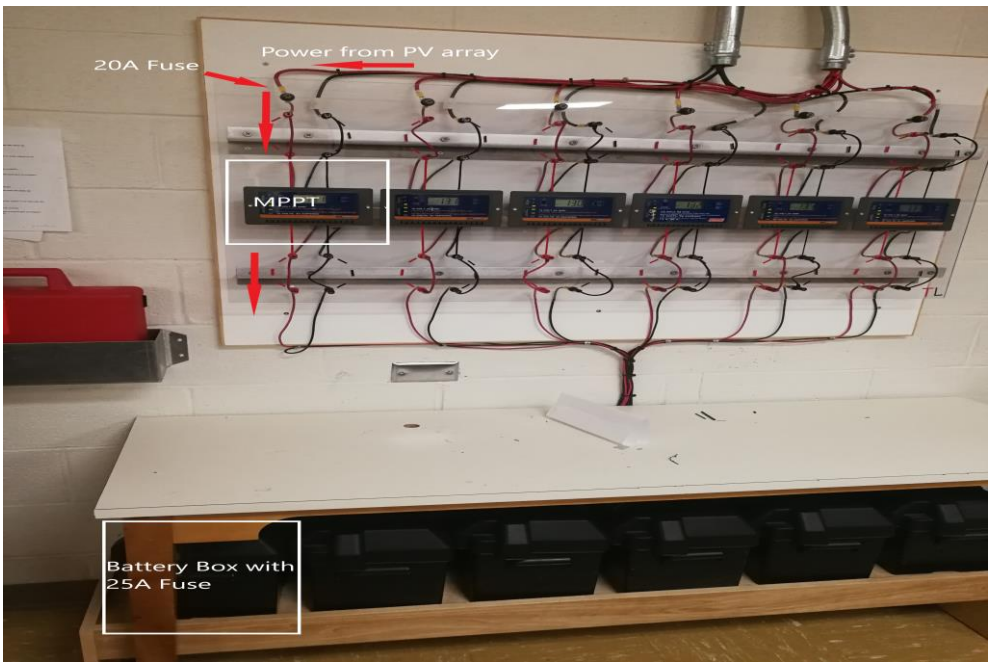


Figure 4.6 PV System in Lab (without PV Array)

## 4.4 Sensors

There are two sensor circuits, one for collecting the PV system's data and the other for the weather data. The sections below will discuss the sensors and sensor circuits in detail.

### 4.4.1 Sensors in PV System

The sensors in the PV system include two current sensors (same version) and two voltage dividers. The ratios (primary voltage to secondary voltage) of the voltage dividers of battery voltage and PV voltage are 4:1 and 6.56:1 respectively. The PV voltage divider and battery voltage divider are composed of four resistors, which are shown in Figure 4.7 below.

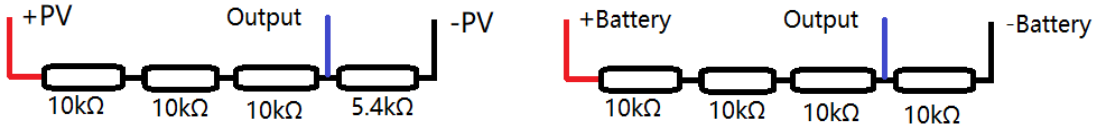


Figure 4.7 Voltage Divider

The outputs in the figure above are analog values. Arduino will transform the analog values into digital values by equation 4.1.

$$Data = measured\_value \times 1024/reference\_value \quad (4.1)$$

Thus, the real-time measured voltage should be calculated by equation 4.2 below.

$$V_{real} = Data * \frac{Ratio}{204.6}\ (V) \quad (4.2)$$

The $Ratio$ for the PV voltage divider is 6.56, and for battery voltage divider is 4.

The adopted current sensor is ACS712, which is shown in figure 4.8 below.


Figure 4.8 Current Sensor

The offset output voltage of the current sensor is 2.5V, the current range is from -20A to 20A and the sensitivity is 180mV/A. Other detailed data of the current sensor is shown in reference [54]. The testing results of the current sensor measuring PV output current and the current sensor measuring battery input current are shown in table 4.1 and table 4.2 respectively:

| Input Current (A) | Output Voltage (V) | Average Sensitivity(V/A) |
|---|---|---|
| 0 | 2.487 | 0.187 |
| 1 | 2.671 | |
| 2 | 2.855 | |
| 2.38 | 2.928 | |

Table 4.1 Test Result of PV Current Sensor

| Input Current (A) | Output Voltage (V) | Average Sensitivity(V/A) |
|---|---|---|
| 0 | 2.499 | 0.1872 |
| 1 | 2.683 | |
| 1.99 | 2.867 | |
| 2.46 | 2.958 | |

Table 4.2 Testing Result of Battery Current Sensor

Similarly, the real-time current value should be calculated by equation 4.3 below.

$$I_{real} = \frac{Data}{38.51} - 13.32 \text{ (A)} \quad (4.3)$$

4.4.2 Sensors for Weather Data

Collected weather data includes the data of solar radiation and temperature. The light dependent resistor is PDV-P8103. Its sensitivity (lg(R100)–lg (R10)/lg(E100)-lg(E10)) is 0.75, and its typical performance is shown in figure 4.9. Other detailed data is shown in [56]. The complete circuit to sense solar radiation is shown in figure 4.10.

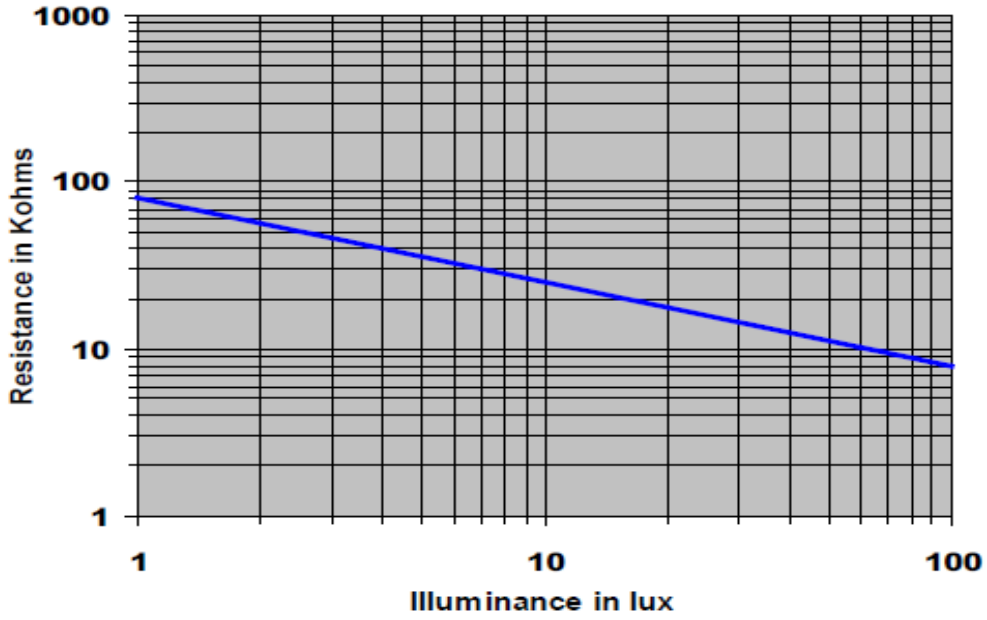


Figure 4.9 Typical Performance of PDV-P8103

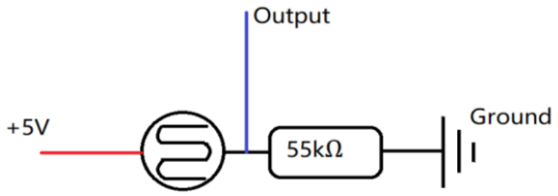


Figure 4.10 Circuit of Solar Sensor

According to the given data and the performance curve of the light dependent resistor, the solar radiation is calculated by equation 4.4 below.

$$Ra = 0.0079 * 10^{(2.5311 - lg(55.7 * data/(1170.31 - data)))} \quad (4.4)$$

The adopted temperature sensor is tmp36. Its offset output voltage is 0.5V, its output

voltage scaling is 10mV/°C, and its output voltage at 25°C is 750mV. Other detailed data is in reference [58].

The real-time temperature is calculated by equation 4.5 below.

$$T = Data/1.945 - 50 \quad (4.5)$$

## 4.5 Radio Communication System

The radio communication system is used to transmit data between data logger 1 and data logger 2. The radio transmission system is based on 2 LS-U1000 RF modules with RS232 interface. Either LS-U1000 RF module can be the transceiver or receiver without programming. The RS232-TTL interface boosts the digital signals in the TTL level (0 – 5V) from one data logger to RS232 level (±8.5V). LS-U1000 RF circuit modulates the boosted signal to electric current and sends it to transceiver antenna to be transformed into radio waves. The receiving antenna (conductor) then transforms the electromagnetic wave into electric wave (current). Then, the receiver (LS-U1000) transforms the current into digital signals, and send it to another data logger through RS232-TTL interface. The overall communication system is shown in figure 4.11.

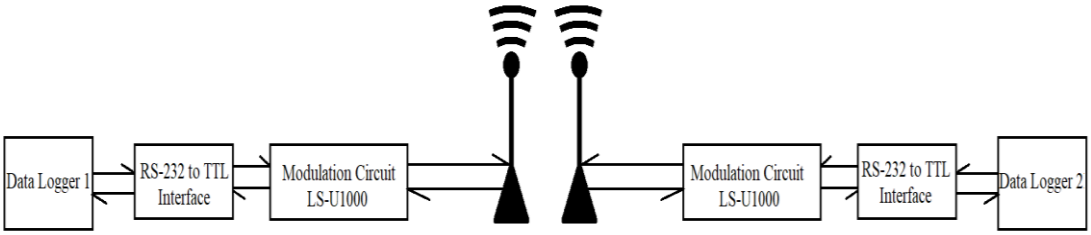


Figure 4.11 Overall Radio Communication System

Since LS-U1000 communicates with other devices by using RS232 protocol, the RS232-TTL interface circuit is needed to boost the TTL-level (0 – 5V) signals from data logger up to RS232 level (±8.5V), or level down the RS232-level signals to TTL level for the data logger. Otherwise, the signal in the RS232 level may destroy the data logger. The detailed description of the RS232-TTL interface circuit is shown in section 4.5.1 below.

4.5.1 RS232-TTL Interface

The RS232-TTL interface is based on MAX232. It uses a capacitive voltage generator to supply RS232 voltage level [55]. It has two receivers and two transceivers. Each receiver levels down the RS232-level signals to TTL level and each driver boosts up the TTL- level signals to RS232 level. Other detailed data is shown in [55]. Since the interface circuits for transmitter and receiver are equally same, the only one-side interface circuit is shown in figure 4.12 below.

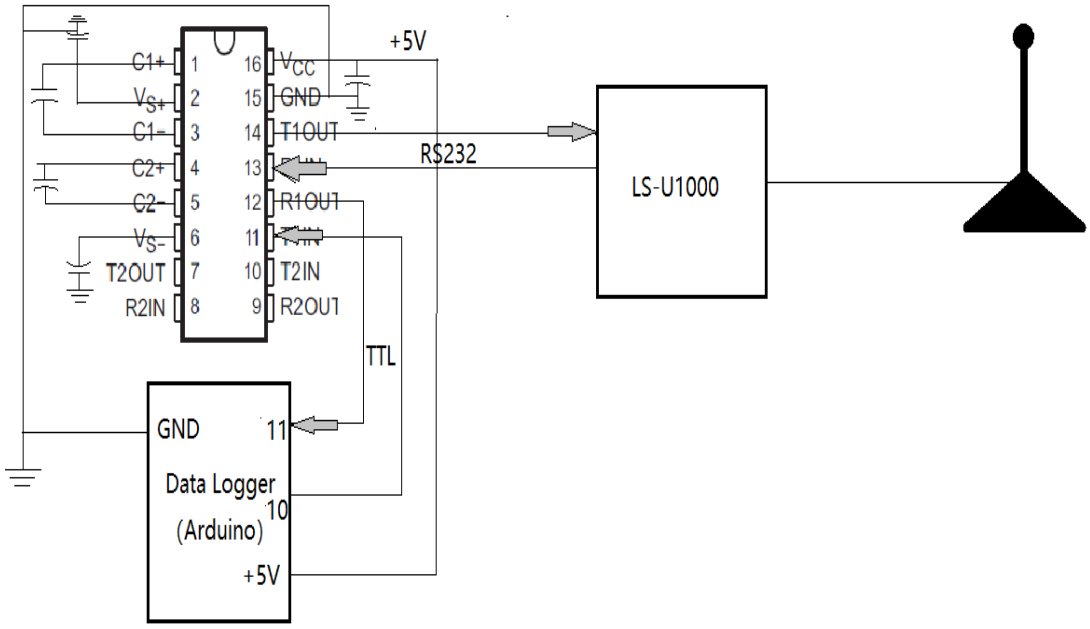


Figure 4.12 Detailed RS232-TTL Interface

As it is shown above, the output signal (TTL level) from pin 11 of one Arduino board are transmitted to the input of MAX232's driver #1. The output signals from driver #1 are then boosted up to RS232 level and sent to LS-U1000, which transforms the signal to electric current and send it to the antenna. The antenna transforms the electric wave into a radio wave, which is then received by receivers and transformed into TTL-level signals to the other Arduino logger.

## 4.6 Programs in Arduino Boards and Python Script

### 4.6.1 Program of Arduino Boards (Data Loggers)

Arduino boards collect the sensor data, calibrate it then send it to PC for further processing. Besides data logging, as it is shown in figure 4.1, data logger 2 needs to communicate with data logger 1 to get its collected sensor data. Synchronization is needed between data logger 1 and data logger 2, to get the accurate and real-time value of the solar radiation and temperature from data logger 1.

The flow chart of the program of data logger 1 and data logger 2 is shown in figure 4.13 and 4.14 below.

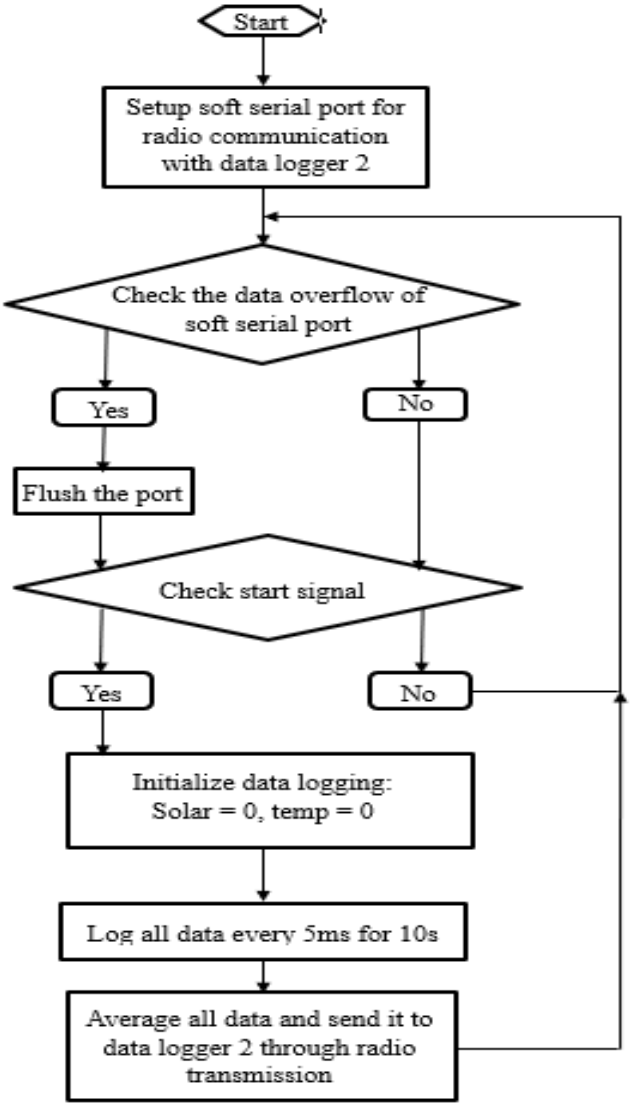


Figure 4.13 Program Flow Chart of Data Logger 1

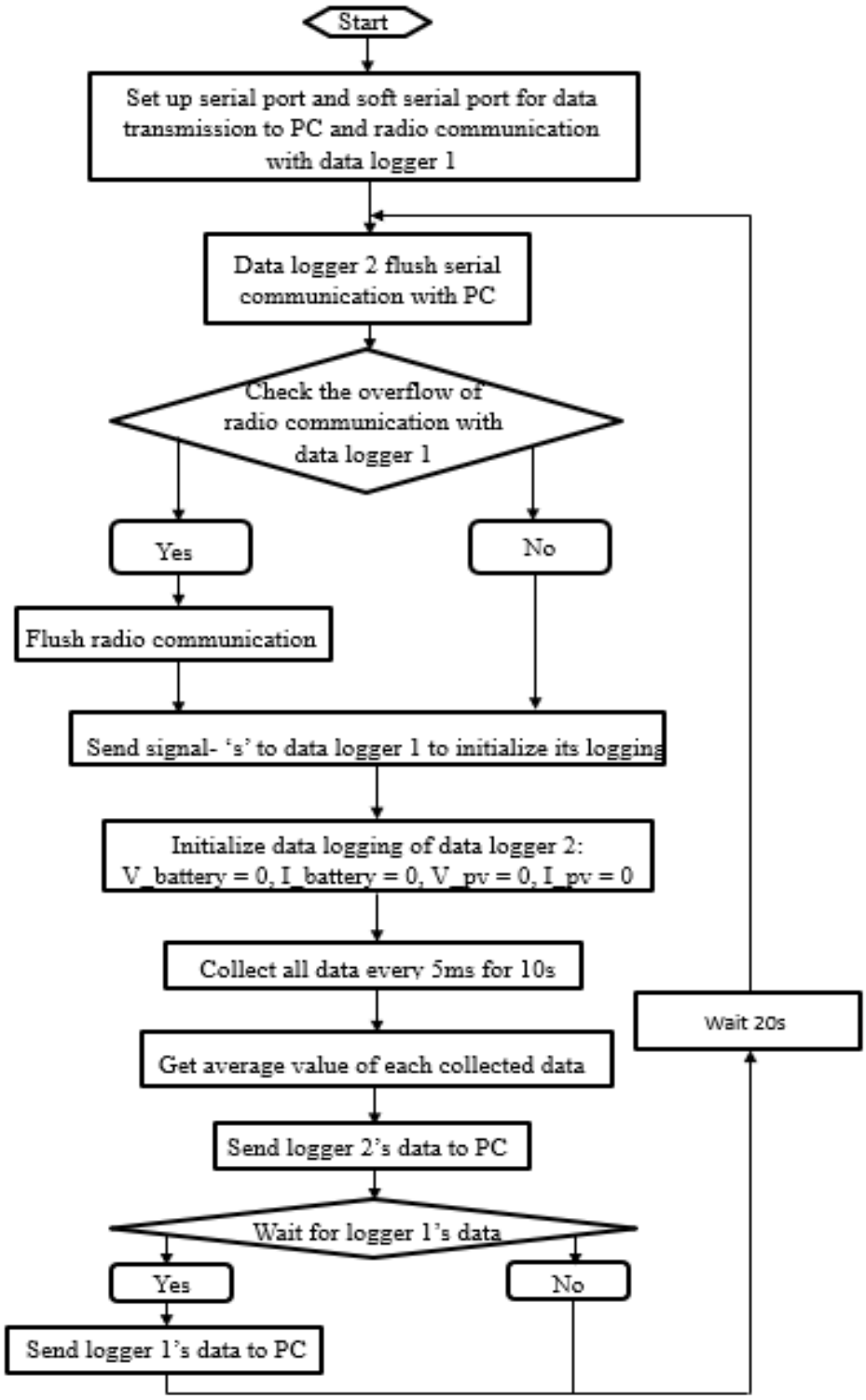


Figure 4.14 Program Flow Chart of Data Logger 2

It can be seen from figure 4.14 that data logger 2 not only collects the PV system's data (current and voltage) but also receive the weather data from data logger 1 through radio transmission. After setting up the serial and software serial port transmitting data to PC

and data logger 1 respectively, data logger 2 flushes the serial buffer to guarantee that the most recent data are sent to PC. After flushing the serial port connected with the PC, it checks the overflow of the software serial buffer, which guarantees that data logger 2 receives the most recent data from logger 1. Then, logger 2 sends the start signal- 's' to logger 1, and logger 1 begins collecting weather data. This process includes initializing variables, collecting and calibrating data. After sending the processed data to the PC, it waits for the data from data logger 1. Once the data from logger 1 are sensed, logger 2 will send them to the PC and start the next loop after the 20s; otherwise, it will directly start the loop after 20s without sending weather data.

Data logger 1 (as shown in figure 4.13) flushes its software serial buffer first once getting the start signal from logger 1. It then collects and processes weather data. After finally sending data to data logger 2, logger 1 will return to the beginning of its loop and wait for the next start signal. The program of data logger 1 and data logger 2 are shown in figure 4.15 and 4.16 respectively.

```
#include <SPI.h>
#include <SoftwareSerial.h>

int rx = 10;
int tx = 11;
int tempPin = A0;
int solarPin = A1;
int average_time = 2000;

SoftwareSerial mySerial(rx, tx); // RX, TX

void setup() {
  Serial.begin(9600);

  while (!Serial) {
    ;}

  mySerial.begin(9600);
  analogReference(DEFAULT);
}

void loop() {

    if(mySerial.overflow()){
      ;
    }
    else{
      ;
    }

    Serial.flush();

    if(mySerial.read() == 'a'){
```

```
      float temp = 0;
      float solar = 0;

      for(int i=0; i<average_time; i++){
        temp += analogRead(tempPin);
        solar += analogRead(solarPin);
        delay(5);
      }

      String temp1 = 't' + String(temp/average_time) + 'T';
      String solar1 = 's' + String(solar/average_time) + 'S';

      mySerial.print(temp1+solar1+"\n");
      Serial.print(temp1+solar1+"\n");
    }

    else{
      ;
    }

}
```

Figure 4.15 Program of Data Logger 1

```
#include <SPI.h>
#include <SoftwareSerial.h>

int rx = 10;
int tx = 11;
int voltage_baPin = A0;
int current_baPin = A1;
int voltage_pvPin = A2;
int current_pvPin = A3;
int average_time = 2000;

SoftwareSerial radio_receive(rx,tx);//RX,TX

void localread(){

  float voltage_ba = 0;
  float current_ba = 0;
  float voltage_pv = 0;
  float current_pv = 0;

  for(int i = 0; i < average_time; i++){
      voltage_ba += analogRead(voltage_baPin);
      current_ba += analogRead(current_baPin);
      voltage_pv += analogRead(voltage_pvPin);
      current_pv += analogRead(current_pvPin);
      delay(5);
    }

    String voltage_baa = 'b' + String(voltage_ba/average_time) + 'B';
    String current_baa = 'd' + String(current_ba/average_time) + 'D';
    String voltage_pva = 'p' + String(voltage_pv/average_time) + 'P';
    String current_pva = 'q' + String(current_pv/average_time) + 'Q';

    Serial.print(voltage_baa + current_baa + voltage_pva + current_pva);
```

```
}

void setup(){

  radio_receive.begin(9600);
  Serial.begin(9600);
  analogReference(DEFAULT);

}

void loop(){

  Serial.flush();

  if(radio_receive.overflow()){
    ;
  }
  else{
    ;
  }

  radio_receive.print('a');
  localread();

  while(radio_receive.available()>0){
    Serial.write(radio_receive.read());
  }

  delay(20000);

}
```

Figure 4.16 Program of Data Logger 2

### 4.6.2 Python Program on PC

The python program receives and processes the data from logger 1 back to real-time measured data, then transmits them to Thingspeak server and a local hard drive. However, for long-time data transfer, the structure of the program should be strengthened to prevent the logging from being stopped by small errors. The program firstly initializes the serial communication with data logger 2, the URL transmission with Thingspeak server and the data storage on the local USB drive. Then, it checks the dataset from data logger 2 at the serial port. If it exists, the program decodes it to string from binary mode; otherwise, it loops back to dataset checking. If there is no error during decoding, the program extracts each data (solar radiation, temperature, battery's current and voltage, and PV array's current and voltage) from the dataset; otherwise, the dataset becomes empty, and the subsequent data will also be empty. The program

then checks the availability of each extracted data (no matter it is empty or not) and transforms unavailable data to empty data. Then, the data (whether it is empty or not) is transformed from string to float data, and processed to real-time values according to equation 4.2 to equation 4.5. Next, the program checks the availability of URL transmission, and posts the real-time data to Thingspeak server if the transmission is available, then transforms the data to the USB storage; otherwise the program only sleeps 5s before the next step, in which the program saves the sensed data and current time to a local USB driver. Then, another cycle of the program begins after sleeping 5s and flushing the serial buffer. The detailed flow chart of the program is shown in figure 4.17 below.

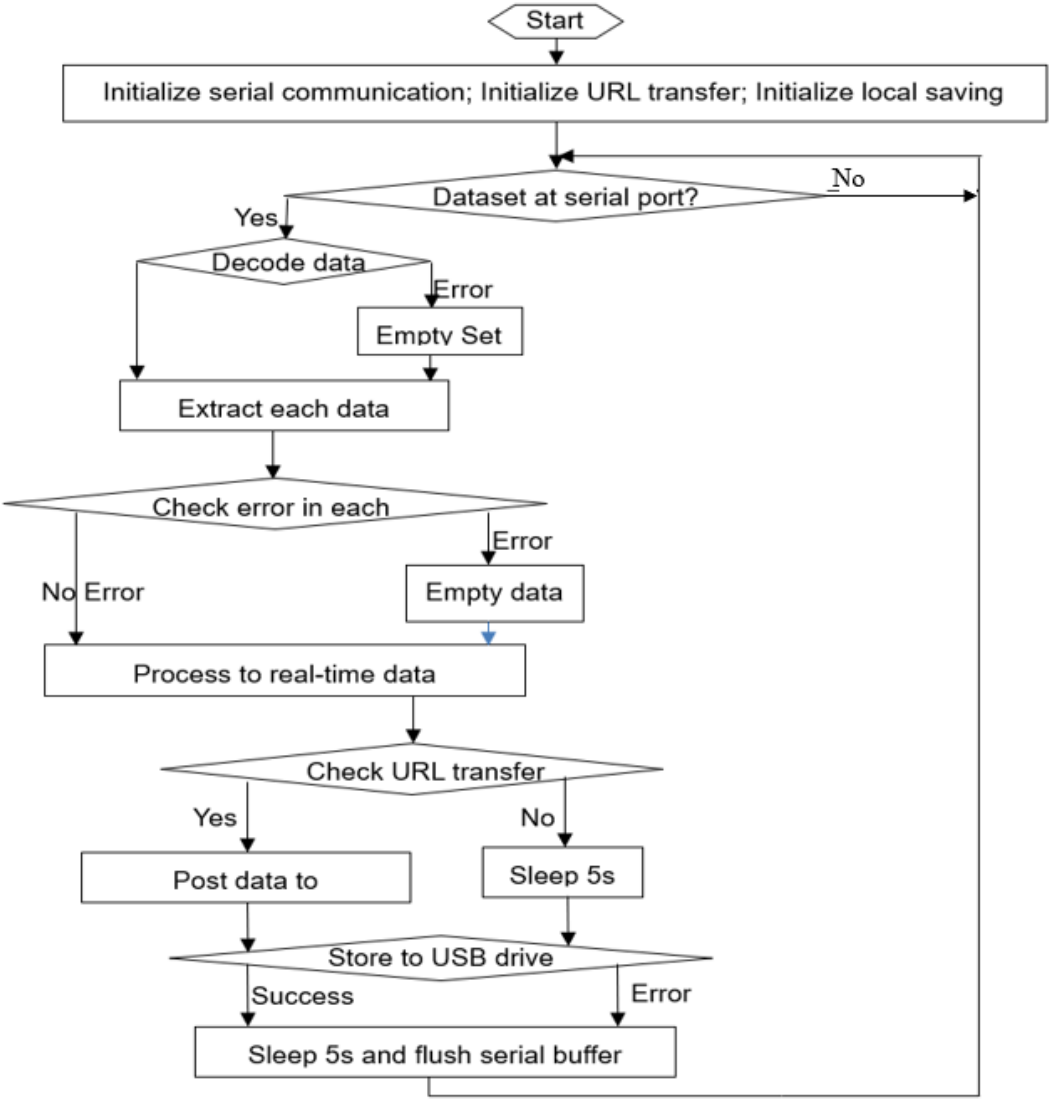


Figure 4.17 Flow Chart of Python Program

The detailed program is shown below.

```
import serial
import time
import math
import requests

def connection_check():

    try:
        requests.get('https://api.thingspeak.com/channels/547754\
                     /feeds.json?api_key=FFBE8AN8TFW087D4&result=2',timeout=1)
        return True
    except requests.RequestException:
        time.sleep(5)
        return False
    except requests.ConnectionError:
        time.sleep(5)
        return False
    except requests.HTTPError:
        time.sleep(5)
        return False
    except requests.TooManyRedirects:
        time.sleep(5)
        return False
    except requests.ReadTimeout:
        time.sleep(5)
        return False
    except requests.ConnectTimeout:
        time.sleep(5)
        return False
    except requests.Timeout:
        time.sleep(5)
        return False
    except requests.packages.urllib3.exceptions.MaxRetryError:
        time.sleep(5)
        return False
    except requests.packages.urllib3.exceptions.NewConnectionError:
        time.sleep(5)
        return False

def data_posting(url):

    if(connection_check() == True):
        try:
            requests.post(url)
        except:
            pass
    else:
        pass

def type_check(inpString):

    data = inpString

    try:
        data = float(data)
        return True
    except ValueError:
        return False

local_data = open('F:/new_data/local2.csv', 'w')
local_data.write('time'+','+'voltage_battery'+','+ 'current_battery'+','+\
                 'voltage_pv'+','+'current_pv'+','+ 'solar_irradiance'+','+\
                 +'temperature'+'\n')
local_data.close()


serl = serial.Serial('COM4',9600,timeout=1)
serl.flush()

while True:

    if(serl.inWaiting()>0):

        try:
            data1 = serl.readline().decode()
        except UnicodeDecodeError:
            data1 = ''
```

```
voltage_pv = ''
current_pv = ''
solar = ''
temp = ''

d_ind = list(range(len(data1)))

if ('b' in data1) and ('B' in data1):
    voltage_ba_sindex = data1.index('b')
    voltage_ba_eindex = data1.index('B')

    for i in d_ind:
        if (i > voltage_ba_sindex) and (i < voltage_ba_eindex):
            voltage_ba += data1[i]
        else:
            pass

    if (type_check(voltage_ba) == True):
        voltage_ba = float(voltage_ba)
        voltage_ba = voltage_ba/53.98
    else:
            pass

else:
    pass

if ('d' in data1) and ('D' in data1):
    current_ba_sindex = data1.index('d')
    current_ba_eindex = data1.index('D')

    for i in d_ind:
        if (i > current_ba_sindex) and (i < current_ba_eindex):
            current_ba += data1[i]
        else:
            pass

    if(type_check(current_ba) == True):
        current_ba = float(current_ba)
        current_ba = current_ba/38.51- 13.32
    else:
        pass

else:
    pass
if ('p' in data1) and ('P' in data1):
    voltage_pv_sindex = data1.index('p')
    voltage_pv_eindex = data1.index('P')

    for i in d_ind:
        if (i > voltage_pv_sindex) and (i < voltage_pv_eindex):
            voltage_pv += data1[i]
        else:
            pass

    if(type_check(voltage_pv) == True):
        voltage_pv = float(voltage_pv)
        voltage_pv = voltage_pv/33.05
    else:
        pass

else:
    pass

if ('q' in data1) and ('Q' in data1):
    current_pv_sindex = data1.index('q')
    current_pv_eindex = data1.index('Q')

    for i in d_ind:
        if (i > current_pv_sindex) and (i < current_pv_eindex):
            current_pv += data1[i]
        else:
            pass

    if(type_check(current_pv) == True):
        current_pv = float(current_pv)
        current_pv = current_pv/38.45- 13.32
    else:
        pass

else:
    pass

if ('s' in data1) and ('S' in data1):
    solar_sindex = data1.index('s')
    solar_eindex = data1.index('S')

    for i in d_ind:
        if (i > solar_sindex) and (i < solar_eindex):
            solar += data1[i]
        else:
            pass
```

```
            if(type_check(solar) == True):
                solar = float(solar)
                solar = pow(10, 2.5311 - 1.33*math.log10\
                            (55.7*solar/(1170.31-solar)))
                solar *= 0.0079
            else:
                pass

        else:
            pass

        if ('t' in data1) and ('T' in data1):
            temp_sindex = data1.index('t')
            temp_eindex =  data1.index('T')

            for i in d_ind:
                if (i > temp_sindex) and (i < temp_eindex):
                    temp += data1[i]
                else:
                    pass

            if(type_check(temp) == True):
                temp = float(temp)
                temp = temp/1.945 - 50
            else:
                pass

        else:
            pass

        localtime = time.strftime("%Y-%m-%d %H:%M:%S", time.localtime())

        try:
            local_data = open('F:/new_data/local2.csv','a')
            local_data.write(localtime+','+str(voltage_ba)+','+str(current_ba)+\
                             ','+str(voltage_pv)+','+str(current_pv)+','+str(solar)+\
                             ','+str(temp)+'\n')
        except:
            print("check usb driver")
            pass

        url1 = 'https://api.thingspeak.com/update/?api_key=RFW2EIQD64ZSDKGV'+\
               '&field1='+str(voltage_ba)+'&field2='+str(current_ba)+'&field3='+\
               str(voltage_pv)+'&field4='+str(current_pv)+'&field5='+str(temp)+\
               '&field6='+str(solar)
        print(localtime+" solar: "+str(solar)+"  temp: "+str(temp)+"  voltage_ba: "\
              +str(voltage_ba)+"  current_ba: "+str(current_ba)+"  voltage_pv: "+\
              str(voltage_pv)+"  current_pv: "+str(current_pv))

        data_posting(url1)

        time.sleep(5)

        serl.flush()

    else:
        pass
```

Figure 4.18 Python Program on PC

## 4.7 Data Visualization and Analysis

### 4.7.1 Basic Settings on Thingspeak Server

Thingspeak is an open online platform to collect, analysis and act on sensor data [57]. To fully visualize the collected data, six fields are set up. Field 1 is for battery voltage, field 2 for battery current, field 3 for PV voltage, field 4 for PV current, field 5 for solar radiation and field 6 for temperature. The message of connection failure is sent to a

tweet account to notify users when no data is sent to Thingspeak account (shown in figure 4.19).


Figure 4.19 Connection Failure Message on Tweet Account

### 4.7.2 Data Visualization

The data is collected every 30s for 16 days. This proves that the overall system can achieve long-time robust data log and transfer. One day's data on Thingspeak is shown in figure 4.20, 4.21 and 4.22 below.

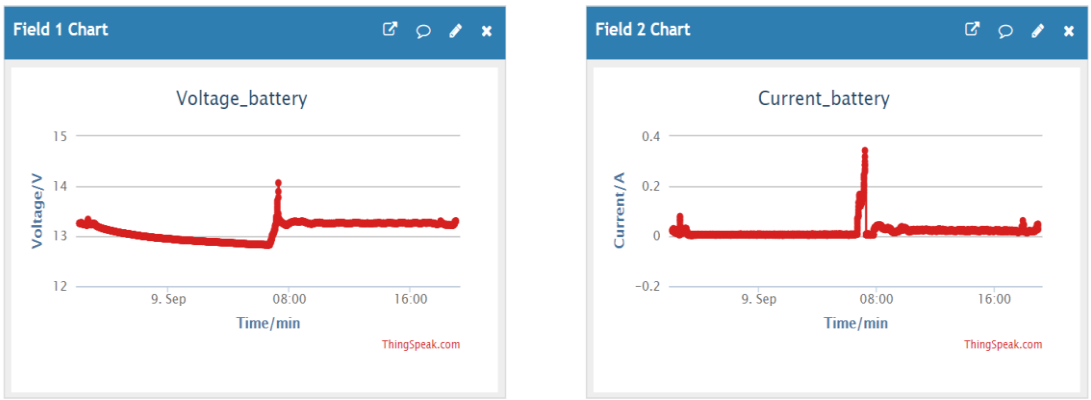


Figure 4.20 Voltage and Current of Battery in One Day

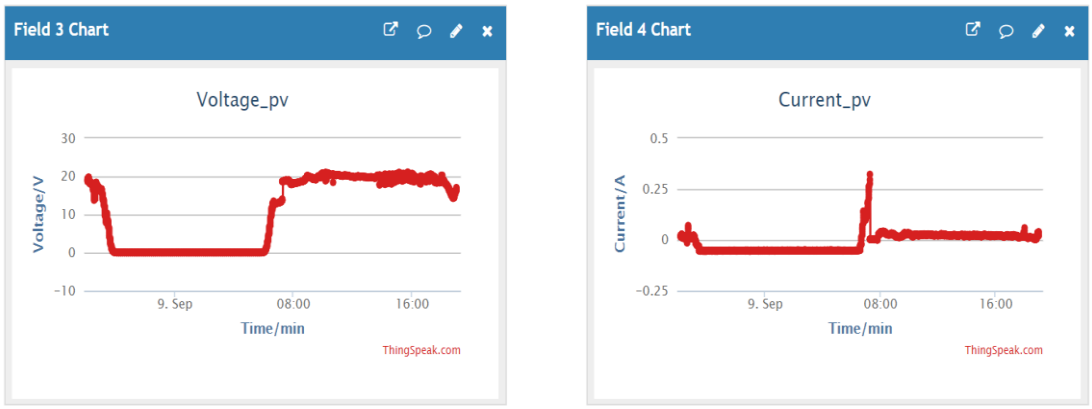


Figure 4.21 Voltage and Current of PV Array in One Day

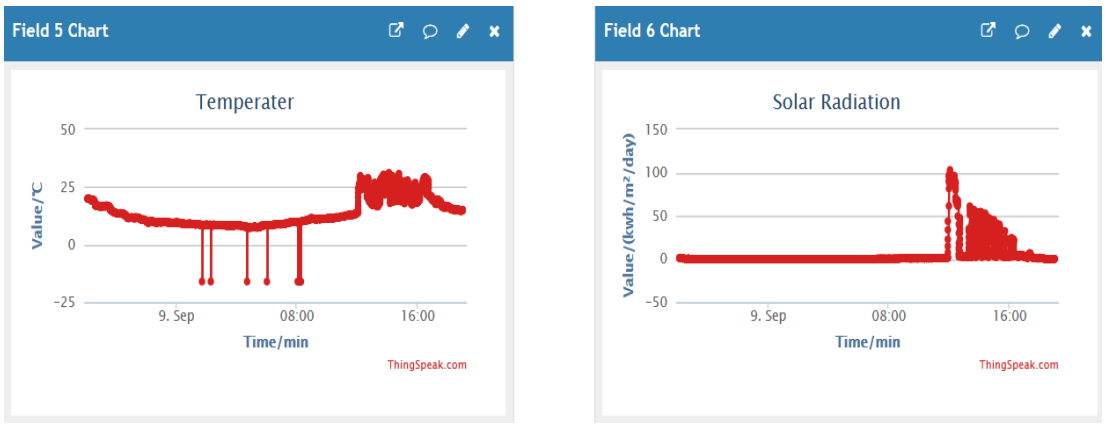


Figure 4.22 Temperature and Solar Radiation in One Day

From the comparison between the solar radiation and current-voltage data of the system, it can be seen that the value of solar radiation is proportional to the values of input-output voltage and current of MPPT. During the day time, the output voltage of MPPT (battery voltage) is lower than the input voltage of MPPT. There are two reasons for this phenomenon. The first is that the PV array's output voltage at the maximum power point is always smaller when the voltage of the battery is low. The second reason is that MPPT's DC/DC converter is open-circuit for the most time of each cycle due to the near fully charged battery. This results in the fact that MPPT's output voltage is closer to battery voltage.

From figure 4.22, it can be seen that the temperature is also proportional to solar radiation. Please notice that the solar radiation is not equal to the radiation received by

the PV array. That is caused by the shadow from the infrastructure near the light resistor (shown in figure 4.23).

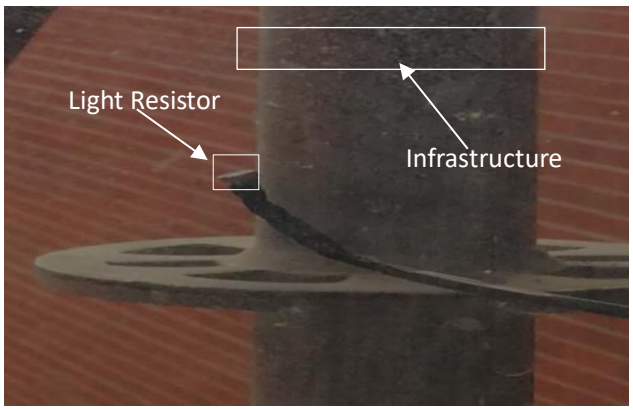


Figure 4.23 Project Obstruction

All collected sensor data is shown in figure 4.24 below.

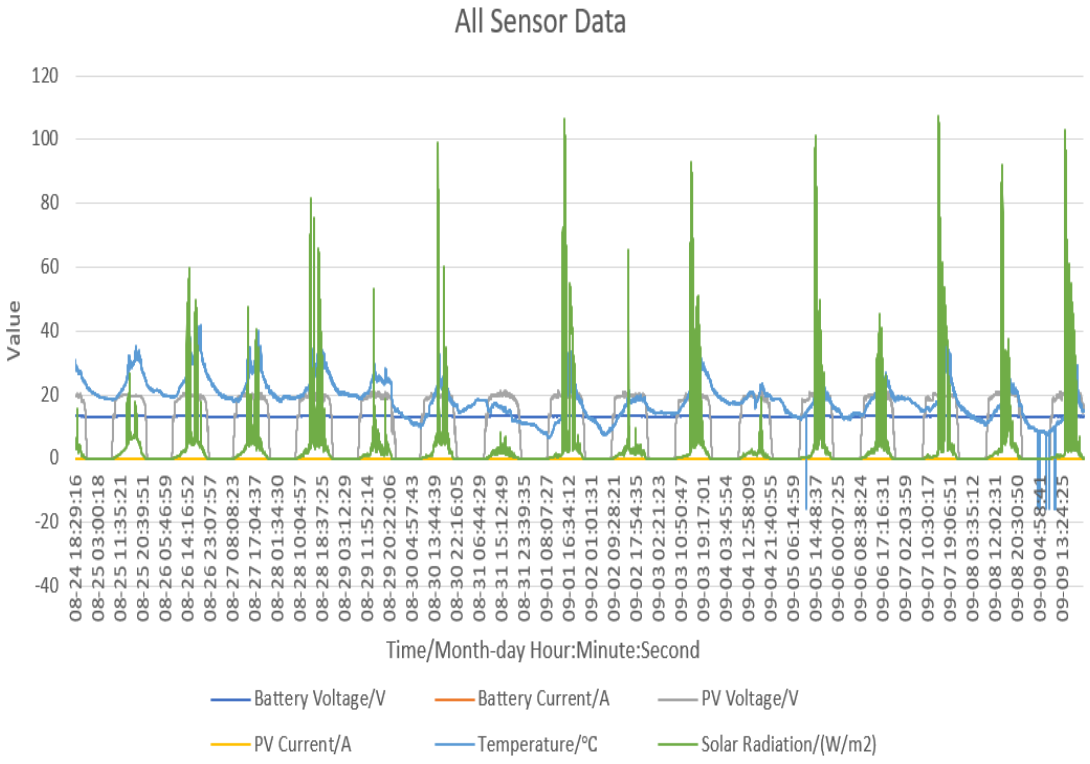


Figure 4.24 All Sensor Data

Figure 4.24 shows that the voltage and current of the battery and PV array and the temperature are proportional to solar radiation. The PV array begins to receive solar radiation and charge the battery around 6 am. every day. Simultaneously, the output

voltage of PV array resumes to 20V from 0V, and its output current begins to increase to a positive value. Due to one night's discharge, the capacity of the battery drops. Moreover, MPPT starts its functions. During 5 am. to 8 am., MPPT's output voltage (battery voltage) increases to track PV array's maximum output power, so do the battery current and PV current. After this period, the battery is fully charged. The current and voltage of the system keep constant for the rest of the daytime. Around 8 pm. solar radiation declines to a certain value when the output voltage and current of the PV array begin to decline. At the same time, the power from the PV array is not enough to compensate for the self-discharge energy of the battery, so the voltage and current of the battery also decrease. During the night without solar radiation, the output voltage of the PV array becomes zero, so do the output current of the PV array and MPPT. The output voltage of MPPT is equal to the battery voltage during the same period since the blocking diode of the PV array and the power electronic device of MPPT block the electrical connection between the PV array and battery.

Figure 4.24 and the temperature in figure 4.22 show that there are some interruptions in the temperature measurement of the last day. This is because the circuit to measure temperature does not have the function to eliminate these interruptions during measurement, which needs to be improved in future research.

### 4.7.3 Data Analysis

The battery is near fully charged all the time, and the measurement of solar radiation is frequently disturbed by the shadow of the infrastructure mentioned in section 4.6.2. Thus, it is not reliable to check the operation of the PV array based on the collected data. In this section, only the efficiency and daily energy supply of the MPPT are analyzed in MATLAB based on the collected data. The flow chart of data-analysis program in MATLAB is shown in figure 4.25 below.

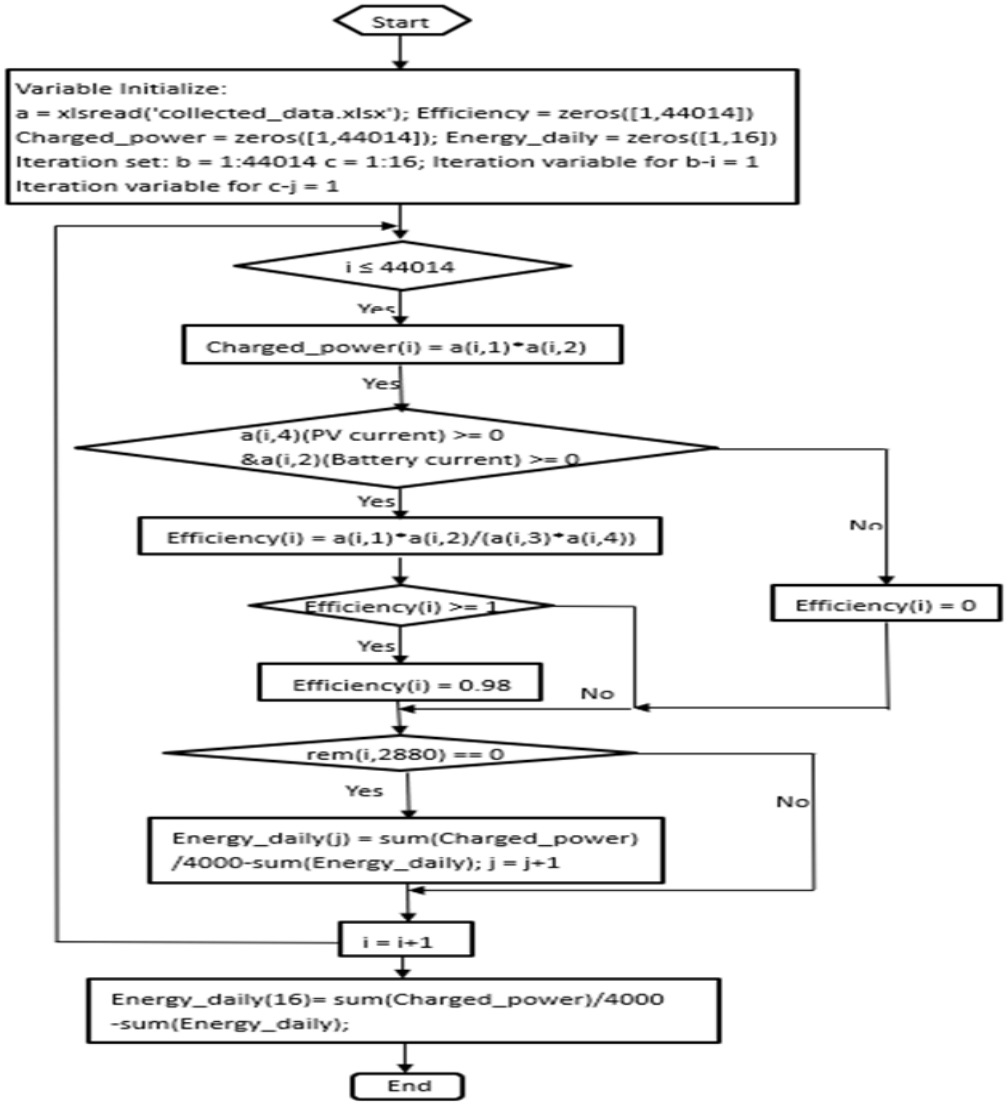


Figure 4.25 Flow Chart of Data Analysis in MATLAB

Figure 4.25 shows that the efficiency and output power of MPPT is initialized as 1×44014 arrays. Each element of arrays results from the process of each loop. When there is no solar radiation, the output current, and input current of MPPT sometimes are less than zero due to battery discharge, and the MPPT stops functioning during this time. Thus, in each loop, if any current is less than zero, the efficiency is set to zero. Because of the measurement error of current and voltage, the efficiency is sometimes equal to or larger than 1. The value is then set to 0.98 which is the maximum efficiency of the MPPT. After efficiency calculation, the daily energy supply from the 1$^{st}$ to 15$^{th}$ day is calculated every 2880 loops, and the daily energy of the 16$^{th}$ day is calculated by

subtracting the supplied energy in previous 15 days from the total supplied energy after the loop. The detailed MATLAB program is pasted in figure 4.26, and the resulted output power and efficiency of the MPPT are shown in figure 4.27.

```
x = 1:44014;
x1 = 1:16;
Efficiency = zeros([1 44014]);
Charged_power = zeros([1 44014]);
a = xlsread('collected_data.xlsx');
Energy_daily = zeros(1,16);
j = 1;

for i = 1:44014

   Charged_power(i) = a(i,1)*a(i,2);

   if(a(i,2) >= 00.001 && a(i,4) > 0)
      Efficiency(i) = a(i,1)*a(i,2)/(a(i,3)*a(i,4));
      if(Efficiency(i) >= 1)
         Efficiency(i) = 0.98;
      else
      end
   else
      Efficiency(i) = 0;
   end

   if(rem(i,2880) == 0)
      Energy_daily(j) = sum(Charged_power)/4000-sum(Energy_daily);
      j = j+1;
   else
   end
end

Energy_daily(16) = sum(Charged_power)/4000-sum(Energy_daily);

plot(x, Efficiency, x, Charged_power)
pause
plot(x, Energy_daily)
Charged_energy = sum(Charged_power)/4000;
```

Figure 4.26 MATLAB Program for Data Analysis

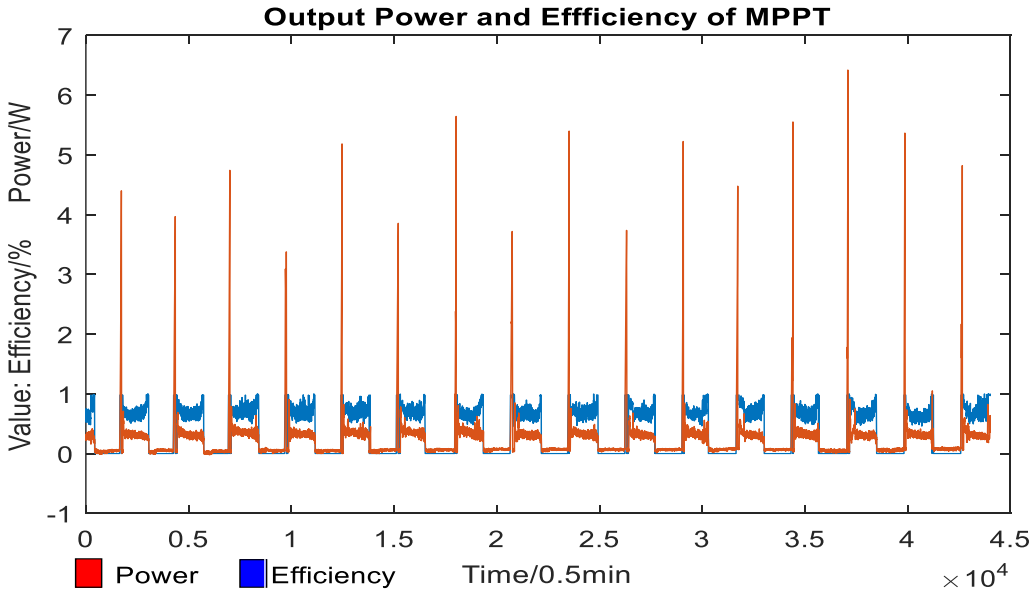


Figure 4.27 Output Power and Efficiency of MPPT

Figure 4.27 shows that MPPT's efficiency during the morning and evening is the largest during each day. After discharging for one night, the voltage and capacity of the battery are the lowest of the day. Because the solar radiation during this time is also low, to charge the battery quickly, MPPT operates in high efficiency to get maximum power from the PV array. Similarly, during the evening when solar radiation decreases to a very low level, MPPT operates in high efficiency to extract maximum power from the PV array to compensate for the self-discharge power of the battery. Since the solar radiation during the rest of daytime is higher, the MPPT operates in a relatively lower efficiency to limit the power output of the PV array preventing the battery from overcharging.

The energy supplied to the battery in each day is shown in figure 4.28 below.

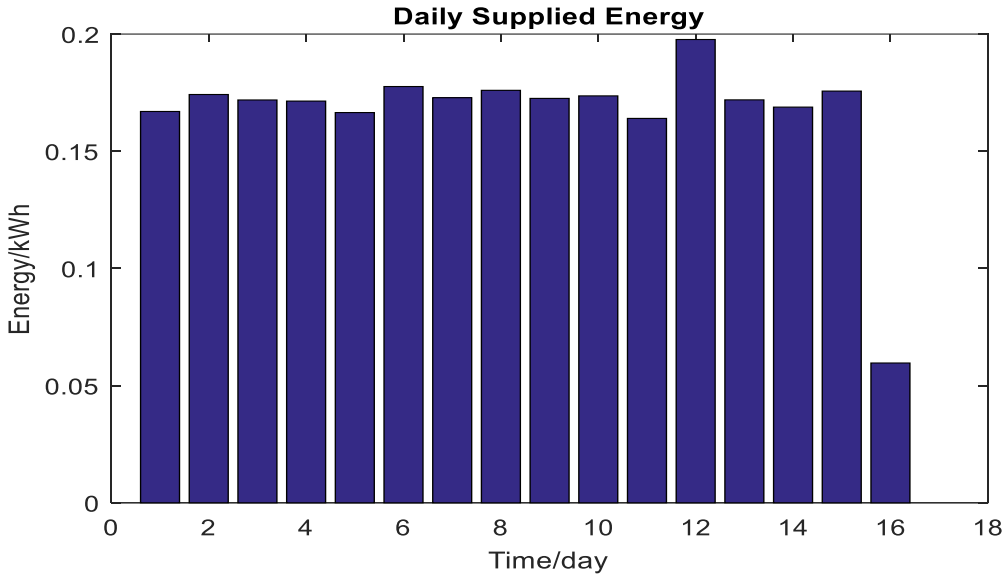


Figure 4.28 Daily Supplied Energy

Figure 4.28 shows that the energy supplied to the battery is very low on the 16$^{th}$ day. This is because the operation of the setup was stopped by the lab administrator in the middle of that day. Except for that, the supplied energy in rest days is very even due to the stable weather in these 16 days.

## 4.8 Conclusion

This chapter presented the design of data logger, data storage and data visualization system, all circuit details, all logged data and fundamental data analysis. The designed system performed well during the best period of 16 days. Issues faced during data logging and design are also described in this chapter, such as the solar radiation block from nearby infrastructure, uncalibrated solar and temperature sensor circuits, unexpected interruption and so on. More detailed data analysis of the PV array's operation will be presented after fixing these issues in future research.

# Chapter 5

# Conclusion and Future Work

## 5.1 Research Summary

This thesis presented the design of a hybrid power system for a remote house in China, including system modeling and simulation. The households abundant wind and solar energy resources due to high altitude and flat terrain. To compensate the intermittent solar and wind energy, a DC-coupled solar-diesel hybrid power system is designed in Homer, which achieves high renewable penetration and eliminates a large amount of diesel consumption. The system can also fulfill its economic requirements, of which the payback time is 20 years.

The dynamic model of the hybrid system is then built in Simulink to check the transient dynamics of the system. To increase the simulation speed, the simplified models [13] are adopted in the simulation model. The control system maintains the steady-state operation of the whole system under various disturbances. The simulation results show that the MPPT can achieve the maximum power of the PV array under various solar radiation, the diesel generator can be appropriately switched on and off according to the solar power, load and capacity of the battery storage, the soft starter of the diesel generator can prevent the fault of IGBT connection due to long-time operation, the charge controller and supervisory keep the battery storage from overcharging and overdischarging, the inverter can steadily converter DC to AC under system disturbance. All of these ensure a steady operation of the whole hybrid power system.

PID+R+CCF decreases the waveform deformation of the inverter output, and the DC voltage regulator stabilizes the DC input voltage of the inverter. The regulator is a boost converter, which both boosts up and stabilizes the input voltage of the inverter. Due to the switching operation of the inverter, the dynamics of the converter becomes nonlinear and undetectable. A time-delayed controller, which belongs to robust control

methods, is therefore designed for the DC voltage regulator. According to the simulation results, the DC voltage regulator can achieve good performance under input voltage variations and load transitions, and the waveform of the inverter is very close to a standard sinewave.

For system monitoring, a data logging system, which includes 2 data loggers and a web transfer on the PC, is built for an isolated PV system. The synchronized radio-frequency transmission between data loggers ensures the updated measurement for web transfer. The voltage levels between data loggers and radio frequency transmission are transferred by RS232-TTL interface circuits. By python program, the PC receives all sensor data and transfers them to thingspeak server. This enables system monitoring from anywhere connected to the Internet. An alarm message is set to be tweeted from the web server to the user for system maintenance when the data transfer is interrupted. This data logging system is robust and tested for 16 days without interruption, which can be prolonged if the lab manager did not shut it down. The data analysis on MATLAB also shows that the system kept steady operation during the test.

## 5.2 Research Contribution

- Designed a solar-diesel hybrid power system for a rural area in Qinghai Province of China. The designed system achieves reliability, high renewable penetration (> 60%) and suitable payback time (20 years).
- Designed an MPPT with simplified incremental inductance control method, of which the program is more straightforward than the original method.
- Designed a soft starter that can bypass the IGBT connection of the diesel generator between startups and shutdowns, which decreases the probability of the disconnection with the whole system.
- Designed a DC input voltage regulator controlled by TDC for a single-phase inverter controlled by PID+R+CCF controller, which achieves stable DC input voltage and little output voltage distortion of the inverter.

- Designed a data logging system with synchronized radio communication which ensures most updated measurements sent to the PC.
- Designed a robust data transfer from the data logging system to the web server. The uploaded data are downloaded and further analyzed on MATLAB.

## 5.3 Future Work

- Design a solar-wind-diesel hybrid power system for the selected location for higher renewable penetration.
- Develop a time-delayed controller with its parameters adjusted by fuzzy logic control to achieve a broader load range of the DC voltage regulator.
- Develop hardware for the regulator-inverter system to validate the performance of the designed control system (time-delayed controller for the regulator, PID+R+CCF for the inverter).
- Include the function of data analysis in the python program and transfer the results to the web server for visualization.
- Enable the load control of the isolated PV system from the Internet.

## 5.4 List of Publications

[1] Bojian Jiang, M. Tariq Iqbal, "Dynamic Modeling and Simulation of an Isolated Hybrid Power System in a Rural Area of China," Journal of Solar Energy Volume 2018, doi: https://doi.org/10.1155/2018/5409069.

[2] Bojian Jiang, M. Tariq Iqbal, "The Dynamic Modeling and Simulation of Hybrid Power System for a Remote Location in China," The 26th Annual Newfoundland Electrical and Computer Engineering Conference, 2017.

[3] Bojian Jiang, M. Tariq Iqbal, "Data Logging and Visualization System for an Isolated PV System," to be submitted.

# References

[1] J. F. Manwell, J. G. McGowan and A. L. Rogers, “Wind Energy Explaned Theory, Design and Application Second Edition”, pp447-501, 2009.

[2] Chong Li, Xinfeng Ge, Yuan Zheng, Chang Xu, Yan Ren, Chenguang Song and Chunxia Yang, “Techno-economic feasibility study of autonomous hybrid wind-PV-battery power system for a household in Urumqi, China”, Energy 55 (2013) 263-272.

[3] Godfrey Boyle, Bob Everett, et al., “Renewable Energy: Power for a Sustainable Future”, 3rd edition, pp75-91, 2012.

[4] Arthouros Zervos, Christine Lins, et al., “Renewable 2017 Global Status Report”, REN21, 2017, Retrieved from REN21 website: http://www.ren21.net/ gsr-2017.

[5] Fangqiu Xu, Jicheng Liu, Shuaishuai Lin, Qiongjie Dai and Cunbin Li, “A Multi-Objective Optimization Model of Hybrid Energy Storage System for Non-Grid-Conn ected Wind Power: A Case Study in China”, Elsevier, Energy 163 (2018) 585-603.

[6] https://www.alibaba.com/product-detail/solar-energy-system-off-grid-5KW_6047 5172138.html?spm=a2700.7724838.2017115.92.348e7eabhQsjjt.

[7] Lina Yan et al., “China Energy Efficiency Report”, International Energy Charter.

[8] Jie Chen, Wei Liu, Deyi Jiang, Junwei Zhang, Song Ren, Lin Li, Xiaokang Li and Xilin Shi, “Preliminary investigation on the feasibility of a clean CAES system coupled with wind and solar energy in China”, Energy 127 (2017) 462-478.

[9] Lose´ L. Bernal-Agustı´n and Rodolfo Dufo-Lo´pez, “Simulation and optimization of stand-alone hybrid renewable energy systems”, Electrical Engineering Department, University of Zaragoza, Calle Marı´a de Luna 3, 50018 Zaragoza, Spain, 2009.

[10] Mohammad El Badawe, Tariq Iqbal and Geroge K.I. Mann,” Optimization and Modeling of a Stand-Alone Wind/PV Hybrid Energy System”, 2012 25th IEEE Canadian Conference on Electrical and Computer Engineering.

[11] Milana Trifkovic, Mehdi Sheikhzadeh, Khaled Nigim and Prodromos Daoutidis, “Modeling and Control of a Renewable Hybrid Energy System with Hydrogen Storage”, IEEE Transaction on Control Systems Technology, Vol. 22, No. 1, January 2014, 1063-

6536.

[12] M. J. Khan and M. T. Iqbal, “Dynamic modeling and simulation of a small wind–fuel cell hybrid energy system”, Renewable Energy Volume 30, Issue 3, March 2005, pp421–439.

[13] MATLAB 2016

[14] Abdulhamed Hwas, Reza Katebi, “Wind Turbine Control Using PI Pitch Angle Controller”, IFAC Conference on Advances in PID Control PID'12 Brescia (Italy), March 28-30, 2012.

[15] Huan-Liang Tsai, Ci-Siang Tu, and Yi-Jie Su, “Development of Generalized Photovoltaic Model Using MATLAB/Simulink”, Proceedings of the World Congress on Engineering and Computer Science 2008 WCECS 2008, October 22 - 24, 2008, San Francisco, USA.

[16] Ling Qin, Shaojun Xie, Chen Yang, Jiankun Cao, “Dynamic Model and Dynamic Characteristics of Solar Cell”, 2013 IEEE ECCE Asia Downunder, June 2013, pp.659-663.

[17] Shah Arifur Rahman, Rajiv K. Varma, Tim Vanderheide, “Generalized Model of a Photovoltaic Panel”, IET Renewable Power Generation, 2014, Vol. 8, Issue 3, pp. 217-229.

[18] E. Hyman, W. C. Spindler, and J. F. Fatula, “Phenomenological discharge voltage model for lead acid batteries”, Proceedings of AIChEL Meeting, November,1986.

[19] I. Kamwa, “Dynamic modelling and robust regulation of a no-storage wind-diesel hybrid power system,” Electrical Power Systems Research, vol.18, pp.219–233, 1990.

[20] T. Theubou, R. Wamkeue and Kamwa, “Dynamic Model of Diesel Generator Set for Hybrid Wind-Diesel Small Grids Application”, 2012 25th IEEE Canadian Conference on Electrical and Computer Engineering (CCECE) 978-1-4673-1433-6/12/$31.00 ©2012 IEEE.

[21] George C. Konstantopoulos, Antonio T. Alexandridis, “Non-linear voltage regula -tor design for DC/DC boost converters used in photovoltaic applications: analysis

and experimental results", IET Renewable Power Generation, 2013, Vol. 7, Issue 3, pp. 296–308.

[22] Rick Zaitsu, "Voltage Mode Boost Converter Small Signal Control Loop Analysis Using the TPS61030", Texas Instrument Application Report SLVA274A–May 2007.

[23] Ya-Xiong Wang, Duck-Hyun Yu, and Young-Bae Kim, "Robust Time-Delay Control for the DC-DC Boost Converter", IEEE Transactions on Industrial Electronics, Vol. 61, NO. 9, September 2014.

[24] Jinjun Liu, Peiyun Qing, Xu Yang, Yue Wang, Zhaoan Wang and Zhuo Fang, "Power Electronics", 5th edition, pp.97-138, 2009 ISBN 978-7-111-26806-2.

[25] Xiao Liu, Aaron M. Cramer, Fei Pan, "Generalized Average Method for Time-Invariant Modeling of Inverters", IEEE Transaction on Circuits and Systems–I: regular papers, Vol. 64, No. 3, March 2017.

[26] Yanbo Che, Guojian Liu, Zhangang Yang, Xiaokun Liu, "Model of Inverter in More Electric Aircraft Based on Generalized State Space Averaging Approach", 2015 6th International Conference on Power Electronics, IEEE, Doi: 10.1109/PESA.2015. 7398935.

[27] M. Kalantar, S.M. Mousavi G, "Dynamic behavior of a stand-alone hybrid power generation system of wind turbine, microturbine, solar array and battery storage", Applied Energy Volume 87, Issue 10, October 2010, Pages 3051–3064.

[28] D. K. Sharma and G. Purohit, "Advanced Perturbation and Observation (P&O) based Maximum Power Point Tracking (MPPT) of a Solar Photo-Voltaic System", 2012 IEEE 5th India International Conference on Power Electronics, Dec. 2012, pp. 1-5, ISBN 976-1-4673-0931-8.

[29] B. Amrouche, M. Belhamel and A. Guessoum, "Artificial Intelligence Based P&O MPPT Method for Photovoltaic Systems", Revue des Energies Renewables ICRESD-07 Tlemcen (2007) II - 16.

[30] Dong Dong, Timothy Thacker, Rolando Burgos, Fei Wang, Dushan Boroyevich, "On Zero Steady-State Error Voltage Control of Single-Phase PWM Inverters with Different Load Types", IEEE Transactions on Power Electronics, VOL. 26, NO. 11,

November 2011.

[31] Muhammad. Tila, Khan. Adnan Umar, Jamil. Nouman, Zameer. Junaid and Khawar. Muhammad, “DC Voltage Regulator for Battery Less PV System Using MPPT”, 2015 Power Generation System and Renewable Energy Technologies, June 2015, pp.1-6.

[32] N. F Nik Ismail, I. Musirin, R. Baharom, D. Johari, “Fuzzy Logic Controller on DC/DC Boost Converter”, 2010 IEEE International Conference on Power and Energy (PECon2010), Nov 29 - Dec 1, 2010, Kuala Lumpur, Malaysia.

[33] Hegazy Rezk, Igor Tyukhov, Mujahed Al-Dhaifallah and Anton Tikhonov, “Performance of Data Acquisition System for Monitoring PV System Parameters”, Measurement 104 (2017) 204–211.

[34] Francisco J. Sánchez-Pacheco, Pedro Juan Sotorrío-Ruiz, Juan R. Heredia-Larrubia, Francisco Pérez-Hidalgo and Mariano Sidrach de Cardona, “PLC-Based PV Plants Smart Monitoring System: Field Measurements and Uncertainty Estimation”, IEEE Transactions on Instrumentation and Measurement, Vol. 63, No. 9, September 2014.

[35] Farid Touati, M.A. Al-Hitmi, Noor Alam Chowdhury, Jehan Abu Hamad and Antonio J.R. San Pedro Gonzales, “Investigation of solar PV performance under Doha weather using a customized measurement and monitoring system”, Renewable Energy 89 (2016) 564-577.

[36] https://en.m.wikipedia.org/wiki/Xbee

[37] Terashmila Lasagani K. A., Tariq Iqbal, George Mann, “Data Logging and Control of a Remote Inverter Using Lora and Power Line Communication”, Energy and Power Engineering (EPE) Journal, Vol. 10, No. 8, August 2018.

[38] http://www.88cc88.com

[39] http://www.bipvcn.org/popsci/6799.html/attachment/9

[40] https://search.earthdata.nasa.gov/search/granules?p=C1276812695-GES_DISC&m=37.2568359375!101.232421875!6!1!0!0%2C2&tl=1531779965!4!!&q=temperature&ok=temperature&sp=101.583984375%2C37.5029296875

[41] Jie Chen, Wei Liu, Deyi Jiang, Junwei Zhang, Song Ren, Lin Li, Xiaokang Li and Xilin Shi, “Preliminary Investigation on the Feasibility of a Clean CAES System Coupled with Wind and Solar Energy in China”, Energy 127 (2017) 462-478, doi: http: //dx.doi.org/10.1016/j.energy.2017.03.088.

[42] B. Reshef, H. Suehrcke and J. Appelbaum, “Analysis of a Photovoltaic Water Pumping System”, Eighteenth Convention of Electrical and Electronics Engineers in Israel (1995), IEEE, doi: 10.1109/EEIS.1995.513787.

[43] Brigitte Hauke, “Basic Calculation of a Boost Converter's Power Stage”, Texas Instrument Application Report, SLVA372C, November 2009.

[44] Maaspaliza Azzi, Nasrudin Abd. Rahim, “Design Analysis of Low-pass Passive Filter in Single-phase Grid-connected Transformerless Inverter”, International Journal of Renewable Energy Research 1 (2011) 25-31, 2011.

[45] Dong Dong, et al., “Control Design and Experimental Verification of a Multi-Function Single-Phase Bidirectional PWM Converter for Renewable Energy Systems”, IEEE, 2009 13th European Conference on Power Electronics and Applications.

[46] Dong Dong, Timothy Thacker, Rolando Burgos, Fei Wang, Dushan Boroyevich, “On Zero Steady-State Error Voltage Control of Single-Phase PWM Inverters with Different Load Types”, IEEE Transactions on Power Electronics, VOL. 26, NO. 11, November 2011.

[47] Rick Zaitsu, “Voltage Mode Boost Converter Small Signal Control Loop Analysis Using the TPS61030”, Texas Instrument Application Report SLVA274A–May 2007.

[48] Katsuhiko Ogata, “Modern Control Engineering”, 3rd edition, Prentice Hall, ISBN: 0-13-227307-1997, 1997.

[49] PyungH. Chang, Jeong W. Lee, “A Model Reference Observer for Time-Delay Control and Its Application to Robot Trajectory Control”, IEEE Transactions on Control Systems Technology, Vol. 4, No. 1, January 1996.

[50] K. Youcef-Tomi and S. Reddy, “Analysis of Linear Time Invariant Systems with Time Delay”, Proc. of American Control Conference, pp. 1940-1944, 1992.

[51] https://www.topsolarpanel.com/product/sunforce-37130-130w-crystalline-solar-panel

[52] Coleman 12V 30Amp Digital Charge Controller User's Manual

[53] https://www.interstatebatteries.com/products/srm24?productLine=marine&subcategoryKey=&ignorecategoryid=true

[54] "Fully Integrated, Hall Effect-Based Linear Current Sensor IC with 2.1kVRMS Isolation and a Low-Resistance Current Conductor", ACS712-DS, Rev. 16, Allegro MicroSystems, LLC, June 5, 2017.

[55] "MAX232x Dual EIA-262 Drivers/Receivers", SLLS047M-February 1989-Revised November 2014.

[56] "CDS Photoconductive Photocells PDV-P8103", Luna Optoelectronics, Rev 01-04-16.

[57] https://www.mathworks.com/help/thingspeak/

[58] Low Voltage Temperature Sensors: TMP35/TMP36/TMP37 Data Sheet